Contributions to ionospheric modeling with GNSS in mapping function, tomography and polar electron content features

Haixia Lyu

Supervisor: Prof. Dr. M. Hernández-Pajares

Aerospace Science and Technology Doctoral Program
Universitat Politècnica de Catalunya

Thesis submitted as a collection of published articles

July, 2020

Acknowledgements

2020, the minimum of Solar Cycle 25, is a special year for the whole world, due to the far and wide impact of Covid-19. This Pandemic crisis brings our hearts closer, in spite of the containment measures and social distancing reducing physical contact. There is a Chinese poem saying "Hai nei cun zhi ji, tian ya ruo bi lin", meaning "Great friendship can overcome long distance". One day this crisis would be over, or we learn how to coexist with the virus, and we could hug each other again in the sunshine. It might sound clichéd, but it is true: We need to take love, courage and incredible patience to make a difference in our life. In this context, I decide to write the Acknowledgements section in a semi-formal way.

Despite that I grew up underprivileged, I am very lucky and well protected by my parents, teachers and bosses in my life, making me be able to concentrate on learning, studying and working without interruption. I would love to thank Chinese Coucil Scholarship (CSC), Prof. Hongping Zhang and Prof. Min Li at GNSS Research Center of Wuhan University, Institut d'Estudis Espacials de Catalunya (IEEC), Prof. Manuel Hernández-Pajares at UPC-IonSAT research group, Dr. Estel Cardellach at IEEC-ICE-CSIC for the financial support during my academic years for studying in Barcelona and participating in international conferences. Without them, this dissertation would not have been possible.

I forego the pleasure it would be to thank my supervisor, Prof. Manuel Hernández-Pajares, to whom I am indebted for his invaluable guidance, support, advice and encouragement. I look upon him as pre-eminent researcher, whose passion and philosophical attitude have deeply influenced me. I admire him because he is such a rich person. By rich I do not mean anything related to money or wealth. I mean the confidence when facing what life presents him, the ability to bounce back and solve problems, the internal richness that nobody can take away from him. During the preparation of this thesis, I read with care and profound interest Manuel's papers, which stirred up in me a burning zeal to add the most humble contribution. Working with him is such a pleasant experience, making me have an irresistible urge to follow in his footsteps.

I would love to thank Prof. Enric Monte Moreno for his suggestions, wisdom, guidance, encouragement and all the things he has taught me during these years. He is a polymath, as gifted as he is versatile. His elegantly lucid lectures impressed and inspired me a lot.

Manuel and Enric are such charismatic teachers that, I believe, their lectures would be overflowed with students standing on ladders at the windows in China if they could teach in Chinese.

I wish to thank all my colleagues and visitors at UPC-IonSAT group, particularly Victoria Graffigna, Alberto García-Rigo, David Roma-Dollase, Fabricio dos Santos Prol, Jiachun An. Cooperation with them has been particularly inspiring and congenial. I would also like to acknowledge specifically my gratitude to Prof. Jingnan Liu, Prof. Hongping Zhang, Prof. Zhenghang Li, Prof. Min Li and Prof. Jingbin Liu in Wuhan University, who have generously supported me by word and deed. Furthermore, I am particularly grateful, too, to reviewers and researchers for immensely insightful comments on related papers, presentations and posters.

My thanks are due to my landlady Maribel, landlord Miguel and their family for offering me such a warm home environment in Barcelona and great help in local integration. Also my warm thanks to all friends who I knew in China and Barcelona. I have greatly enjoyed the help and encouragement given by them - no one named, no one forgotten.

My gratitude extends, naturally, to my family, who have never ceased to encourage me.

During these years, I learn that the purpose of the academic journey is the journey itself. Going is important, not arriving. Looking back this journey, I would love to thank all the people who gave me their time, their wisdom, concrete help along the path, and would like to say to myself "no hay camino sino estelas en la mar". I will continue walking, making my own road.

In the end, I would share with friends and particularly the professors who have taught me a few sentences in the poem "Youth" by Samuel Ullman: " Youth is not a time of life; it is a state of mind; it is not a matter of rosy cheeks, red lips and supple knees; it is a matter of the will, a quality of the imagination, a vigor of the emotions; it is the freshness of the deep springs of life. ... Whether sixty or sixteen, there is in every human being's heart the lure of wonder, the unfailing child-like appetite of what's next, and the joy of the game of living. In the center of your heart and my heart there is a wireless station; so long as it receives messages of beauty, hope, cheer, courage and power from men and from the Infinite, so long are you young."

Abstract

UNESCO codes: 120321, 220209, 250118

This dissertation focuses on determining the vertical electron content distribution in low and high vertical resolution from ground-based and LEO on board GNSS data and improving the knowledge of ionosphere climatology in northern mid-latitude and polar regions. The novelty is summarized in the following four aspects:

The first contribution is to propose a new ionospheric mapping function concept - Barcelona Ionospheric Mapping Function (BIMF), in order to improve STEC (Slant Total Electron Content) conversion accuracy from any given VTEC (Vertical Total Electron Content) model. BIMF is based on the climatic modeling of the VTEC fraction in the second layer - μ_2, which is the byproduct of UQRG generated by UPC. The first implementation of BIMF is BIMF-nml for the northern mid-latitudes, where the latitudinal variation of μ_2 is neglected. μ_2 is modeled as function of date and local time. From the user's perspective, BIMF is the linear combination of μ_2 and the standard ionospheric mapping function, and only needs 41 constant coefficients, making BIMF achieve the simplicity for application. The good performance has been demonstrated in the dSTEC assessment for different IGS GIMs: UQRG, CODG and JPLG.

The second contribution is to confirm the capability of UQRG GIMs to detect representative ionospheric features in polar regions through six case studies, including TOI (Tongue of Ionization), trough, flux transfer event, theta-aurora, ionospheric convection patterns and storm enhanced density. The long-term VTEC and μ_2 data provide valuable databases for studying the morphology and climatology of polar ionospheric phenomena. The unsupervised clustering results of normalized VTEC distribution show that TOI and polar cap patches exhibit an annual dependence, i.e. most TOI and patches occurring in the North Hemisphere winter and the South Hemisphere summer.

The third contribution is to propose a hybrid method - AVHIRO (the Abel-VaryChap Hybrid modeling from topside Incomplete RO data), to solve an ill-posed rank-deficient problem in the Abel electron density retrieval. This work is driven by the future EUMETSAT Polar System 2nd Generation, which provides truncated ionospheric RO data, only below impact heights of 500 km, in order to guarantee a full data gathering of the neutral part.

AVHIRO takes advantage of one Linear Vary-Chap model, where the scale height increases linearly with altitude above the F_2 layer peak, and uses Powell search to solve the full electron densities, ambiguity term, and four parameters of the Vary-Chap model simultaneously, taking into account the nonlinear interactions between the unknown parameters.

The fourth contribution is to take advantage of the geometry brought by combining DORIS, ground-based Galileo, ground-based, LEO-POD and vessel-based GPS data and ingest the multi-source dual-frequency carrier phase measurements into the tomographic model to improve the GIM VTEC estimation precision. The impact of adding each type of measurements, which are Galileo data, vessel-based GPS data, DORIS and LEO-POD GPS data, to ground-based GPS data on GIM product is examined according to two complementing evaluation criteria, JASON-3 VTEC comparison and GPS dSTEC test. This study proves the expected better GIM performance by new data ingestion into tomographic model, which is a successful step forward from conception to initial experimental validation.

Resumen

UNESCO códigos: 120321, 220209, 250118

Esta disertación está centrada en determinar la distribución vertical del contenido de electrones en resolución vertical baja y alta a partir de medidas GNSS terrestres y a bordo de satélites de órbita baja (LEO), además de utilizar medidas GNSS desde buques y medidas DORIS, además de mejorar el conocimiento de la climatología de la ionosfera en las regiones polares y en latitudes medias del hemisferio norte. Las contribuciones se pueden resumir en los siguientes cuatro aspectos:

La primera contribución consiste en proponer un nuevo concepto de función de mapeo ionosférico: la función de mapeo ionosférico de Barcelona (BIMF), con el fin de mejorar la precisión de conversión de STEC (contenido total de electrones inclinado) a partir de cualquier modelo de VTEC (contenido total de electrones vertical). BIMF se basa en el modelado climático de la fracción VTEC en la segunda capa - μ_2, que es el subproducto de UQRG generado por UPC. La primera implementación de BIMF es BIMF-nml para las latitudes medias del hemisferio norte. μ_2 se modela en función del dia y la hora local. Desde la perspectiva del usuario, BIMF es la combinación lineal de μ_2 y la función de mapeo ionosférico estándar, y solo necesita 41 coeficientes constantes, lo que hace que BIMF sea facilmente aplicable. Su buen comportamiento se demostró en la evaluación dSTEC para diferentes IGS GIM: UQRG, CODG y JPLG.

La segunda contribución se centró en confirmar la capacidad de los GIM UQRG para detectar características ionosféricas representativas en regiones polares a través de seis estudios de casos, que incluyen lenguas de ionización (TOI), depresión de ionización en forma de canal, sucesos de transferencia de flujo, theta-aurora, patrones de convección ionosférica y densidad aumentada durante tormentas geomagnéticas. Los datos a largo plazo de VTEC y μ_2 proporcionan valiosas bases de datos para estudiar la morfología y climatología de los fenómenos ionosféricos polares. Los resultados de agrupamiento no supervisados de la distribución normalizada de VTEC muestran que los TOI y los parches en los casquetes polares exhiben una dependencia anual, es decir, la mayoría de los TOI y parches ocurren en el invierno del Hemisferio Norte y el verano del Hemisferio Sur.

La tercera contribución ha consistido en proponer un método híbrido: AVHIRO (el modelo híbrido Abel-VaryChap a partir de datos de RO incompletos en la parte superior), para resolver un problema de rango deficiente en la recuperación de la densidad electrónica con el modelo de Abel. Este trabajo está motivado por el futuro sistema polar EUMETSAT de segunda generación, que proporciona datos truncados de RO ionosférica, sólo por debajo de las alturas de impacto de 500 km, con el fin de garantizar una recopilación completa de medidas de la parte neutra. AVHIRO aprovecha un modelo Linear Vary-Chap, donde la altura de la escala aumenta linealmente con la altitud por encima del pico de la capa F_2, y utiliza la búsqueda Powell para resolver las densidades completas de electrones, el término de ambig*üe*dad y cuatro parámetros del modelo Vary-Chap simultáneamente, teniendo en cuenta las interacciones no lineales entre los parámetros desconocidos.

La cuarta contribución es aprovechar la geometría aportada por la combinación de datos GPS DORIS, Galileo en tierra, LEO-POD y en barco, e incorporar las mediciones de la fase de la portadora de doble frecuencia de múltiples fuentes en el modelo tomográfico para mejorar la precisión de estimación de GIM VTEC. El impacto de agregar cada tipo de mediciones, que son datos de Galileo, datos de GPS basados en embarcaciones, datos de GPS DORIS y LEO-POD, a datos de GPS terrestres en productos GIM se examina de acuerdo con dos criterios de evaluación complementarios, comparación con VTEC[JASON-3] y con dSTEC[GPS]. Este estudio demuestra el mejor rendimiento esperado de GIM por la nueva ingesta de datos en el modelo tomográfico, que es un exitoso paso adelante desde la concepción hasta la validación experimental inicial.

Contents

List of Figures

List of Tables

Nomenclature

Acronyms / Abbreviations

AVHIRO the Abel-VaryChap Hybrid modeling from topside Incomplete RO data

BDS Beidou Navigation Satellite System

BIMF Barcelona Ionospheric Mapping Function

BIMF-nml Barcelona Ionospheric Mapping Function at northern mid-latitudes

CODE Center for Orbit Determination in Europe

DCB Differential Code Bias

DORIS Doppler Orbitography and Radio-positioning Integrated by Satellite

DOY Day Of Year

dRMSe daily RMS error

EPS-SG EUMETSAT Polar System - Second Generation

EUMETSAT European Organization for the Exploitation of Meteorological Satellites

FFT Fast Fourier Transform

FTE Flux Transfer Event

GEC Global Electron Content

GIM Global Ionospheric Map

GLONASS Globalnaja Nawigazionnaja Sputnikowaja Sistema

GNSS Global Navigation Satellite System

GPS Global Positioning System

HF High Frequency

IAAC Ionosphere Associate Analysis Centers

IDM the ion drift meter

IGS International GNSS Service

IMF Interplanetary Magnetic Field

IONEX IONosphere map EXchange format

IRI International Reference Ionosphere

IRO Ionospheric Radio Occultation

IROWG International Radio Occultation Working Group

JPL Jet Propulsion Laboratory

LBG Linde–Buzo–Gray

LEO Low Earth Orbit

LOS Line Of Sight

LT Local Time

LVQ the Learning Vector Quantization

MEO Medium Earth Orbit

MLT Magnetic Local Time

NTCM the Neustrelitz TEC Model

POD Precise Orbit Determination

PPP Precise Point Positioning

RMS Root Mean Square

RO Radio Occultation

RPA The retarding potential analyzer

RTK Real-Time Kinematic

SBAS Satellite-Based Augmentation System

SED Storm Enhanced Density

SEEIRO the Simple Estimation of Electron density profiles modeling from topside Incomplete RO data

SPP Standard Point Positioning

STD Standard Deviation

STEC Slant Total Electron Content

SuperDARN the Super Dual Auroral Radar Network

TDIM The Utah State University time dependent ionospheric model

TEC Total Electron Content

TID Travelling Ionospheric disturbance

TIEGCM The National Center for Atmospheric Research Thermosphere-Ionosphere Electrodynamics General Circulation Model

TOI Tongue of Ionization

TOMION the TOmographic Model of the IONosphere

UPC Universitat Politècnica de Catalunya

UT Universal Time

VCET Vary-Chap-based Extrapolation Technique of electron density

VTEC Vertical Total Electron Content

WARTK Wide-Area RTK

Chapter 1

Introduction

1.1 Ionosphere and GNSS

To date, Global Navigation Satellite Systems (GNSSs) include Global Positioning System (GPS), Globalnaja Nawigazionnaja Sputnikowaja Sistema (GLONASS), Galileo and BeiDou Navigation Satellite System (BDS). GNSSs were originally designed for positioning, navigation and timing, but surprisingly promote a wide range of scientific studies and industrial applications. Currently, GNSS service has become an indispensable infrastruture of Smart City at the societal level.

The ionospheric delay is one significant error source for GNSS signal. Because of the fact that the ionosphere is a dispersive medium, the dual-frequency measurements allow to cancel out or isolate the first-order ionospheric term, 99.9% of ionospheric delay, by linear combination. In turn, GNSS measurements have been used as important technical means to monitor the ionosphere with a unique temporal and spatial resolution. Different aspects of research and studies in GNSS ionosphere field have been explored, such as regional and global Vertical Total Electron Content (VTEC) modeling (Hernández-Pajares et al., 2009; Liu et al., 2011), ionosphere irregularities (Raghunath and Ratnam, 2015), Travelling Ionospheric disturbances (TIDs) (Afraimovich et al., 1998), ionospheric seismology (Jin et al., 2015), space weather (Jakowski et al., 2002), solar flares (Hernández-Pajares et al., 2012), and stellar flares (Hernández-Pajares and Moreno-Borràs, 2020).

This section introduces the basic GNSS observables and the ionospheric combination, which serve as the basic measurements in the studies presented in the dissertation.

1.1.1 GNSS observables

Two of the basic types of GNSS measurements are pseudorange and carrier phase.

The pseudorange P1 and P2 observation equations on two frequencies between the satellite j antenna and the receiver i antenna are:

$$P1_i^j = \rho_i^j + c(dt_i - dt^j) + rel_i^j + T_i^j + \alpha_1 STEC_i^j + K1_i^j + M_{P1,i}^j + \varepsilon_{P1,i}^j \tag{1.1}$$

$$P2_i^j = \rho_i^j + c(dt_i - dt^j) + rel_i^j + T_i^j + \alpha_2 STEC_i^j + K2_i^j + M_{P2,i}^j + \varepsilon_{P2,i}^j \tag{1.2}$$

The carrier phase L1 and L2 observation equations on two frequencies between the satellite j antenna and the receiver i antenna are:

$$L1_i^j = \rho_i^j + c(dt_i - dt^j) + rel_i^j + T_i^j - \alpha_1 STEC_i^j + B1_i^j + \omega_{L1} + m_{L1,i}^j + \varepsilon_{L1,i}^j \tag{1.3}$$

$$L2_i^j = \rho_i^j + c(dt_i - dt^j) + rel_i^j + T_i^j - \alpha_2 STEC_i^j + B2_i^j + \omega_{L2} + m_{L2,i}^j + \varepsilon_{L2,i}^j \tag{1.4}$$

where:

- ρ_i^j is the geometric distance between the satellite j antenna and receiver i antenna phase centers at emission and reception time, respectively: $\rho_i^j = \sqrt{(x^j - x_i)^2 + (y^j - y_i)^2 + (z^j - z_i)^2}$
- dt_i is the offset of the receiver i clock from GPS time.
- dt^j is the offset of the satellite j clock from the GPS time.
- rel_i^j represents the relativistic effect.
- T_i^j is the tropospheric delay.
- $STEC_i^j$ represents the integral of electron density in the ionosphere along the slant ray path, i.e. Slant Total Electron Content (STEC), and $\alpha_i = 40.3/{f_i}^2$.
- K_i^j represents the delays due to the instrumental constants of satellite and receiver, which are dependent on the frequency.
- $M_{P,i}^j$ and $m_{L,i}^j$ represent the effect of multipath on pseudorange and carrier phase respectively, also depending on the frequency.
- $\varepsilon_{P,i}^j$ and $\varepsilon_{L,i}^j$ represent a noise term containing all unmodeled effects.
- B is an ambiguity phase term owing to the signal acquisition, an ambiguity of an integer number of wavelengths ($N\lambda$) appears to which one has to add phase instrumental terms k_i, k^j from satellite and receiver, respectively ($B_i^j = k_i + k^j + \lambda N_i^j$).

- $\omega_L = \lambda_i \phi$ is a term due to signal polarization (wind-up), where ϕ is the relative transmitter-receiver antenna angle.

1.1.2 Ionospheric combination

The ionospheric combination is of interest in the ionosphere modeling. It cancels the geometric part of the measurement and in general the non-frequency dependent terms. It is also called geometry-free combination, leaving the ionospheric delay, the slowly varying instrumental delays, multipath and observational noise. The ionospheric combinations *PI* and *LI* in pseudorange and carrier phase observables are defined as below:

$$\begin{aligned} PI_i^j &\equiv P2_i^j - P1_i^j \\ &= 40.3(\frac{1}{f_2^2} - \frac{1}{f_1^2})\mathrm{STEC}_i^j + (K2_i^j - K1_i^j) + (M_{P2,i}^j - M_{P1,i}^j) + (\varepsilon_{P2,i}^j - \varepsilon_{P1,i}^j) \end{aligned} \tag{1.5}$$

$$\begin{aligned} LI_i^j &\equiv L1_i^j - L2_i^j \\ &= 40.3(\frac{1}{f_2^2} - \frac{1}{f_1^2})\mathrm{STEC}_i^j + (B2_i^j - B1_i^j) + (m_{L2,i}^j - m_{L1,i}^j) + (\omega_{L2,i}^j - \omega_{L1,i}^j) + (\varepsilon_{L2,i}^j - \varepsilon_{L1,i}^j) \end{aligned} \tag{1.6}$$

1.2 Ionospheric tomography with GNSS

Dual-frequency GNSS data have been widely recognized as important measurements for modeling and monitoring the ionosphere (Hernández-Pajares et al., 2011). In the TOmographic Model of the IONosphere (TOMION) version 1 — TOMIONv1, proposed by Hernández-Pajares et al. (1999), only dual-frequency carrier phase measurements are used to derive the ionospheric delay. Two advantages of this tomographic model are: 1) not using pseudorange measurements with larger noise increase the precision; 2) the tomographic approach reduces mismodeling brought by the single layer assumption, particularly when there are large Total Electron Content (TEC) gradients. The more accurate and precise STEC estimation by tomography can help increase the ambiguity resolution success rate in Real-Time Kinematic (RTK) or Wide-Area RTK (WARTK) (Hernández-Pajares et al., 2002) (Hernández-Pajares et al., 2000b).

1.2.1 From ground-based measurements only

The tomography with two vertical layers are adopted to estimate the vertical electron content distribution when only ground-based GNSS measurements are ingested. The use of two layers can be understood as a model with a variable effective height driven by the data. And the 3D voxels are set in Sun-fixed reference frame where the electron distribution is more stationary. Using *LI* combination observations, the mean electron densities in the illuminated voxels and the combined ambiguity terms are estimated simultaneously after cycle slip detection. The combination of ionosonde and GNSS data can achieve better estimation of vertical electron content structure with more vertical layers (Hernández-Pajares et al., 1999).

1.2.2 From LEO-based measurements

Low Earth Orbit (LEO) based radio occultation (RO) data provide valuable measurements for ionosphere study. The two main ways of modeling electron density distribution are tomographic models with low vertical resolution (Hernández-Pajares et al., 1998; Leitinger et al., 1997) and the Abel inversion with higher vertical resolution (Hajj and Romans, 1998). This section briefly reviews two aspects: the contribution of RO data to the improvement in tomographic models and the performance enhancement of Abel inversion by taking into account the horizontal electron content gradient.

LEO and ground-based data combined in a voxel-based tomographic model

GPS measurement from LEO satellites can improve the geometry for the tomographic model. The ingestion of LEO-based GNSS data is able to improve the vertical resolution. The tomographic model with eight vertical layers is solved by Kalman filtering, assuming a random walk process for the electron density in the Sun-fixed coordinate system, also during space weather events (Hernández-Pajares et al., 1998). The improvement of estimation accurary of electron density can be seen in Figure 3 of Hernández-Pajares et al. (1998).

Inversion of radio-occultation LEO measurements: improved Abel inversion and dual-layer POD electron content modeling

The Abel inversion is another useful technique to estimate electron density profile in radio-occultation scenarios. In the traditional Abel inversion, the error sources are mainly brought by the spherical symmetry assumption and by neglecting the electron density above LEO orbit height. In order to mitigate the error caused by spherical symmetry assumption, the separability concept was proposed by introducing VTEC as providing the relative horizontal

variation proxy for the electron density and shape function as new unknown, instead of the electron density, in the modified Abel inversion (Hernández-Pajares et al., 2000a). By applying the topside electron content correction derived from Precise Orbit Determination (POD) measurements, negative values of estimated electron density at low altitudes can be removed (Hernández-Pajares et al., 2017a).

1.3 Global Ionospheric Maps

Through dSTEC validation and Altimeter-VTEC assessment, the rapid Universitat Politècnica de Catalunya (UPC) Global Ionospheric Map (GIM), UQRG, has the best overall performance among other UPC GIMs and GIMs from other International GNSS Service (IGS) ionospheric analysis centers (Feltens et al., 2011; Hernández-Pajares et al., 2017c; Roma-Dollase et al., 2018). This section describes how UQRG is generated and its by-product μ_2.

1.3.1 UQRG VTEC GIM

The two crucial techniques to generate UQRG GIM are tomographic estimation and kriging interpolation, with dual-frequency measurements gathered from 150-250 globally distributed GPS receivers as input.

In the tomographic estimation, one simplication is that the whole ionosphere is condensed in the altitude range from 110 km to 1470 km. Another assumption is that the electron density is homogeneously distributed in each voxel, which is the basic 3D volume element, in a Sun-fixed reference frame for the case of VTEC GIMs computed from ground GNSS data. The condensed ionosphere is splitted into 1017×2 isotropic voxels in horizontal and vertical dimensions respectively, with the size of each voxel in horizontal dimension an adaptive setting up increasing from smaller angular spacing at the equator to larger angular spacing at high latitudes and in vertical dimension 680 km as the thickness. The varying horizontal splitting is adopted to avoid the estimation problem caused by the sparsity of illumination and not to lose the sensitivity to horizontal gradient (Hernández-Pajares et al., 1997). Specifically, the voxel size can be increased to ensure the minimum number of Lines Of Sight(LOSs) illuminating one voxel allowing the estimation and also can be decreased in the region where more LOS number is available to present more detailed horizontal gradient. Each STEC observation is described as the sum of the integral of electron density in all illuminated voxels. Therefore, the observation equations are given as follows:

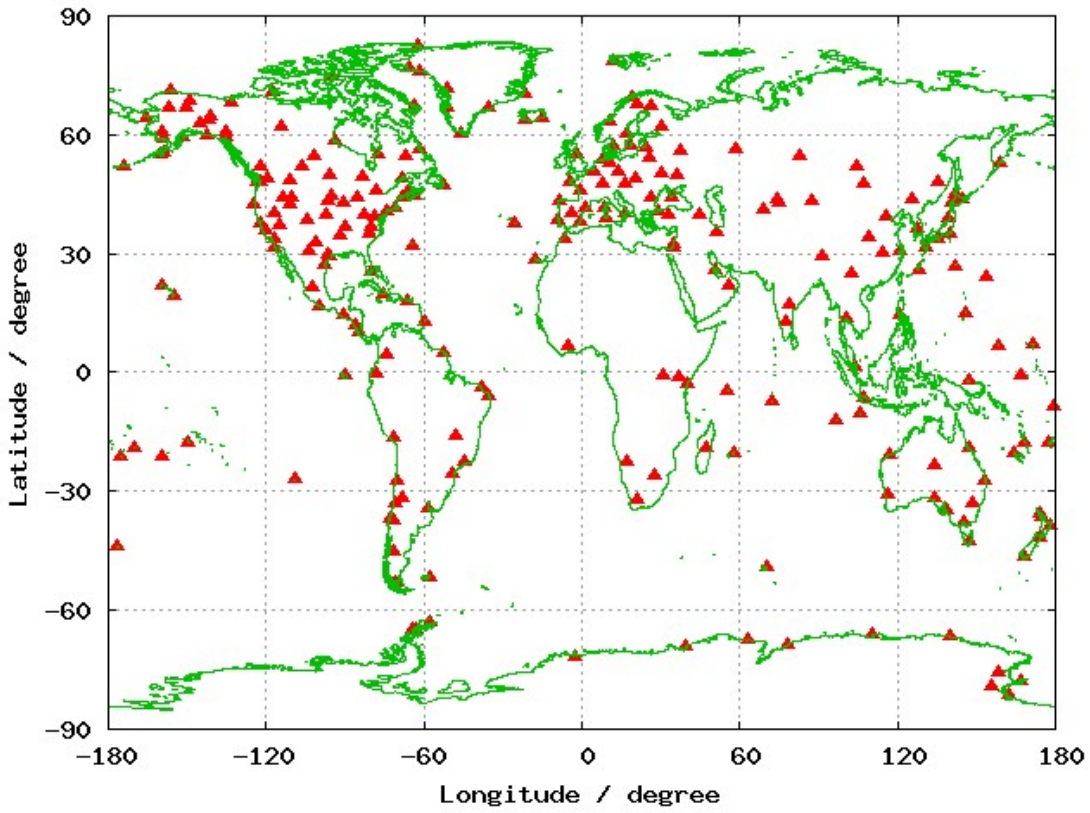

Figure 1.1 Global distribution of IGS GPS stations used in generation of UQRG GIM on day 152 of year 2009

$$LI - (\lambda_1 - \lambda_2) \cdot \phi = \sum_{i=1}^{M_I} \sum_{j=1}^{M_{J(i)}} \sum_{k=1}^{M_K} (N_e)_{i,j,k} \cdot \Delta l_{i,j,k} + BI \tag{1.7}$$

where the wind-up term $(\lambda_1 - \lambda_2) \cdot \phi$ is corrected from LI; the index (i,j,k) represents the voxel, with i in latitude, j in local time and k in height respectively; M_I, $M_{J(i)}$ and M_K are the maximum number of voxels in three dimensions; $\Delta l_{i,j,k}$ represents the ray-path-length inside each illuminated voxel (i,j,k), which is computed by the very good approximation of straight-line propagation.

Firstly, the mean electron density $(N_e)_{i,j,k}$ of the voxels, together with the ambiguity term BI, is estimated by a forward Kalman filter, modeling the mean electron densities as random walk process in a Sun-fixed reference frame, and the ambiguities as random variables. To avoid repetition, the advantage of the tomographic model is no longer described here.

Following is the interpolation to fill the gaps of measurements, due to the lack of a good coverage of GPS receivers. This lack of data is compounded especially over the oceans, Siberia and the Southern Hemisphere, e.g. Central Africa and partial south polar region

(Figure 1.1). At first, STEC for each measurement can be directly derived according to the equivalent version of Equation (1.7): $\hat{STEC} = ((LI - (\lambda_1 - \lambda_2) \cdot \phi - \hat{BI}))/\alpha$, where $\hat{BI}$ is taken as the best estimation of the combined ambiguity in the continuous phase arc of each GNSS transmitter-receiver pair, typically the last one in one phase-continuous arc. Then, it is easy to obtain VTEC, converted from the estimated STEC value by using the single-layer ionospheric mapping function with the fixed height 450 km, adopted in IGS community. Finally, the Kriging technique, which efficiently takes into account the decorrelation length of the ionospheric modeling error (Orús et al., 2005), is applied on the residuals of individual VTEC values regarding the initial VTEC GIM computed by means of splines-based interpolation.

Finally, the differential code biases (DCBs) are estimated from combined pseudorange measurements *PI* by substracting the ionospheric delay computed from the generated GIMs. By adding the gravity datum of satellite code biases (the sum of them is taken as zero), receiver code bias and satellite code bias are solved.

1.3.2 Vertical distribution - μ_2

In addition to the final GIM product of the tomographic run, the fraction of the second-layer vertical electron content, μ_2 parameter, can be derived from the estimated electron densities in two vertical voxels situated at the same horizontal location. Since the two vertical voxels have the same size in height (680 km in the GIM's computation), μ_2 can be written as the ratio of electron densities as follows:

$$(\mu_2)_{i,j} = \frac{(N_e)_{i,j,2}}{(N_e)_{i,j,1} + (N_e)_{i,j,2}} \tag{1.8}$$

where $(N_e)_{i,j,1}$ and $(N_e)_{i,j,2}$ respectively represent the electron density at the first layer and the second layer for the same horizontal voxel indexed with (i,j).

μ_2 is obtained from the direct estimation in the tomographic model, and stored internally at UPC premises during the daily runs performed since June 1998 within the IGS. μ_2 is not only an indicator of the relative vertical distribution of free electrons, which was used to analyze the main trough (Hernández-Pajares et al., 2020a), but also a useful driver of an improved ionospheric mapping function (Lyu et al., 2018b).

1.4 Thesis breakdown

Following the Introduction, four works are presented in Chapter 2, 3, 4 and 5: Improvement of the vertical ionospheric electron content distribution for ground-based users: BIMF-nml; Study of the electron content distribution in polar regions from UQRG; Improvement of the Abel inversion of top-truncated RO ionospheric data: AVHIRO; A new way of improving Global Ionospheric Maps by ionospheric tomography based on multi-Space Geodetic dual-frequency measurements. Afterwards, it comes to Quality Indexes and the Conclusions.

Chapter 2

An improved ionospheric mapping function for mid-latitude GNSS users: BIMF-nml

2.1 Introduction

Ionospheric error is one significant error source in GNSS positioning, in particular for Standard Point Positioning (SPP). To mitigate the ionospheric error, broadcast model parameters like Klobuchar model for GPS (Klobuchar, 1987) and NeQuick model for Galileo (Angrisano et al., 2013), empirical models like International Reference Ionosphere (IRI) (Bilitza, 2001), NeQuick (Nava et al., 2008) and the Neustrelitz TEC Model (NTCM) (Jakowski et al., 2011), global or regional ionospheric maps (GIMs or RIMs) (Hernández-Pajares et al., 2011) (Aa et al., 2015), and numerical models provided by the Satellite-Based Augmentation Systems (SBAS) (Hernández-Pajares et al., 2005) can be utilized to calculate VTEC and then STEC is converted from VTEC by ionospheric mapping function. Accurate STEC information is critical not only for SPP, but also for relative positioning, such as RTK or WARTK (Hernández-Pajares et al., 2000b). When the baselines among the reference stations increase, the ambiguity resolution success rate can decrease due to the poor spatial dependence of the atmospheric delay. If more accurate STEC values could be provided, the ambiguity resolution success rate would be improved significantly (Hernández-Pajares et al., 2002).

The traditional ionospheric mapping function is based on a single-layer assumption with fixed effective height, which can lead to big conversion errors especially for low elevation. In fact, the ionospheric effective height, i.e. the optimal height to represent the ionospheric

electron content within a single spherical and geocentric thin layer, mainly varies with geographical location, local time, season, and solar activity since it depends on the electron density distribution and on the elevation angle above the horizon of the receiver–transmitter line-of-sight. In general, the effective height is set in a range between 350 km and 450 km. Different ranges of shell height in certain regions have been investigated (Birch et al., 2002; Niranjan et al., 2007). To overcome the mapping error caused by the constant shell height, the concept of varying effective heights was proposed (Komjathy and Langley, 1996), but it is difficult to measure the proper shell height (Sakai et al., 2001). The mapping function obtained from Multi-layer shell model (Sakai et al., 2001), chapman and IRI model (Hoque and Jakowski, 2013; Zus et al., 2017), considering the vertical electron density distribution, is another research direction.

The Barcelona Ionospheric Mapping Function was proposed to improve the STEC corrections from VTEC models in GNSS applications at northern mid-latitudes (BIMF-nml). It is based on a climatic prediction of the distribution of the topside vertical electron content fraction of VTEC, i.e. μ_2, as introduced in Section 1.3.2. This forecasting model has been derived from the daily runs of the TOmographic Model of the IONosphere (TOMION) software, performed to generate the UPC GIMs in IONosphere map EXchange format (IONEX) for IGS during the last 20 years. In order to assess the performance of the new ionospheric mapping function, the precise STEC difference (dSTEC) values that are not used in GIM generation are selected as independent true values. It is shown that, in terms of GIM STEC estimation, BIMF outperforms the standard ionospheric mapping functions with 450 km shell height, which is adopted by IGS and the one with 350 km shell height, which is used by SBAS. The improvement is clear not only for UPC GIMs, which already use a tomographic model, with up to 8% and 15% of enhancement for shell heights of 450 km and 350 km respectively for the year 2014, but especially for CODE GIMs, with up to 22% and 32% of improvement respectively, and for JPL GIMs, with up to 21% and 29% of improvement respectively.

2.2 Two-layer assumption

When GIMs, or any VTEC model, are used to correct the ionospheric delay in space geodetic measurements such as GNSS, the slant delay for each signal is computed by multiplying the vertical delay at the IPP location by an obliquity factor, i.e., using a mapping function under the single-layer assumption. The most commonly used mapping function, which will be called the standard mapping function in this study, is described as follows:

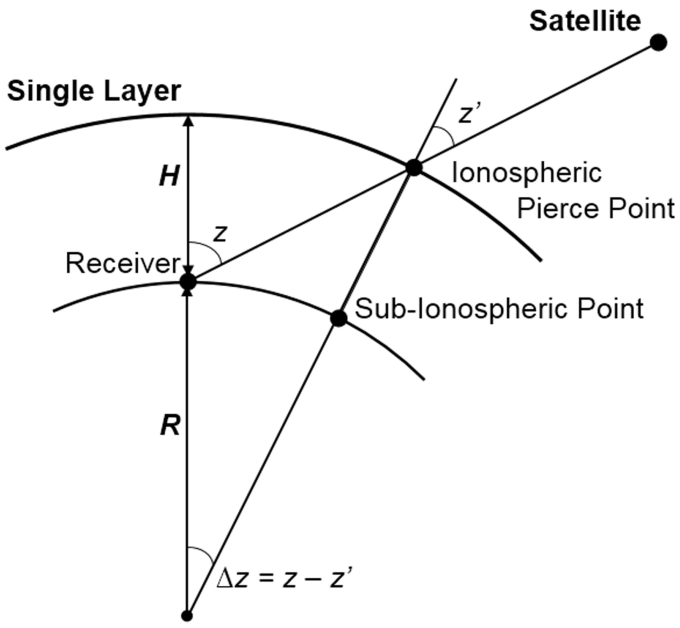

Figure 2.1 Single-layer model for the ionosphere

$$M = \frac{STEC}{VTEC} = \frac{1}{cosz'} \tag{2.1}$$

where STEC is computed along the signal ray-path, and VTEC and z' are defined at the IPP (Figure 2.1)

As mentioned in Section 1.3, the two-layer tomographic model has been adopted for the daily computation of UPC GIMs since the IGS Ionospheric Working Group started on June 1, 1998 (Hernández-Pajares et al., 2009), which is implemented in the TOmographic Model of the IONosphere (TOMION) software (Hernández-Pajares et al., 1997). The ionospheric electron content by two spherical geocentric layers is significantly better for fitting the ground-based GNSS measurements than the single layer and for computing the VTEC (Hernández-Pajares et al., 1997, 1999; Juan et al., 1997). The first ionospheric layer is defined as between 110 and 790 km, with a central height of 450 km, which is also the assumed effective height in VTEC GIMs generated within IGS. The second layer is from 790 to 1470 km, coinciding with the typical topside layer definition for Low Earth Orbiting satellites with on-board GPS receivers such as FORMOSAT-3/COSMIC (Hernández-Pajares et al., 2017a), with a central height of 1130 km (Figure 2.2). Although the thickness of the condensed ionosphere is 1360 km (1470 minus 110 km), it actually includes the electron content of the whole ionosphere and plasmasphere up to the GPS height, with two effective heights at the central values of 450 and 1130 km. In addition, each layer is divided into

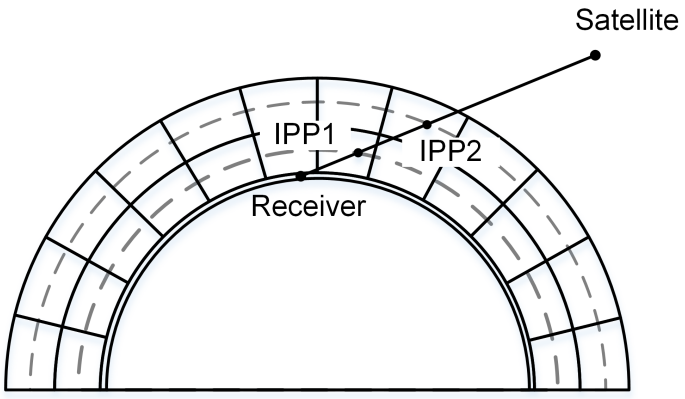

Figure 2.2 Segmentation diagram of STEC for a given GNSS ray under the two-layer assumption. IPP1 and IPP2 are the intersection points of the receiver-to-satellite line-of-sight with the first and the second central heights, respectively

volume elements (voxels) of few degrees in longitude and latitude. The corresponding geometric factors for each layer, denoted by M_1 and M_2, are used in the UPC TOMION runs to estimate the vertical distribution of electron content among the top and bottom voxels.

For the top and bottom voxels at given horizontal location, following the definition of μ_2 (see Section 1.3.2), we simplify the notation in the formula of two ratio values μ_1 and μ_2 as shown in Equation 2.2:

$$\begin{aligned} \mu_1 &= \frac{N_1}{N_1+N_2} = \frac{P_1}{P_1+P_2} = \frac{P_1}{V} \\ \mu_2 &= \frac{N_2}{N_1+N_2} = \frac{P_2}{P_1+P_2} = \frac{P_2}{V} \end{aligned} \tag{2.2}$$

where N_1 and N_2 are the mean electron densities for the first and second layers, respectively. V is VTEC for the whole ionosphere, and P_1 and P_2 are the partial vertical electron contents for the first and second layer, respectively. We assume that the vertical profile is simplified as consisting of just two points, instead of hundreds of points when it is estimated from radio-occultation measurement inversion (Hernández-Pajares et al., 2000a). Then, the ratios μ_1 and μ_2 can be interpreted as a coarse shape function of only the bottomside and the topside layers, respectively, i.e. the relative ratio of mean electron density N_1 and N_2. So these ratios are also equivalent to vertical partial electron contents for the first and second layers, as both layers have equal thicknesses.

To simplify applying μ_1 and μ_2, obtained from the database of UPC TOMION, the given slant TEC for a particular ray can be divided into two parts by neglecting the horizontal gradients within each layer:

$$\begin{aligned} STEC &= N_1 l_1 + N_2' l_2' \\ &= H \cdot \frac{N_1 l_1}{H} + H \cdot \frac{N_2' l_2'}{H} \\ &= P_1 \cdot M_1 + P_2' \cdot M_2' \\ &= M_1 \cdot \mu_1 V + M_2' \cdot \mu_2' V' \\ &= (1-\mu_2) M_1 V + \mu_2' M_2' V' \end{aligned} \tag{2.3}$$

where H is the common thickness of each layer; l_1 and l_2' are the lengths of the part of the ray included in the first layer and in the second layer; N_1 and N_2' are the electron densities of the first layer and the second layer where the ray passes; P_1 and P_2' are the partial vertical electron contents of each layer crossed by the GNSS ray; V and V' are VTECs for the whole ionosphere at IPP1 and IPP2, respectively; μ_2 and μ_2' are the shape functions of the voxels for the second-layer corresponding to IPP1 and IPP2; M_1 and M_2' are the standard mapping functions at IPP1 and IPP2, equal to l_1/H and l_2'/H, respectively. Equation 2.4 presents the idea behind BIMF; since μ_2 refers to the shape function of the second layer, this ratio corresponds to a first approximation of the vertical distribution of the ionospheric electron density.

To apply the new mapping function we can consider two approaches:

- On the one hand, a nowcasting μ_2 could be directly based on the daily UPC tomographic runs, after grid interpolation and applied in a similar way as the GIMs (IONEX format).
- On the other hand, as a more challenging approach on the determination of the mapping function but simpler for user applications, a forecasting μ_2 could be provided in terms of a climatic function of space and time for a given range of latitudes, such as mid-latitudes.

It is important to remark that in the second case, the users do not need any external information, which could be of great interest compared with the approach of nowcasting μ_2. In the next section, μ_2 variation characteristics will be analyzed in this regard.

2.3 Daily variation characteristics of μ_2

TOMION was developed at UPC to compute the daily GIMs in the context of IGS. It uses a two-layer tomographic approach that takes the distribution of the electrons in the outer part of the ionosphere into consideration. The resulting Global Ionospheric Maps, using

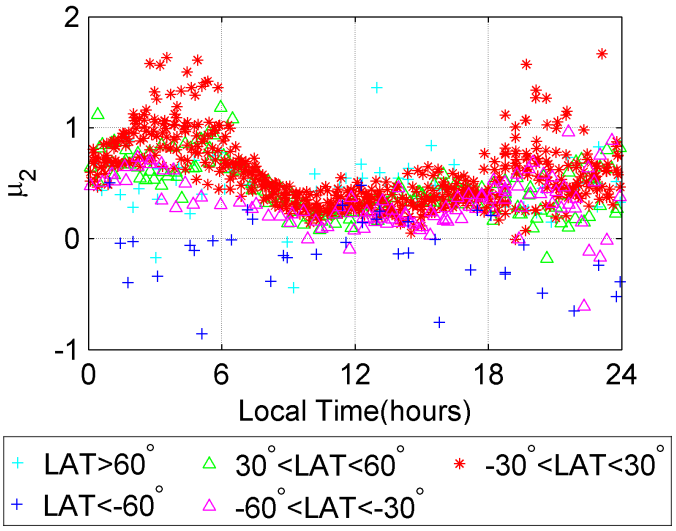

Figure 2.3 Daily variations of μ_2 for different latitude ranges on day of year (DOY) 349, 2006

Kriging interpolation and provided with latency of 1-2 days to the IGS every 15 minutes, are identified as "UQRG" (Orús et al., 2005; Roma-Dollase et al., 2018). Therefore, TOMION runs allow to have a valuable long-term database for μ_2 available since the mid-1998.

Most of the latitude bands show similar daily μ_2 variations as can be seen from the example shown in Figure 2.3, except in the southern area of 60°S due to the scarcity of data. It can be observed that the upper shape function μ_2 reaches its peak at about 4:00 Local Time (LT), which is consistent with the expected relevant role played by the plasmasphere during the night; the valley region occurs approximately between 8:00 and 17:00 LT. It is noticeable that the μ_2 values are systematically higher at night time than at daytime, which is linked to the daily variation of vertical electron density distribution. Thus, to overcome the limitation brought by the fixed single-layer height, it is reasonable to use the μ_2 ratio to improve the standard mapping function.

It is worth mentioning that μ_2 can be:

- Slightly negative, when the $P_2 = N_2 \cdot H$ the partial electron content of the second layer with thickness H is slightly negative. This happens when almost all the electron content is placed below the effective height of the first layer (450 km).

- Slightly larger than one with $P_1 = N_1 \cdot H$ the partial electron content of the first layer slightly negative, when almost all the electron content is placed above the effective height of the second layer (1130 km).

It can be demonstrated from the following approximation:

$$STEC = M_1 \cdot P_1 + M_2 \cdot P_2 = M \cdot V \tag{2.4}$$

The mapping function M_1, M_2 and M depend on the effective height. The greater the effective height is, the smaller the mapping function is. H_1 and H_2 are defined as 450 km and 1130 km, the central height for each layer, corresponding to M_1 and M_2. And H represents the real effective height, corresponding to M.

When H is greater than H_2, e.g. during the nighttime when most of the electron density is distributed in the plasmasphere, then $H>H_2>H_1$ and thus $M_1>M_2>M$. The equation 2.4 can be written as

$$(M_1 - M) \cdot P_1 = (M - M_2) \cdot P_2 \tag{2.5}$$

It can be seen that $M_1 - M$ is positive and $M - M_2$ is negative, which means that P_1 and P_2 have opposite signs. Since $V = P_1 + P_2$ must be positive and $|P_2| > |P_1|$. So we get positive P_2 and $P_2 > V$. Therefore, $\mu_2 = P_2/V$ is greater than 1.

In the case that most of the electron density is distributed below 450 km, positive P_1 and negative P_2 can be similarly deduced by means of equation 2.5, thus negative μ_2.

The negative P_1 and P_2 seem unreasonable at the first glance based on their definition. But from the point of view of modeling, it is consistent with the assumption of the two layers where electron density is homogeneously distributed. So from real data and the simplified dual-layer model, whether μ_2 is negative or greater than 1, both cases can be derived and represent realistic electron density distribution.

Considering that μ_2 is obtained from actual measurements, the mapping VTEC to STEC using μ_2 values is expected to give more realistic results compared to the standard mapping function approach.

The modeling and assessment of BIMF will be performed in the following sections, under the methodology summarized in Figure 2.4.

2.4 BIMF modeling based on μ_2

We are focusing on northern mid-latitude regions, such as Europe with many permanently installed receivers operating, specifically in the latitude range from 30°N to 60°N as the main research region. For this purpose, the μ_2 variation with respect to latitude is neglected for the area under consideration.

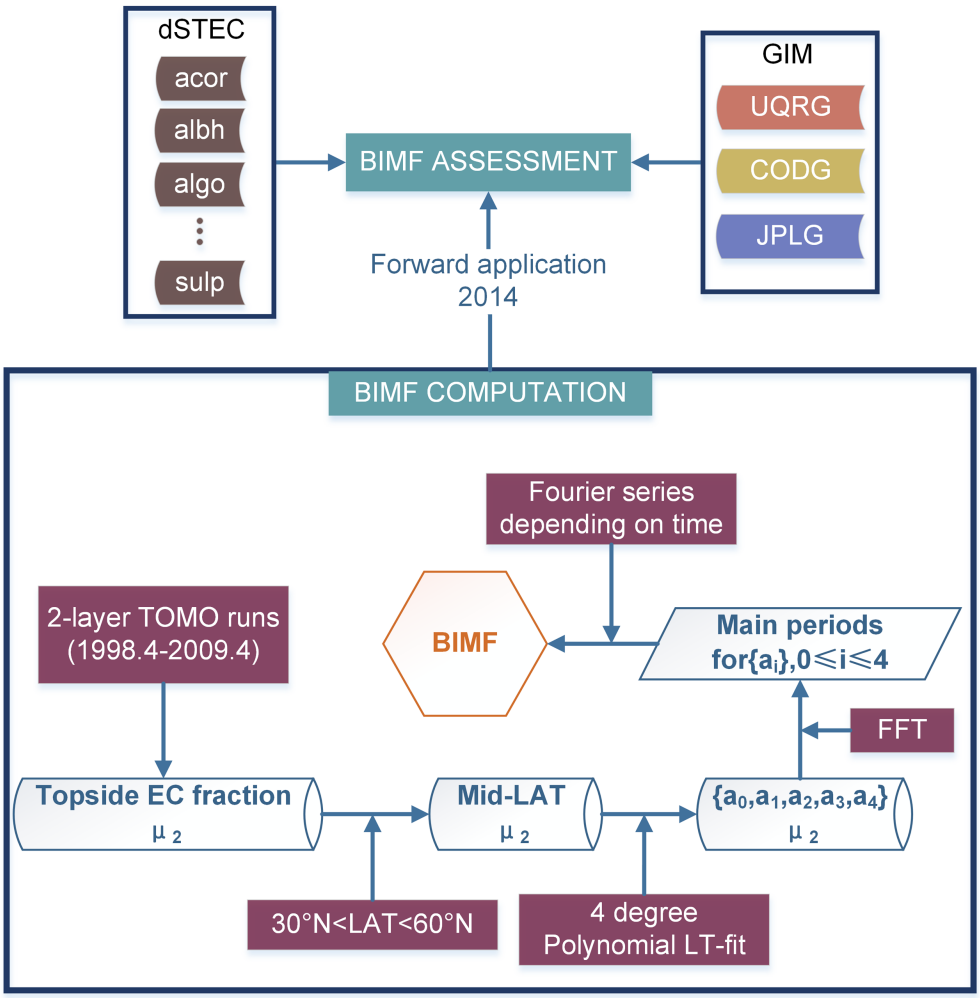

Figure 2.4 Diagram of BIMF modeling and assessment

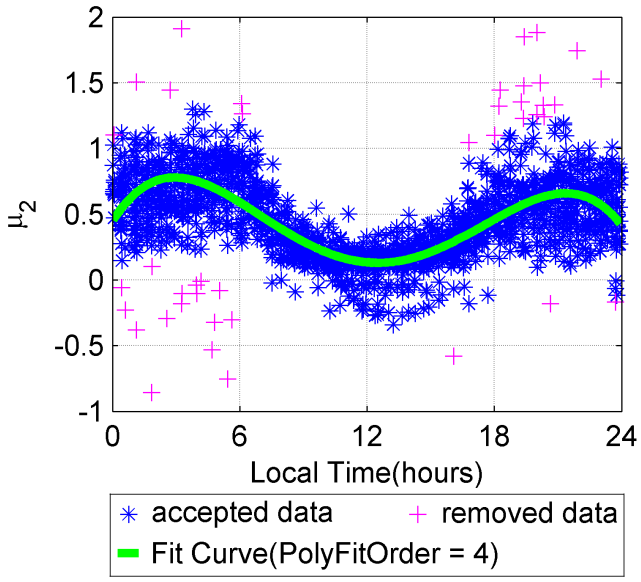

Figure 2.5 Example of daily variation of polynomial fitting of μ_2 for northern mid-latitudes (DOY 349, 2006)

First, for each given day in the study region, the μ_2 parameter is modeled as a fourth-order polynomial of local time, since by comparison of different orders, we found that such fitting of the daily μ_2 variation with local time is a good compromise between accuracy and simplicity,

$$\mu_2(lt) = a_0 + a_1 \cdot lt + a_2 \cdot lt^2 + a_3 \cdot lt^3 + a_4 \cdot lt^4 \tag{2.6}$$

where a_i represents the polynomial coefficients and lt is the local time. To estimate the parameters, we use equally-weighted least squares and remove observation data with residuals greater than three times the root mean square error (outliers). The time series of polynomial coefficients (a_0, a_1, a_2, a_3 and a_4) are obtained from the dual-layer TOMION runs during one solar cycle, beginning on June 1, 1998. An example for the polynomial fitting for the day 349 of the year 2006 and related daily μ_2 data are given in Figure 2.5.

As a second step, the predominant period terms of each coefficient are determined using a Fast Fourier Transform (FFT) for the 11-year time series, corresponding to one solar cycle period (Tables 2.1, 2.2, 2.3, 2.4 and 2.5). As shown in Figure 2.6, the coefficients a_1 to a_4 show the clear presence of three main periods corresponding to 365.2, 182.6 and 121.7 days, in concordance with three main seasonal components found by Hernández-Pajares et al. (2009) for the Global Electron Content (GEC), introduced by Afraimovich et al. (2008). The predominant periods of the constant term a_0 are more complex.

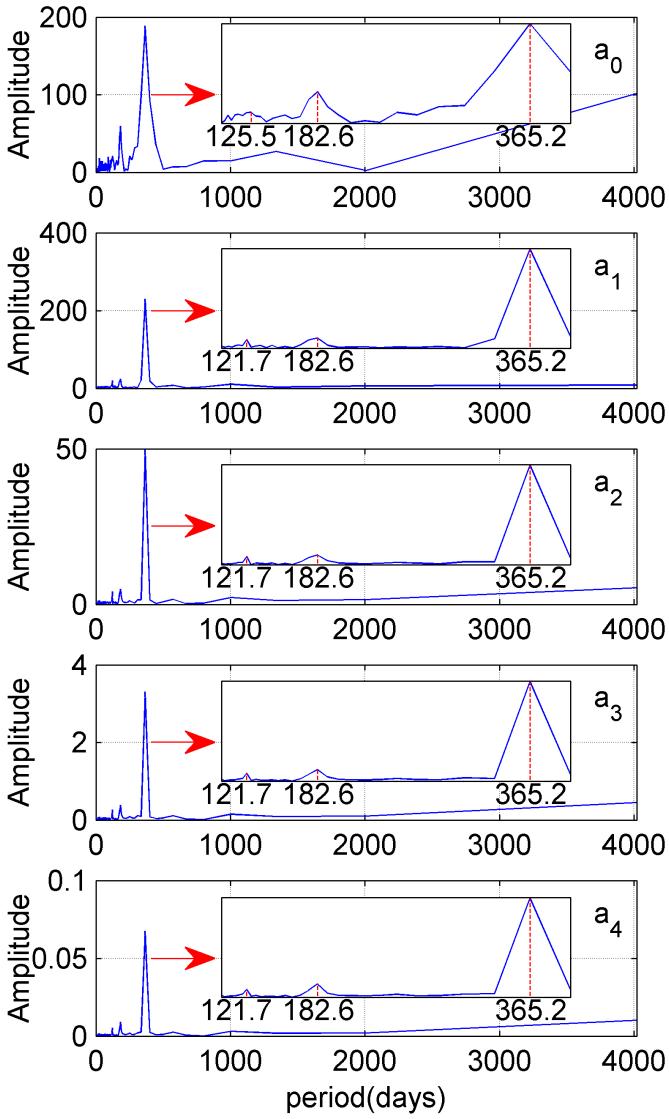

Figure 2.6 Fast Fourier transform of five coefficients time series data from the daily TOMION runs from 1998.4 to 2009.4

After analyzing the temporal variation of μ_2, we obtain the μ_2 model. For IPPs with latitudes between 30°N and 60°N, the μ_2 parameter is expressed as a function of the number

Table 2.1 Coefficients of a_0

k	$T_0^{(k)}$	$C_0^{(2k-1)}$	$C_0^{(2k)}$
0			6.778886E-01
1	365.2	-8.688163E-02	3.578382E-02
2	4017.0	-4.430154E-02	2.439461E-02
3	182.6	-1.869270E-02	-2.323595E-02
4	1339.0	-1.333096E-02	-1.128014E-03
5	125.5	-1.006658E-02	-3.188399E-03
6	26.43	-6.209667E-03	-6.513369E-03

Table 2.2 Coefficients of a_1

k	$T_1^{(k)}$	$C_1^{(2k-1)}$	$C_1^{(2k)}$
0			8.854738E-02
1	365.2	-4.889833E-02	-1.037872E-01
2	182.6	1.211679E-02	5.830693E-04
3	121.7	8.548938E-03	5.303727E-03

Table 2.3 Coefficients of a_2

k	$T_2^{(k)}$	$C_2^{(2k-1)}$	$C_2^{(2k)}$
0			-2.925523E-02
1	365.2	1.111281E-02	2.224605E-02
2	182.6	-2.409684E-03	4.900974E-04
3	121.7	-1.681305E-03	-1.170320E-03

Table 2.4 Coefficients of a_3

k	$T_3^{(k)}$	$C_3^{(2k-1)}$	$C_3^{(2k)}$
0			2.062601E-03
1	365.2	-7.358248E-04	-1.475076E-03
2	182.6	1.864769E-04	-4.539838E-05
3	121.7	1.047826E-04	8.154671E-05

of days since the modified Julian day 50,965 (DOY 152, 1998) and in the local time in hours. The fourth-order polynomial function becomes:

$$\mu_2(td,lt) = a_0(td) + a_1(td)\cdot lt + a_2(td)\cdot lt^2 + a_3(td)\cdot lt^3 + a_4(td)\cdot lt^4 \tag{2.7}$$

$$a_i(td) = C_i^{(0)} + \sum_{k=1}^{n(T_{a_i})} (C_i^{(2k-1)}\cdot sin(2\pi\cdot\frac{td}{T_i^{(k)}}) + C_i^{(2k)}\cdot cos(2\pi\cdot\frac{td}{T_i^{(k)}})) \tag{2.8}$$

where lt is the local time of the IPP, $td = mjd - 50965$, and mjd is the modified Julian day. In addition, $C_i^{(0)}$ is a constant term; $C_i^{(2k-1)}$ are the coefficients of the sine terms; $C_i^{(2k)}$ are the coefficients of the cosine terms; $T_i^{(k)}$ is the k-th period of the polynomial coefficient a_i; $n(T_{a_i})$ is the number of dominant periods of a_i. In this context, Tables 2.1, 2.2, 2.3, 2.4 and 2.5 give the BIMF values for these parameters.

For each polynomial coefficient, the Fourier series fitting is compared with the data from the first step. As can be seen from Figure 2.7, the Fourier series can properly predict the coefficients for periods not used in the modeling. In the case of the constant term, a_0, there is still room for future modeling, maybe in the context of latitudinal dependence. But in general the BIMF is performing reasonably well as a climatological model and might be suitable for prediction of the mapping function after direct assessment of the improvement in the STEC retrieval from VTEC models, as can be seen in Section 2.5.

The main dependences of the final fitted μ_2 are shown in Figure 2.8, 2.9, 2.10. In particular in Figure 2.8 for the year 2014, the higher values of μ_2 occur during the nighttime, as expected. Semi-annual and nearly monthly periods can be seen as well in the VTEC results presented by Hernández-Pajares et al. (2009). The almost 27-day period is compatible with the solar rotation period, and this is consistent with the dependence of the geo-effective solar flux associated to sunspots. A simultaneous view of local time and season dependence is shown in Figure 2.9, where μ_2 presents the highest values in fall and winter seasons. The dependence for more than one solar cycle is presented in Figure 2.10, with highest values

Table 2.5 Coefficients of a_4

k	$T_4^{(k)}$	$C_4^{(2k-1)}$	$C_4^{(2k)}$
0			-4.167004E-05
1	365.2	1.478527E-05	3.013404E-05
2	182.6	-4.442136E-06	1.020289E-06
3	121.7	-2.044199E-06	-1.758158E-06

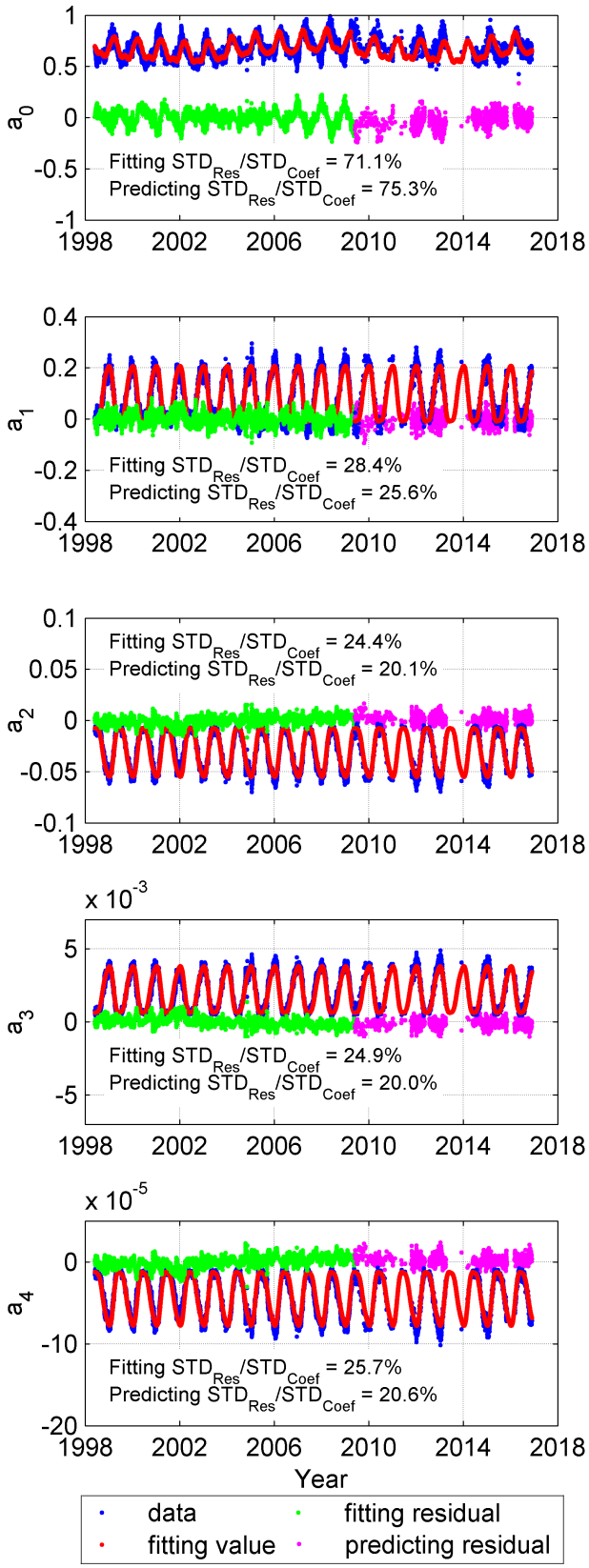

Figure 2.7 Results of Fourier series fitting of five polynomial coefficients from a_0 to a_4. The green and pink dots are the residuals for the dataset used in the time series fit and the residuals when using the predicted values, respectively. The percentages of standard deviation (STD) of residuals relative to the coefficient STD are also given in the plots

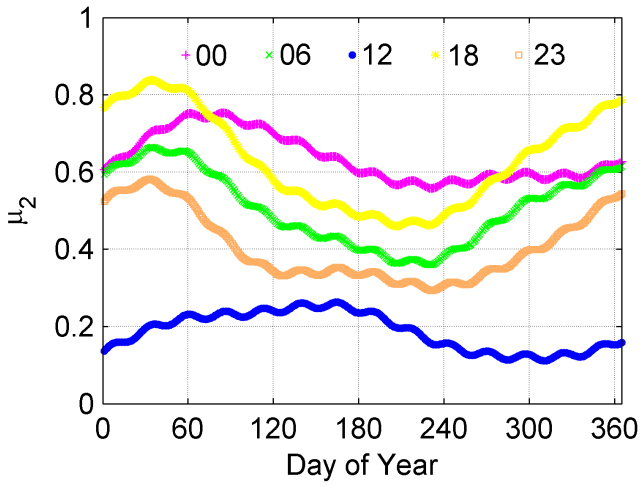

Figure 2.8 Predicted values of μ_2 by BIMF-nml during 2014 for different local time versus day of year

of μ_2 occurring during solar minimum, indicating a small reduction of the topside electron content compared with the bottom-side ionosphere reduction.

Finally, the Barcelona Ionospheric Mapping Function for northern mid-latitudes can be depicted with a revised notation as follows:

$$STEC = (1-\mu_2^{ipp1})M_1^{ipp1}V^{ipp1} + \mu_2^{ipp2}M_2^{ipp2}V^{ipp2} \tag{2.9}$$

where V^{ipp1} and V^{ipp2} are VTECs at IPP1 and IPP2, respectively; M_1^{ipp1} and M_2^{ipp2} are standard mapping functions at IPP1 and IPP2, respectively; and μ_2^{ipp1} and μ_2^{ipp2} are μ_2 ratio values at IPP1 and IPP2, respectively (see Figure 2.11).

2.5 Assessment

According to previous research we can consider very precise and accurate slant electron content difference, hereinafter dSTEC or ΔS, directly obtained from the carrier phase measurements not affected by cycle-slips and independently of any ionospheric model as the reference truth. In addition, the dSTEC observable is very sensitive to the changes of the electron content with elevation and time. Some of the previous applications of dSTEC for the assessment of ionospheric models can be seen in Feltens et al. (2011); Hernández-Pajares et al. (2011); Orús et al. (2005), and more recently in Hernández-Pajares et al. (2017c). dSTEC has been used to compare the performances of different ionospheric models in the IGS context (Roma-Dollase et al., 2018).

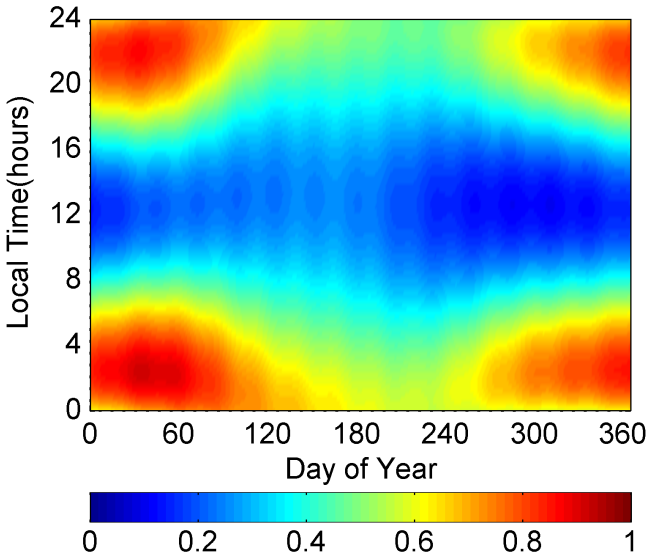

Figure 2.9 Predicted values of μ_2 by BIMF-nml from 2000 to end of 2017 for the night- and day-time (02:00 and 14:00 LT)

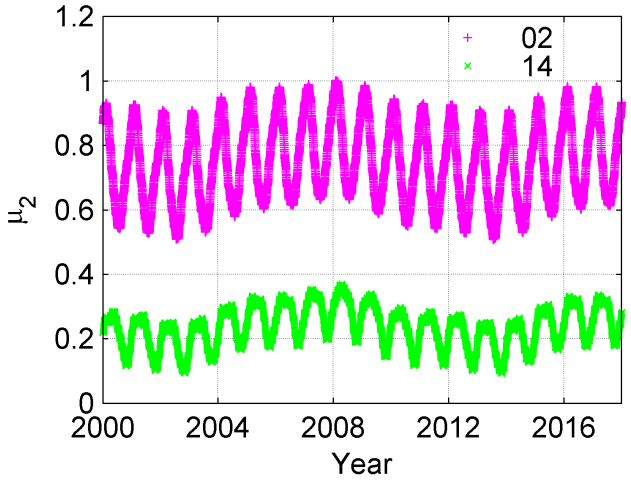

Figure 2.10 Predicted values of μ_2 by BIMF-nml during 2014 as a function of local time and day of year

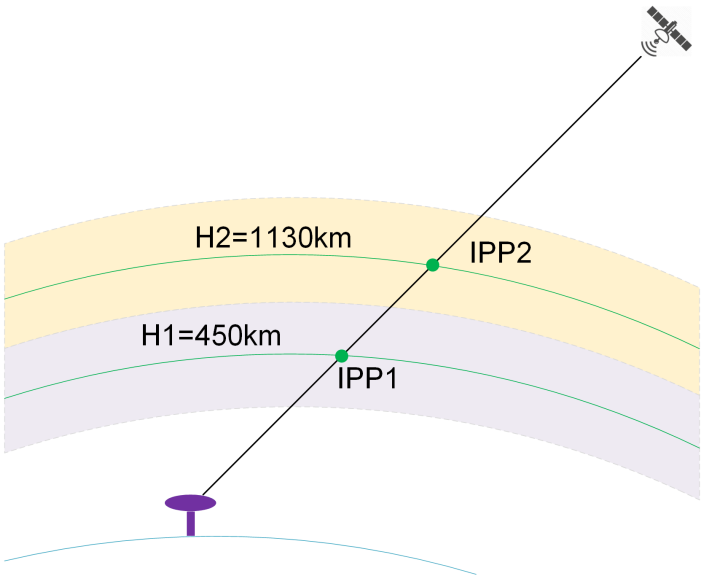

Figure 2.11 Diagram showing the two ionospheric pierce points involved in BIMF definition

dSTEC can be defined as the STEC value at a specific epoch minus the STEC at maximum elevation for the same continuous arc of each given GPS transmitter–receiver pair. It is typically computed every 30 seconds and can be written as $\Delta S = \Delta L_I/\alpha$ with $\alpha = 40.309(f_1^2 - f_2^2)/f_1^2 f_2^2 \simeq 0.105$ m/TECU for GPS (Hernández-Pajares et al., 2011). Such a ΔS value is very accurate, reflecting the level of the carrier phase measurement noise and multipath, i.e. it is typically much below 0.1 TECU. The corresponding ΔS error, ε, can be obtained in a straightforward way as $\varepsilon \simeq \Delta L_I/\alpha - \Delta(M \cdot V)$, where M represents the ionospheric mapping function adopted by the ionospheric model under assessment and V stands for VTEC. Pairs of observations that are separated in elevation by more than 20° are considered because they show significant STEC differences which are sensitive to the accuracy of the model. The comparison of the observed ΔS versus the modeled ΔS, in terms of Root Mean Square (RMS), is the so-called dSTEC test for any ionospheric model.

All in all, dSTEC can be considered as a good ionospheric reference truth for the assessment of any ionospheric mapping function.

To evaluate the performance of BIMF, we have considered:

(1) The dSTEC data for the year 2014 from all the available IGS stations, which are not used for the generation of the UQRG GIMs in the studied region. These independent receivers have been selected to ensure external electron content information, following the recommendations given in Hernández-Pajares et al. (2017c). Here, the latitude range of the selected stations is narrowed to 35°N to 55°N to assure the latitude of IPPs in the modeling region (30°N to 60°N). There are 14 stations available in the

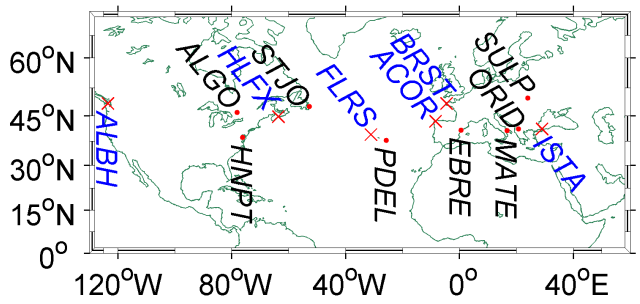

Figure 2.12 IGS stations that were not used for the generation of UQRG GIMs in 2014 but are used for external assessment of the BIMF performance. The stations in blue are not used for statistical purposes because of limited data due to only a few available days in which the stations are not used for GIM computation

specific range, but only 8 of them, marked in black in Figure 2.12, have enough data to compute statistics.

(2) Several statistical parameters to perform the comparisons. Namely:

(a) The daily RMS error of dSTEC, experienced by each GIM (hereinafter dRMSe), with BIMF versus the corresponding error using the classical mapping functions at 450 km (IGS) and 350 km (SBAS) effective heights.

(b) Percentage of days for which BIMF is performing better, i.e. having lower dSTEC daily RMS error (dRMSe) than the classical mapping functions (hereinafter $\%dB$). It is worth mentioning that the number of available days is less than 365, as shown in Tables 2.6, 2.7, and 2.8, because the days in which the selected station was used in the GIMs computation are not considered for a fair assessment.

(c) Relative error of dRMSe referred to the daily RMS of the observed dSTEC values, dRMS, hereinafter $\varepsilon_{rel}[\%] = 100 \cdot dRMSe/dRMS$.

(d) Difference of ε_{rel} for the classical mapping functions and ε_{rel} for BIMF, being positive when BIMF performs better, hereinafter $\Delta\varepsilon_{rel}[\%] = \varepsilon_{rel}[classic] - \varepsilon_{rel}[BIMF]$.

Considering different single-layer heights for different applications, typically 450 km for GIM and 350 km for SBAS, standard mapping functions with the single-layer height of both 450 and 350 km are compared with BIMF. For simplification, we use S450 and S350 to represent standard mapping functions with shell height 450 and 350 km, respectively, in this context.

By taking the dSTEC analysis for the station ORID for DOYs 16-30, 2014 as an example, Figure 2.13 clearly demonstrates that dRMSe values with BIMF are smaller than those

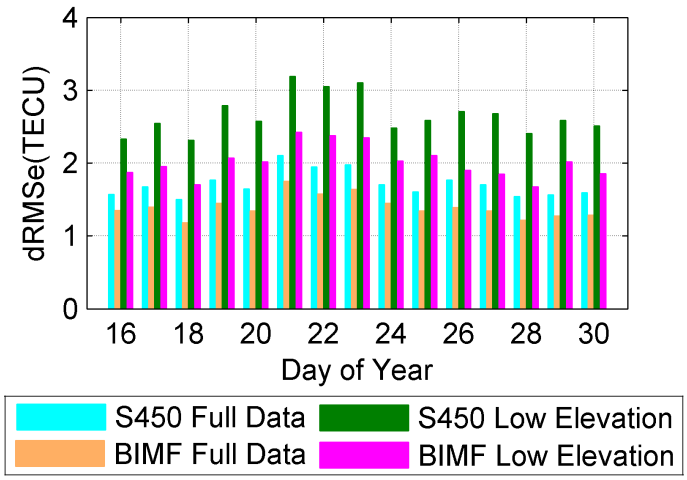

Figure 2.13 ORID station: dSTEC daily RMS error with BIMF and S450 for UQRG GIMs from DOY 16 to 30, 2014. The bars in cyan and in orange are the results for all data. The other two bars indicate the results of S450 (pink) and BIMF (green) for the elevation of the given line-of-sight ray being lower than 40°, and the difference with the reference ray above 20°

with the standard mapping function, particularly for the signals gathered at low elevations. Specifically, the dRMSe has been reduced by approximately 0.5 to nearly 1.0 TECU. The results of the 234-day analysis in 2014, shown in Figure 2.14, indicate that BIMF performs better than the standard mapping function in 210 days in terms of dRMSe, i.e. $\%dB$ more than 90%.

As for the eight IGS stations identified for computing statistics, BIMF applied to UQRG GIMs performs well for six stations, but not for stations ALGO and STJO, which are high-geomagnetic latitude stations (Table 2.6). The BIMF performance might be improved in the future when a global BIMF model based on solar-magnetic local time and latitude can be developed. The number of days where the dSTEC dRMSe are decreased accounts for more than 70% of available days in 2014. Moreover, when the GIMs of two additional IGS Ionosphere Associate Analysis Centers (IAAC), CODG and JPLG, are used for the assessment (Table 2.9 and 2.10), they show larger reductions of dSTEC error than UQRG GIMs: with $\Delta\varepsilon_{rel}$ up to 22% and 20% for 2014 for the respective IAAC GIMs, compared to the results with up to 8% of improvement in the case of UPC GIM. This is consistent with the fact that UQRG GIMs were already estimated with the dual-layer tomographic model, providing a more realistic representation of the slant electron content at different elevations. As shown in Table 2.8, the BIMF improved dSTEC using JPLG GIMs as well, with an improvement given by $\%dB$ in more than 70% of cases. From all the 14 available stations,

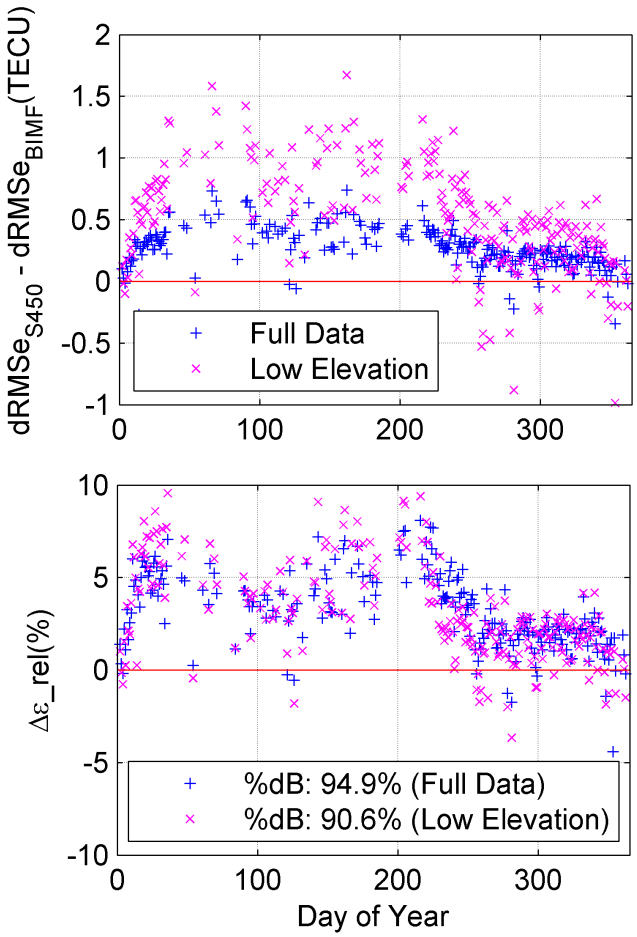

Figure 2.14 ORID station: the differences of dRMSe with S450 minus dRMSe with BIMF for 234 days during the year 2014, applied on the UQRG GIMs. The upper plot gives the absolute differences and the bottom plot gives the percentage of differences with respect to the dSTEC daily RMS

10 stations have a $\%dB$ over 90% for low-elevation statistics. This reinforces the physical consistency of BIMF, regardless of the UPC-TOMION model used originally to compute it.

Table 2.6 Statistics results of different stations using UQRG in 2014, focusing on the percentage when the daily RMS error of BIMF is lower than that of S450 ($\%dB$)

Site name	Geographic latitude	Geographic longitude	Geomagnetic latitude	$\%dB$		Number of days
				Full data	Low elevation	
ALGO	45.96°N	78.07°W	55.46°N	39.2	32.7	171
EBRE	40.82°N	0.49°E	42.79°N	72.9	69.1	188
HNPT	38.59°N	76.13°W	48.13°N	72.8	71.5	239
MATE	40.65°N	16.70°E	39.89°N	93.7	86.1	252
ORID	41.13°N	20.79°E	39.67°N	94.9	90.6	234
PDEL	37.75°N	25.66°W	43.84°N	86.7	88.0	241
STJO	47.60°N	52.68°W	56.44°N	24.3	42.8	173
SULP	49.84°N	24.01°E	47.61°N	78.3	74.8	115

Table 2.7 Statistical results for different stations using CODG in 2014

Site name	Geomagnetic latitude	$\%dB$		Number of days
		Full data	Low elevation	
ACOR	46.73°N	56.4	48.5	202
ISTA	38.30°N	84.1	80.4	244
ORID	39.67°N	66.5	63.1	236
SULP	47.61°N	48.3	50.0	118

2.6 Summary

A simple way of improving GNSS slant ionospheric correction from VTEC models is presented. In many GNSS applications, a mapping function is required to convert from VTEC, which may be provided in GIMs, to STEC. Typical approaches assume a single ionospheric shell with constant height, which is unrealistic, especially for low-elevation signals. To reduce the associated conversion error, we propose the Barcelona Ionospheric Mapping Function and its first implementation at northern mid-latitudes (BIMF-nml). BIMF is based on a climatic prediction of the distribution of the topside vertical electron content

fraction of VTEC - μ_2. BIMF is convenient to be applied since no external data are required in practice. To evaluate its performance, we use as independent reference the STEC difference (so-called dSTEC) values directly measured from mid-latitude dual-frequency GPS receivers that have not been used in the computation of the VTEC GIMs under assessment. It is shown that the use of BIMF improves the GIM STEC estimation compared to the single-layer assumptions. This is the case for the mapping functions used by IGS and SBAS. This improvement is valid not only for the UPC GIMs, up to 15% for the year 2014, but especially for the GIMs of other analysis centers, such as those produced by CODE and JPL, up to 32 and 29%, respectively.

Table 2.8 Statistical results for different stations using JPLG in 2014

Site name	$\%dB$		Number of days
	Full data	Low elevation	
ACOR	78.7	71.3	202
ALBH	98.4	99.2	248
ALGO	89.6	91.2	251
EBRE	79.5	87.0	239
FLRS	89.1	94.8	248
HLFX	90.1	94.4	252
HNPT	96.3	98.3	240
ISTA	98.4	98.4	245
MATE	91.7	96.8	252
ORID	96.2	97.0	236
PDEL	81.0	95.2	248
STJO	84.0	88.0	250
SULP	96.6	95.8	118

Table 2.9 BIMF compared to Standard Mapping Function with fixed height at 450 and 350 km for different GIM products in 2014 (see Roma-Dollase et al. (2018) for details on GIMs): $\%dB$ (percentage of days with lower dRMSe, see above) for all stations. For UQRG GIMs, stations ALGO and STJO are excluded

GIMs	$\%dB$			
	Full data		Low elevation	
	450 km	350 km	450 km	350 km
UQRG	[72.8, 94.9]	[90.4, 98.8]	[69.1, 90.6]	[87.8, 98.7]
CODG	[48.3, 84.1]	[71.8, 95.9]	[48.5, 80.4]	[70.8, 95.9]
JPLG	[78.7, 98.4]	[90.6, 100]	[71.3, 99.2]	[88.1, 100]

Table 2.10 BIMF compared to Standard Mapping Function with fixed height at 450 and 350 km for different GIM products in 2014 for details on GIMs): maximum $\Delta\varepsilon_{rel}$ (relative error reduction with BIMF) for all stations. For UQRG GIMs, stations ALGO and STJO are excluded

GIMs	Maximum $\Delta\varepsilon_{rel}$			
	Full data		Low elevation	
	450 km	350 km	450 km	350 km
UQRG	[4.4, 8.1]	[8.8, 14.7]	[5.9, 10.6]	[11.6, 18.4]
CODG	[4.1, 22.1]	[7.9, 32.0]	[5.5, 13.7]	[8.9, 22.7]
JPLG	[5.0, 20.8]	[9.3, 28.7]	[5.9, 18.0]	[11.6, 25.9]

Chapter 3

Study of the electron content distribution in polar regions from UQRG

3.1 Introduction

The ionosphere at high latitudes is considerably complex due to the fact that nearly vertical magnetic field-lines connect the high latitudes to the outer part of the magnetosphere which is driven by the solar wind. Plasma density irregularity at high latitudes, associated with intense levels of scintillation, can severely disrupt High Frequency (HF) radio communication, surveillance and satellite navigation systems. With the increase of human activities relying on such systems, the ionospheric features in the polar regions are of increasing interest. Thus it is essential to understand the morphology and climatology of different features, such as Tongue of Ionization (TOI), polar cap patches, troughs etc. Over the past decades, knowledge has advanced significantly regarding those ionospheric features in polar regions, based on the observation from various instruments, including incoherent scatter radars, HF radars, digisondes, all-sky intensified photometers, scintillation receivers, and ion drift meter sensors on board satellites, as well as theoretical and assimilation models (Basu et al., 1990, 1985; Buchau et al., 1983; Bust and Crowley, 2007; Coley and Heelis, 1995; Foster and Doupnik, 1984; Kelly and Vickrey, 1984; Rodger et al., 1994; Sojka et al., 1994; Weber et al., 1984, 1986). All have contributed to build a more comprehensive morphological description of polar ionosphere. However, the information and speculation of some mechanisms mostly came from case studies. Considering continuous, global coverage and low-cost characteristics of IGS GNSS data, it is, therefore, worth exploiting the potential of GIMs derived from such GNSS data to detect important polar ionospheric features, study their climatology and thereby improve our knowledge of polar ionosphere.

TOI and segmented polar cap patches are taken as an example to further elucidate the necessity of exploring the value of long-term GIMs derived from IGS GNSS network data in the study of polar ionosphere. Since 1980s, different congestions on the plasma source and mechanism of TOI and patch formation have been put forward based on diverse instrument observations, including data from optical, HF and incoherent radar, ionosondes and satellites (Kelley et al., 1982; Rodger et al., 1994; Weber et al., 1984). Due to the complexity of polar ionospheric activity, there are many mechanisms through which patches can be formed under different Interplanetary Magnetic Field (IMF) and ionospheric conditions, on which (Carlson, 2012) has made an exhaustive review. Among them, one mechanism is enhanced dayside plasma produced by solar photoionization convects across the cusp and into the dark side of the polar cap (Sojka et al., 1994). Another theory is that transient bursts of magnetopause reconnection, i.e. flux transfer events, cause discrete patches of enhanced plasma density (Balmforth et al., 1999; Lockwood and Carlson Jr, 1992; Zhang et al., 2013). In addition, particle precipitation is thought to produce low-density patches (Carlson, 2012). Nevertheless, there is still lack of satisfactory explanation of how polar cap patches are formed and it is challenging to have a whole view of TOI and patch generation based on limited historic data or theoretical models, from which different dependence characteristics on polar cap patches were obtained (Table 3.1). Although the source and mechanism of TOI and patches creation are beyond the scope of the discussion in this Ph.D. dissertation, new findings with more available data today, which gives more comprehensive understanding of polar cap patches, can be the evidence to support some theories, as well as to point out the incompleteness of some speculations, or even to exclude some assumptions. For instance, using high-resolution TEC Maps from the Madrigal Database of Haystack Observatory, David et al. (2016) found that north-hemisphere TOI or patches have Universal Time (UT) and seasonal dependence, contradicting some theories on patch source, which are particle precipitation, motion of the cusp, electric field variations and flux transfer events. This implies those theories cannot be regarded as the dominant mechanism. Moreover, their finding on occurrence frequency shows inconsistency in the assumption that the formation of TOI and patches depends on the level of geomagnetic activity. Whether polar patches are a seasonal or annual phenomenon, however, is called into question by the finds of Chartier et al. (2018). They used in-situ plasma density observations and topside TEC data to detect TOI and found that TOI is not only a winter phenomenon, but also occurs in Southern Hemisphere summer (more patches around December in both hemispheres), which is significant to modify existing theories. In short, due to the limited time span and limited spatial coverage of the observation, it is difficult to accurately obtain the climatology and further give the theoretical mechanism.

As has been mentioned above, high-resolution VTEC maps have been successfully used to detect TOI and polar cap patches in the Northern Hemisphere (David et al., 2016). In this chapter, relatively low-resolution global VTEC maps, UQRG, for the first time are used for the climatology study of selected polar ionospheric phenomena. Through these six case studies, including TOI, trough, flux transfer event, theta-aurora, ionospheric convection patterns and storm enhanced density, the capability of GIMs in detecting polar ionospheric features has been confirmed by comparison with the results reported by other authors with different and higher resolution techniques. Other than 2D VTEC distribution, the μ_2 distribution from UQRG also provides important information in vertical direction. After the usage of UQRG GIMs being justified, the comprehensive results of unsupervised clustering of polar VTEC maps are presented, showing the most frequent electron content patterns, and the key occurrence characteristics, in both the north and south polar hemispheres including polar caps (hereinafter NP and SP).

3.2 UQRG performance in polar regions

The work by Roma-Dollase et al. (2018) shows that the UQRG GIM behaves better than other GIMs at global scale, but no specific comparison has been made restricted to the polar regions. It can be seen in Figure 3.1 and 3.2 the distribution of daily standard deviations of the difference between the reference direct VTEC altimeter measurements (TOPEX, JASON-1 and JASON-2) and the corresponding interpolated GIM VTEC values, from 2002 to 2018, for north and south polar regions (north of 50°N and south of 50°S, respectively). Table 3.2 shows that UQRG has a performance slightly better than that of the final GIMs of the IGS analysis centers and their combination, in both NP and SP, in terms of average of the daily standard deviation of the altimeter and GIM VTEC difference: the first and second better behaving GIMs emphasized in bold and underline in Table 3.2, respectively, for both distribution mode and average. And this is mostly due to the technique being used, rather than the higher temporal resolution of UQRG (15 minutes) compared with the final GIMs (2 hours), as it was demonstrated in section 3.1 of Roma-Dollase et al. (2018). Hence we conclude that the UQRG GIM time series is an appropriate candidate to attempt to detect significant polar TEC features and to extract the polar electron content climatology, as indicated in Section 3.3 and Section 3.4.

Table 3.1 Studies on occurrence dependence of TOI and polar patches.

Measurement / model source	Area	Dependence				Ref.
		Annual/ Seasonal	UT/ MLT(LT)	Geomag./ IMF	Solar Cycle	
Digisonde	NH	x	UT	x	Solar Cycle	Buchau et al. (1985)
The Utah State University time dependent ionospheric model (TDIM) [a]	NH	Seasonal	UT	x	x	Sojka et al. (1994)
The retarding potential analyzer(RPA), the ion drift meter(IDM), and the Langmuir probe aboard the DE 2 spacecraft	NH	Seasonal	UT	IMF	x	Coley and Heelis (1998)
foF2 data from Digital Ionospheric Sounding Systems at stations Sondrestromfjord and Qaanaaq	NH	Seasonal	MLT	IMF(weak)	Solar Cycle	Dandekar (2002)
9-years CHAMP TEC data	NH, SH	Annual	MLT	IMF	Solar Cycle	Noja et al. (2013)
Madrigal GPS TEC Maps (high-resolution)	NH	Seasonal	UT	x	x	David et al. (2016)
The National Center for Atmospheric Research Thermosphere-Ionosphere Electrodynamics General Circulation Model (TIEGCM)	NH, SH hemispheric asymmetry of TOI intensity	Seasonal dependence of UT effects on TOI intensity	UT	IMF	x	Liu et al. (2017)
Swarm: in situ plasma density measurements	NH, SH	Seasonal	x	IMF	x	Spicher et al. (2017)
Swarm: in situ electron dens. by Langmuir probe and TEC from POD GPS receiver	NH, SH	Annual	x	Kp-independent	x	Chartier et al. (2018)

[a] Switch between the A and DE patterns every 30 min with constant inputs: (a) The auroral oval parameters, specifically the electron energy flux and average energy, were obtained from Hardy et al. (1987) model. (b) A solar maximum condition was assumed, represented by an F10.7 index of 210.

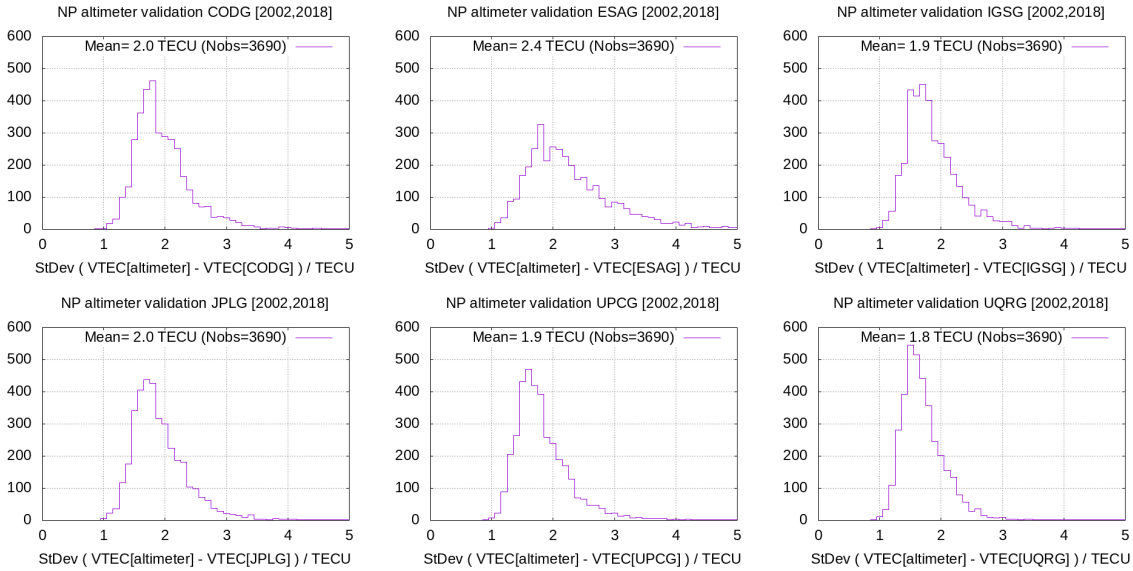

Figure 3.1 Distribution of the daily standard deviation values between the GIM VTEC and the 9,647,398 direct VTEC measurements available from TOPEX, JASON-1 and JASON-2 altimeters, around the north pole (north of 50°N) between day 7 of year 2002 and day 360 of year 2018. They correspond, from left to right and from top to bottom, to the CODG, ESAG, IGSG, JPLG, UPCG and UQRG GIMs.

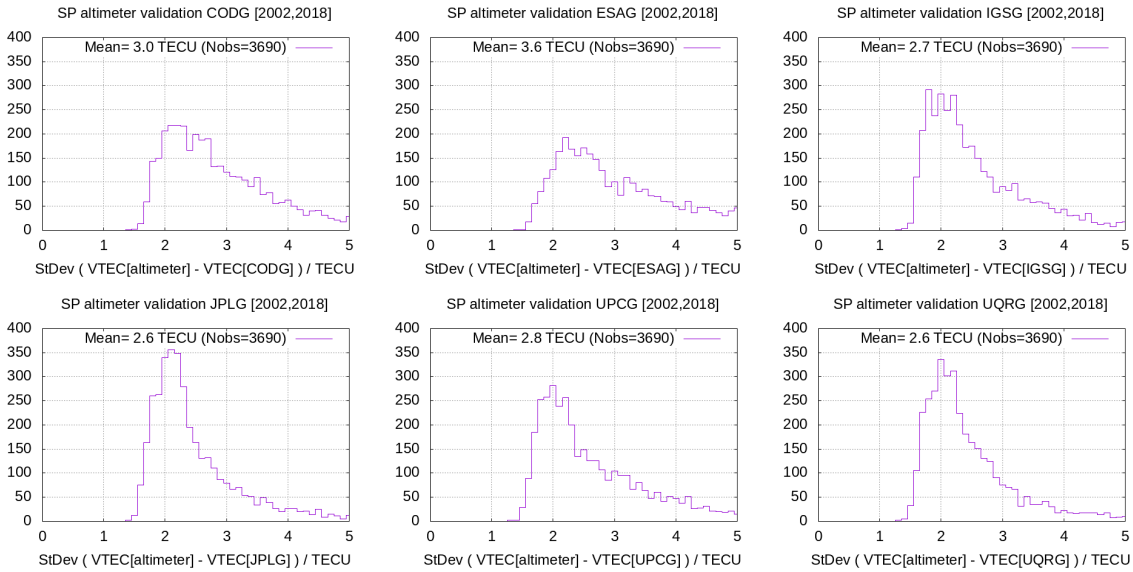

Figure 3.2 Distribution of the daily standard deviation values between the GIM VTEC and the 33,115,960 direct VTEC measurements available from TOPEX, JASON-1 and JASON-2 altimeters, around the south pole (south of 50°S) between day 7 of year 2002 and day 360 of year 2018. They correspond, from left to right and from top to bottom, to the CODG, ESAG, IGSG, JPLG, UPCG and UQRG GIMs.

Table 3.2 Summary of daily standard deviations of GIMs vs. direct altimeter VTEC measurements, in TECUs, in NP (north of 50°N) and SP (south of 50°S), and from 2002 to 2018. It summarizes the detailed results described in Figure 3.1 and 3.2.

Daily Std.Dev. vs. Altimeter VTEC				
GIM	NP		SP	
Id.	Mode	Average	Mode	Average
CODG	1.8	2.0	2.2	3.0
ESAG	1.8	2.4	2.2	3.6
IGSG	**1.5**	**1.8**	**1.8**	2.7
JPLG	1.7	2.0	2.1	**2.6**
UPCG	1.6	1.9	2.0	2.8
UQRG	**1.5**	**1.8**	2.0	**2.6**

3.3 Polar features in UQRG GIM

In this section, the capability of UQRG GIM to realistically detect different polar content features is confirmed. This is demonstrated through some representative case studies previously reported by other authors with different and higher resolution techniques: tongue of ionization, ionospheric trough, flux transfer event, theta-aurora, ionospheric convection patterns and storm enhanced density.

3.3.1 Tongue of Ionization

The TOI and associated patches are special features of the polar ionosphere, which are believed as plasma enhancements in the high latitude F region.

The UQRG GIM VTEC map at 1700 UT on 5 November 2012, when the NP TOI was reported in David et al. (2016), is shown at the left-hand plot of Figure 3.3. This is fully consistent in extension, shape and VTEC level (up to around 20 TECU in the TOI) with Figure 2 of David et al. (2016), obtained with a higher resolution VTEC mapping technique. In addition, a simultaneous TOI happened in the SP, which can be seen at the right-hand plot of Figure 3.3.

Another interesting feature about TOIs in the SP is that most of the TOIs cross or direct to the south magnetic pole (see four examples at different UT times in Figure 3.4), which is located in the range $(136-138°\text{E}, 63-64°\text{S})$ from 1998 to 2015. The frequent appearance of this feature shows the TOI bends from its origin at the daylight hemisphere side towards the magnetic pole. It is noticeable that the μ_2 values within the TOIs are typically smaller than

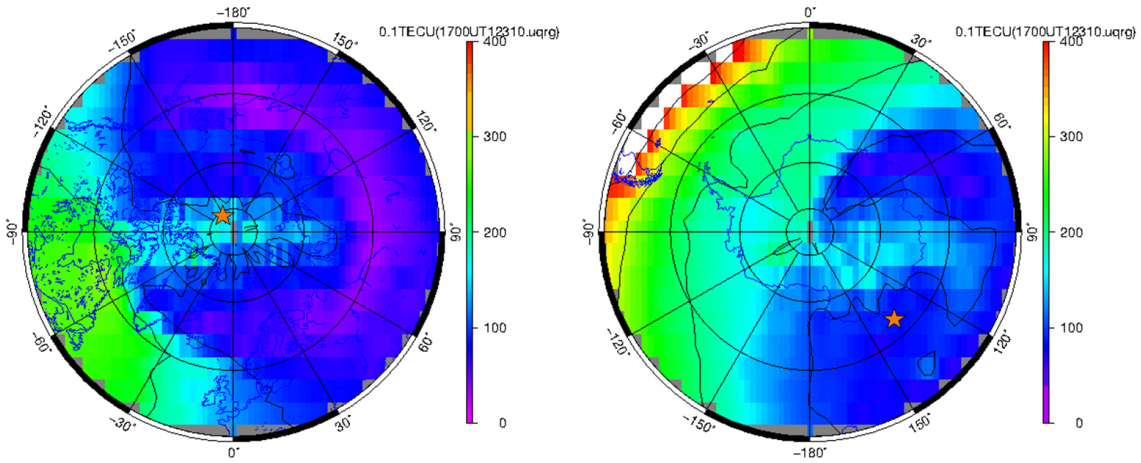

Figure 3.3 VTEC maps in NP (left) and SP (right) at 1700 UT on 5 November 2012. The VTEC scale is given in 0.1 TECUs, the same as the remaining VTEC GIMs in this section. The red star represents the corresponding magnetic pole.

those in the surrounding night polar ionosphere, e.g. the case at 1745 UT of DOY 079, 2001 in Figure 3.4, showing μ_2 in the TOI around [0.3, 0.8] compared to the range approximately between 1.0 and 1.5 in the rest of nightside ionosphere. The smaller μ_2 values represent the associated electron content being distributed significantly lower in height. While, when TOI and the daylight areas are compared, the μ_2 values change slightly. It indicates that the ionospheric effective height, where the free electron can be considered concentrated in a simplified view, almost keeps constant in the TOI from the day-side part. This agrees with the result obtained from Digisonde that the virtual heights in the ionograms did not change during transit of the arcs through the zenith (Buchau et al., 1983).

3.3.2 Trough and Dawnside Drifting Structure

An ionospheric trough is a region of depleted ionization, limited in width but extended in the east-west direction, with more intense regions to the north and south (Hunsucker and Hargreaves, 2007). Taking 1745 UT on DOY 041, 2003 (Figure 3.5) as an example, from the left panel, it is easy to see the mid-latitude trough (in purple), also called as the main ionospheric trough, in the nightside sector. And the right panel shows that μ_2 values in the trough are above 0.8 (corresponding to the represented values of $\mu^\star = \mu_2 + 1 > 1.8$), greater than those in the surrounding area. Big μ_2 implying high ionospheric effective height, corresponds to decrease in concentration of O+ and a typical mid-latitude trough feature - enhanced electron temperature. According to the proportional relationship between temperature and scale height, the high temperature would increase the scale height in the

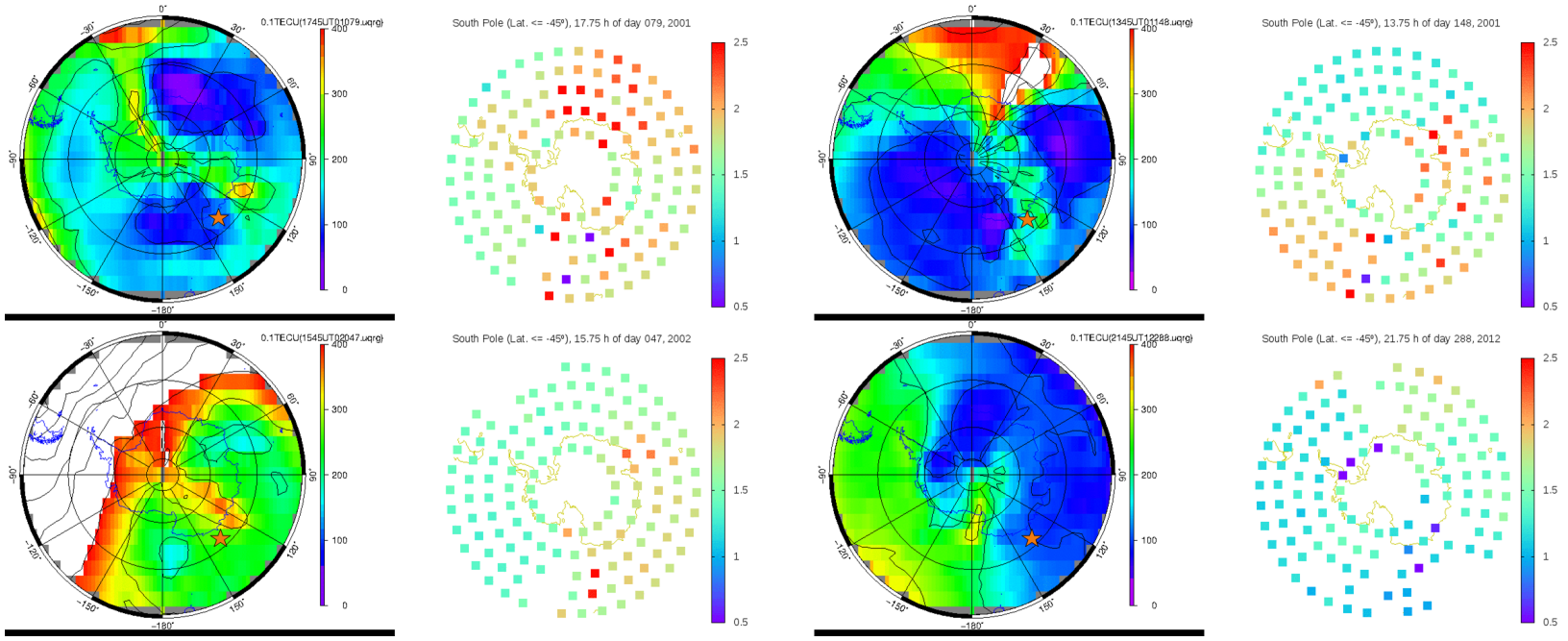

Figure 3.4 Four typical SP VTEC maps showing TOIs, and the associated μ_2 distribution, corresponding to the year-DOY-UT: 2001-079-1745, 2001-148-1345, 2002-047-1545 and 2012-288-2145 (from left to right, from top to bottom). The white area in all the VTEC maps of this context represents VTEC values greater than 40 TECU. In the right panel of each subplot, the values in colorbar are $\mu_2^\star = \mu_2 + 1$. The red star represents the corresponding magnetic pole.

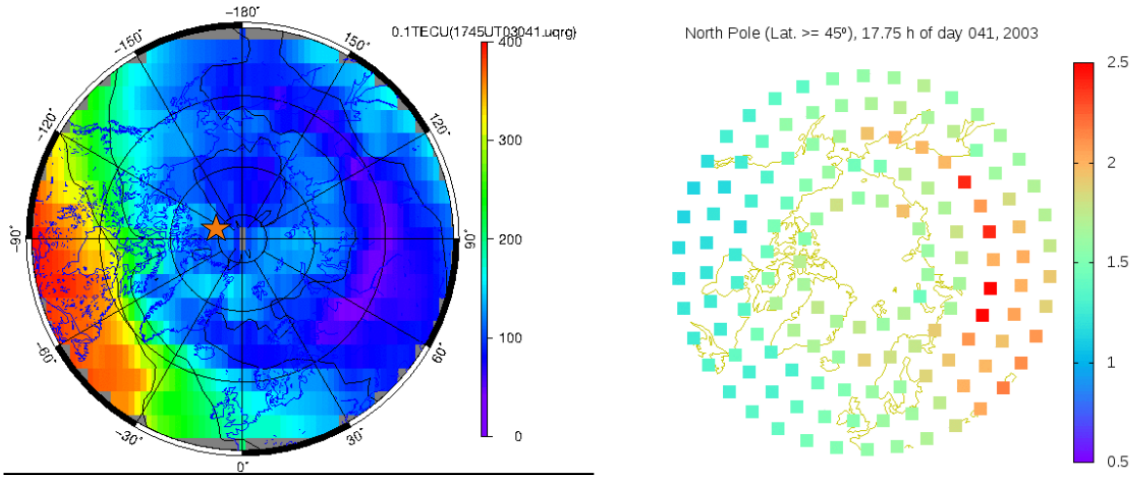

Figure 3.5 VTEC and μ_2 NP maps at 1745 UT on DOY 041, 2003 from UQRG GIMs. In the right panel, the values in colorbar are $\mu_2^\star = \mu_2 + 1$. The red star represents the corresponding magnetic pole.

topside part, resulting in slow decay of electron density above the peak, thus increasing the ionospheric effective height. Apart from the trough, the ring-like enhanced ionization area is clear in VTEC map of Figure 3.5, which will be confirmed in the polar climatology summarized in Section 3.4 (see for instance third and second column of Figure 3.16). In this case study, at 1745 UT, the IMF y-component, B_y, is negative and the z-component, B_z, is switching from northward to southward (see Figure 3.6). The convection theory (Sojka et al., 1993) suggests that, for negative B_y when IMF is southward, the flow is across the dusk-side of the polar cap. While the structure in the VTEC map appears to be dawn-side, thus the convection pattern needs to be further investigated by theoretical model.

3.3.3 Flux transfer event

On 13 February 2001, the transpolar propagation of large-scale TIDs from the nightside source region to the dayside was reported by Cai et al. (2011). On 14 February, the magnetospheric flux transfer events (FTE) are observed by Cluster spacecraft (Wild et al., 2001, 2003). As demonstrated in Table 3.2, UQRG can provide good VTEC estimation with the Kriging interpolation technique, in spite of the limited number of permanent receivers during these early times especially in SP. The VTEC maps in both hemispheres (see Figure 3.7 and 3.8) show the ionospheric response to these events. NP VTEC Maps from 11 February (DOY 041) to 17 February (DOY 047) 2001 have been closely examined. It is worth mentioning that only a series of VTEC maps from 1900 UT of DOY 044 to 0500 UT of DOY 045 with 2-hour interval has been shown in figures to avoid excessive length (Two

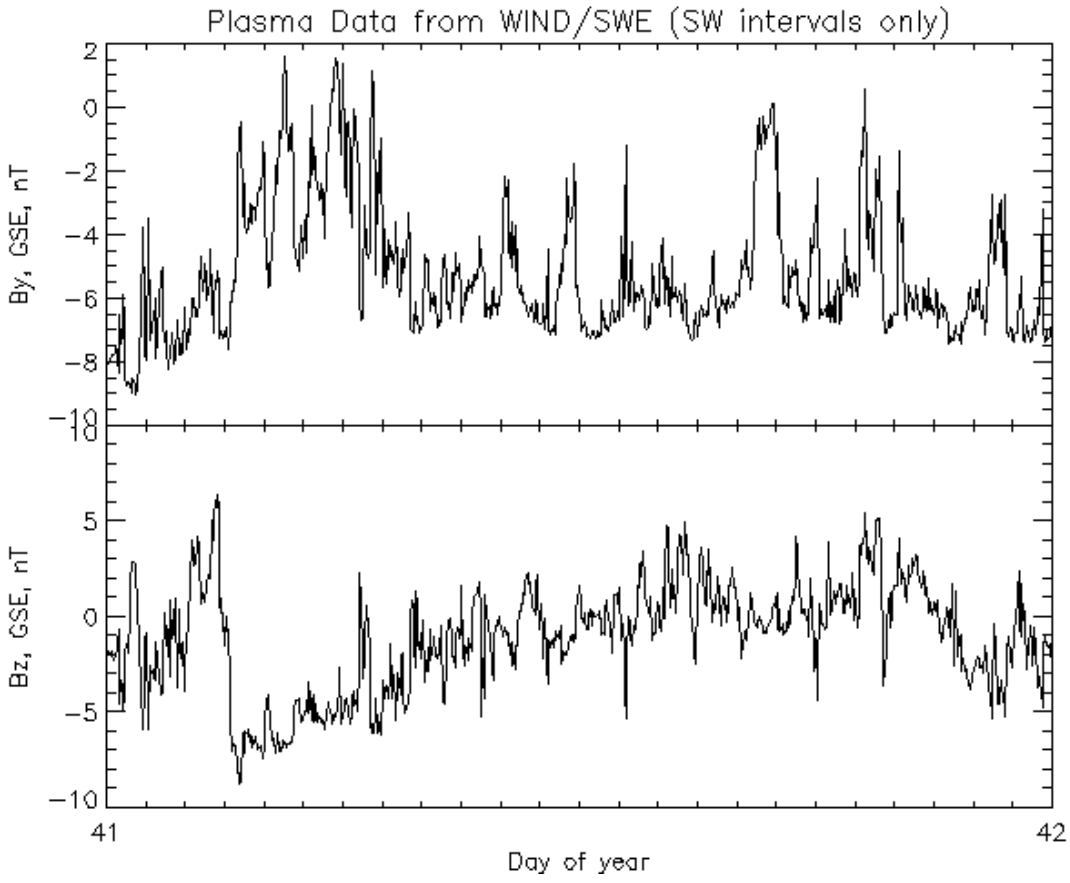

Figure 3.6 IMF B_y and B_z components on DOY 041, 2003, downloaded from https://omniweb.gsfc.nasa.gov/ftpbrowser/wind_swe_2m.html

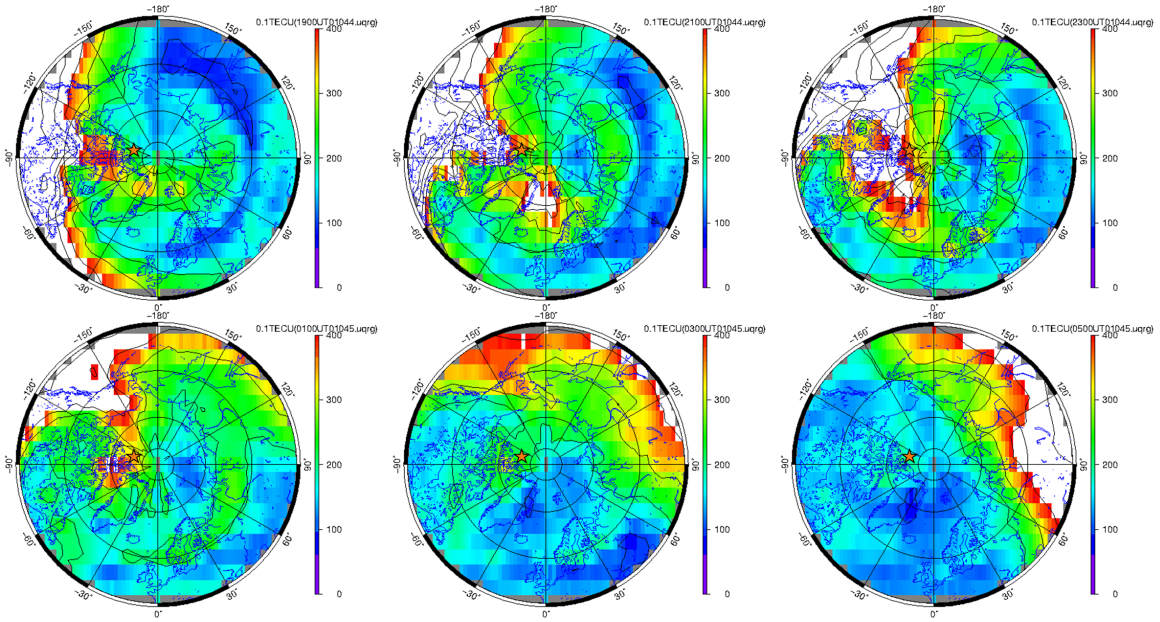

Figure 3.7 From left to right and from top to bottom: NP VTEC maps from UQRG GIMs, showing the development of TOI and patches each 2 hours from 13 February 1900 UT to 14 February 0500 UT, 2001. The red star represents the corresponding magnetic pole.

animations of all the UQRG GIMs from DOY 041 to 047 for both NP and SP are available in ftp://chapman.upc.es/.polar_VTEC_movies.from_UQRG_GIMs). TOI occurred and lasted for around 4 and 5 hours after 1500 UT for DOY 041 and 042 respectively. From 2330 UT of DOY 043 to 0100 UT of DOY 044, two-TOI-like structure presented, which is similar to that in the bottom-left plot of Figure 3.7. Afterwards, between 1700 UT of DOY 044 and 0200 UT of DOY 045, very strong TOI appeared, then drifting to the duskside and back to the dawnside later, and gradually forming a loop and then separating into two-TOI-like structure again. During the second half day of DOY 045, TOI was formed from 1315 UT to 1730 UT. Whereas, on both DOY 046 and 047, no obvious TOI showed up. From SP VTEC maps, TOI appeared in two time slots [0600 UT, 0730 UT] and [2145 UT, 2330 UT] on DOY 044, 2001, three days before which no TOI showed up. What is interesting is a swan-shape structure, which is drifted TOI, occurred around 0200 UT on DOY 045, 2001. And on the same day, TOI can also be seen from 1130 UT to 1500 UT. The specific NP feature that two-TOI-like structure appeared and merged later on might be related to FTE or directly to the geomagnetic disturbance caused by FTE. The mechanism is still unknown and it is worth investigating with other measurements.

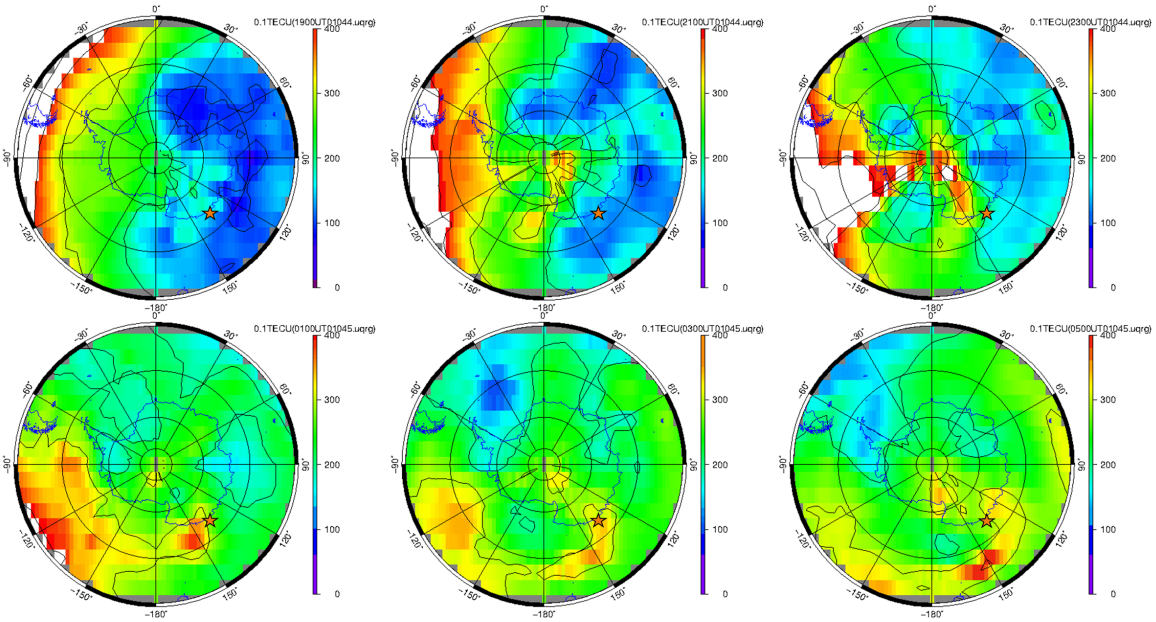

Figure 3.8 From left to right and from top to bottom: SP VTEC maps from UQRG GIMs, showing the development of TOI and patches each 2 hours from 13 February 1900 UT to 14 February 0500 UT, 2001. The red star represents the corresponding magnetic pole.

3.3.4 Theta-Aurora VTEC Observation in SP

During 1638-2000 UT of September 15, day 258 of year 2005, direct observations of closed magnetic flux, in correspondence with a small and thin transpolar arc over SP, were taken by the FUV Wideband Imaging Camera of the IMAGE satellite (see Figure 4A in Fear et al. (2014)). We have detected the formation of a transpolar arc, longer and thicker, during this day, before the pass of the satellite. It can be seen at the bottom of Figure 3.9, in the SP VTEC snapshots at 1115 UT and 1515 UT, with two associated depletions at both sides. Moreover, a ring of enhanced electron content was very clearly formed at 1515 UT (see the bottom-right plot in Figure 3.9). During the IMAGE satellite pass at 1915 UT this VTEC feature obtained from UQRG GIM was weaker, but still present and consistent as it is shown in Figure 3.10. It was located around the south magnetic pole, about (138°E,64°S) at such a time, with a radius of 15° approximately, in concordance with the above-mentioned figure of Fear et al. (2014). The ring together with a mid transpolar arc can be considered as part of such "theta-aurora" happened during northward IMF as explained in the same reference.

3.3.5 GIM Footprint of Ionospheric Convection Patterns

In Figure 3.11 we can see how clearly a typical two-cell convection pattern of VTEC is captured by UQRG GIM. This result is fully consistent with the convection patterns found

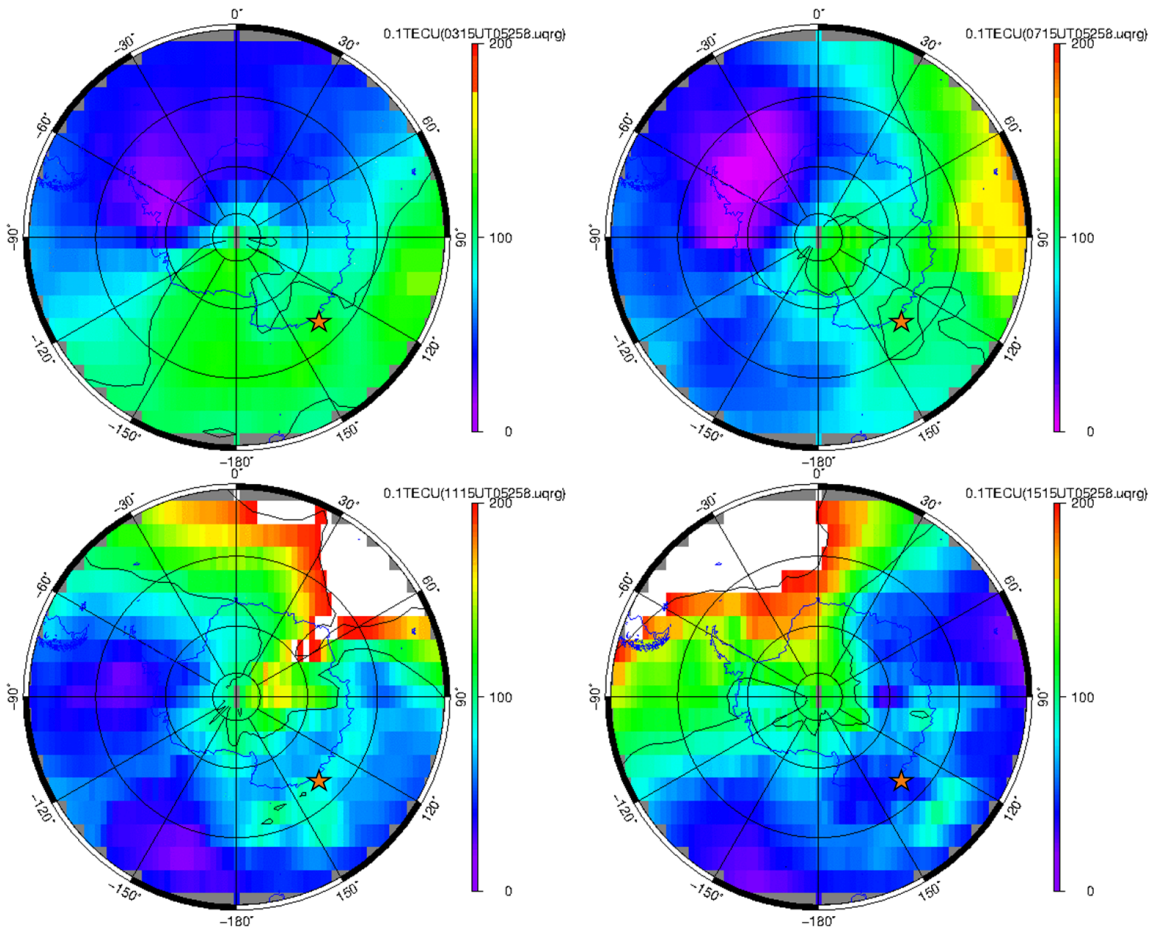

Figure 3.9 SP VTEC during 15 September, day 258, of year 2005 at 0315 UT, 0715 UT (the first row), 1115 UT and 1515 UT (the second row), extracted from UQRG GIM. The red star represents the corresponding magnetic pole.

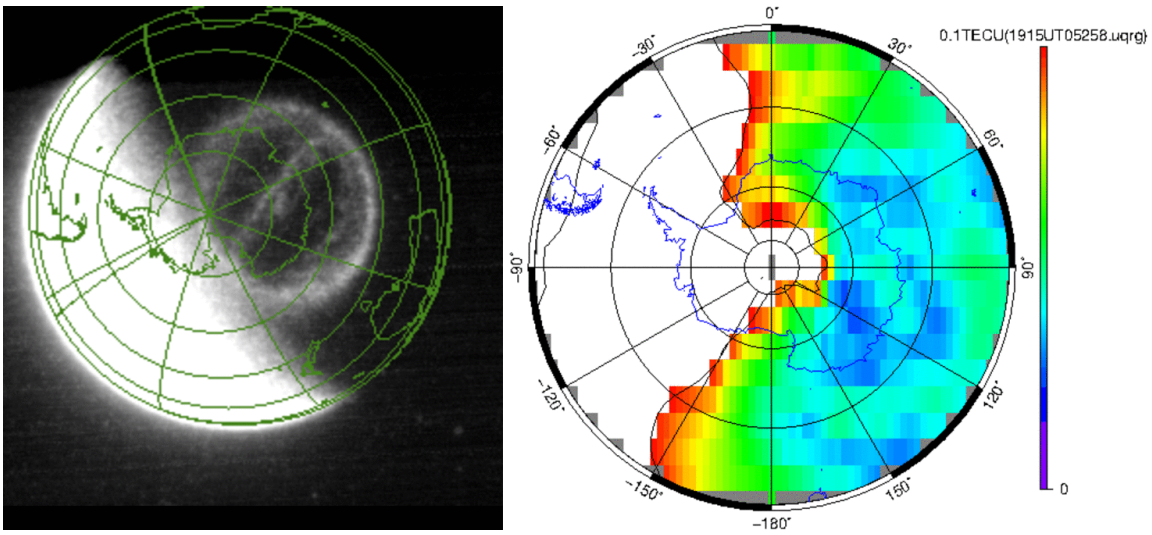

Figure 3.10 Collocated electron content distributions, obtained during September 15, 2005, 1915 UT approximately, in FUV by NASA's IMAGE satellite (provided at ht-tps://www.esa.int/ESA_Multimedia/Images/2014/12/Theta_aurora_as_seen_by_NASA_s_Image_satellite_on_1 the left-hand plot) and by UQRG GIM based on GPS ground-based measurements (the right-hand plot, with colorbar ranging from 0 to 10 TECU). Both depletion and the central transpolar arc can be seen in compatible positions, taken into account that the right-hand plot is oriented approximately 30 degrees clockwise relative to the left-hand plot.

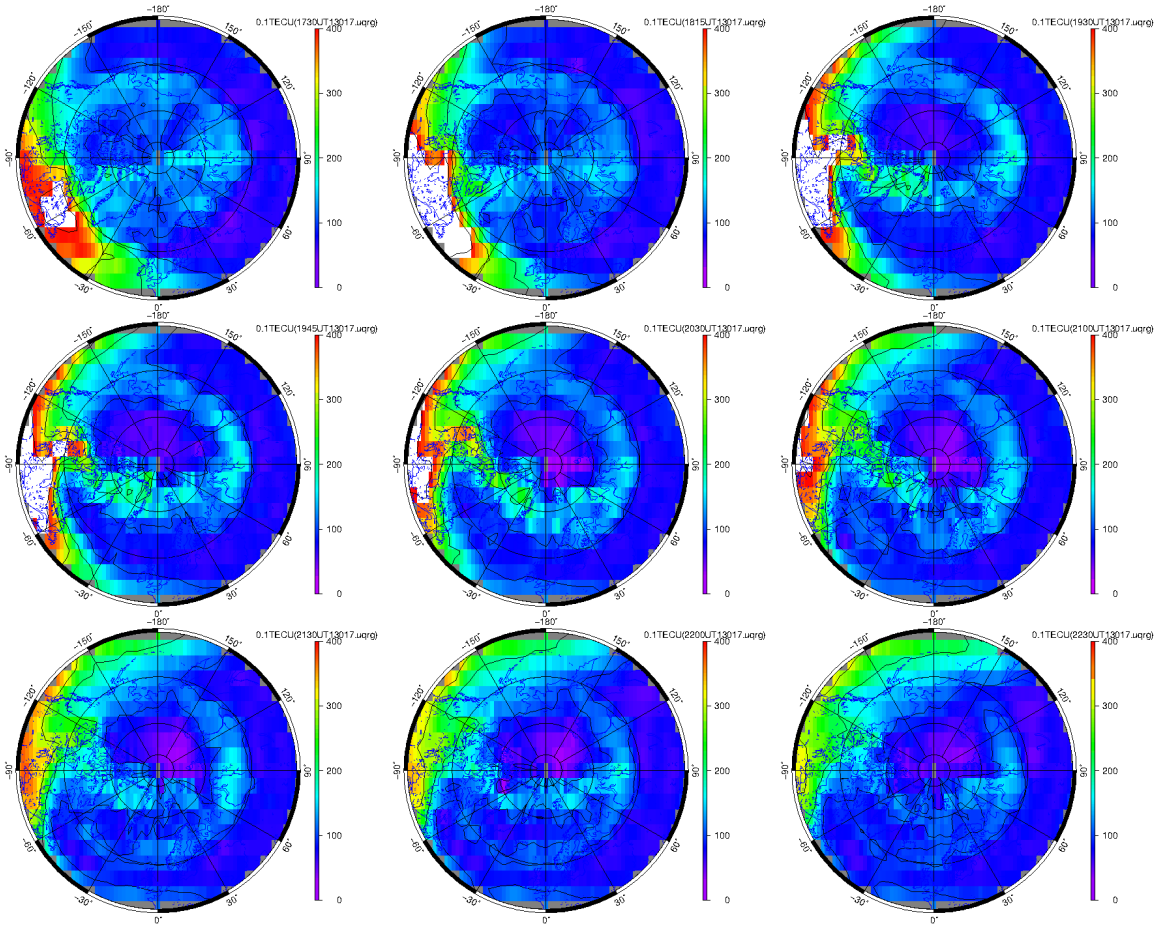

Figure 3.11 UQRG GIM VTEC in NP during 17 January 2013, during approximately the same times as those in Figure 2 in Zhang et al. (2015), in this case (from left to right, and from top to bottom): 1730 UT, 1815 UT, 1930 UT, 1945 UT, 2030 UT, 2100 UT, 2130 UT, 2200 UT and 2230 UT.

by means of the large-scale coverage of the flows provided by the Super Dual Auroral Radar Network (SuperDARN) radars, and with the GPS-based VTEC patches reported in NP and approximately at the same times in Figure 2 of Zhang et al. (2015). Although this event happened during southward IMF, i.e. during its reconnection with the geomagnetic field (see in Zhang et al. (2015) additional details, including the full Dungey convection cycle context), the fact that the corresponding representative normalized VTEC map shows a similar feature (see Figure 3.17, the fifth row and third column plot corresponding to NP at 2145UT), would suggest the possibility that this two-cell convection pattern might happen under different conditions too, even though its occurrence (see the first row and third column plot in Figure 3.18) is lower under the condition of Figure 3.11 when closing to solar cycle maximum.

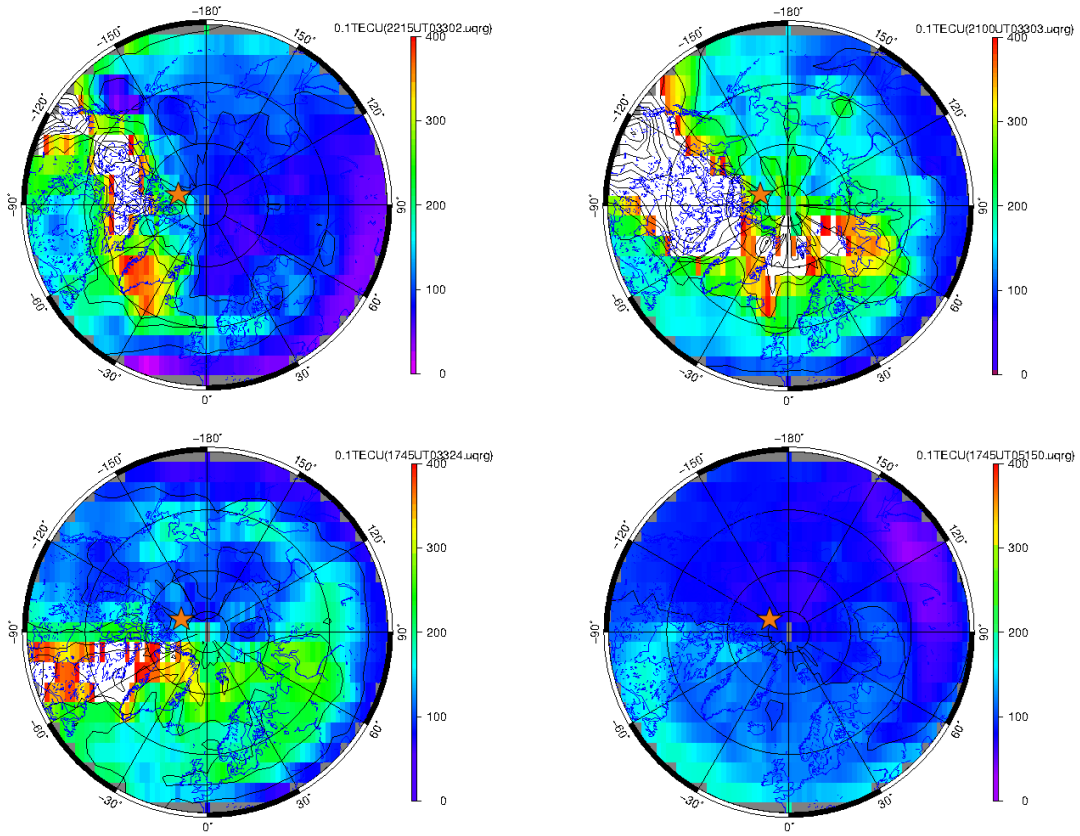

Figure 3.12 Four NP cases for storm enhanced TEC on two days (DOY 302 2215 UT and 303 2100 UT, 2003) of "Halloween Storms" (top), on DOY 324 1745 UT, 2003 (bottom-left), and DOY 150 1745 UT, 2005 (bottom-right), directly obtained from the corresponding UQRG GIMs. The red star represents the corresponding magnetic pole.

3.3.6 Storm-enhanced density

During geomagnetic storms, F-region ionospheric plasma from lower latitudes in the afternoon sector is transported polewards. Consequently, a latitudinally narrow region of Storm Enhanced Density (SED) and increased TEC is carried toward higher latitudes in the noon sector (Foster, 1993). The distribution of NP VTEC during major geomagnetic storms, including Halloween Storms of 2003 and the other two cases with Kp index around 7 and 8.7 respectively, is shown in Figure 3.12. The feature that the enhanced TEC plumes are concentrated in the pre-midnight and postnoon sector (Foster et al., 2005) can be seen in these four examples on Halloween Storms of 2003, DOY 324, 2003, and DOY 150, 2005.

3.4 Climatology of the Polar Ionospheres

3.4.1 Unsupervised Clustering Algorithm – Learning Vector Quantization

In order to better perform a first systematic analysis of the polar VTEC climatology from the large UQRG GIMs database, we have selected an unsupervised clustering system that enables to find representative prototypes of the VTEC maps directly extracted from the GIMs. This will also allow to characterize the occurrence of its predominant morphology and features. To carry out this analysis we have chosen the Learning Vector Quantization (LVQ) algorithm, (Kohonen, 2012; Murtagh and Hernández-Pajares, 1995). The reason for selecting the LVQ algorithm instead of other clustering algorithms, such as k-means or LBG (Linde et al., 1980), lies in the fact that it is an adaptive algorithm and does not require any a-priori categorization which might bias the analysis, as it was shown for instance in classification of astronomical populations (Hernández-Pajares, 1993) or in GNSS ionospheric determination (Hernández-Pajares et al., 1997).

As it was detailed in Hernandez-Pajares and Floris (1994), the aim of this unsupervised classifier is to find a smaller set of $C = \{\mathbf{c}_1, \ldots, \mathbf{c}_p\}$ of p centroids that provides a good approximation of the original set S of n ionization-level-independent, i.e. normalized polar VTEC map (input space) with m attributes, i.e. the number of pixels, encoded as vectors $\mathbf{x} \in S$. Intuitively, this means that for each $\mathbf{x} \in S$ the distance $\|\mathbf{x} - \mathbf{c}_{f(x)}\|$ between x and the closest centroid $\mathbf{c}_{f(x)}$ should be small.

The LVQ clustering algorithm can be summarized as follows:

1. We define the number of centroids p and the number of times (number of epochs) for which the whole database is run through the algorithm.

2. We initialize the values $C = \{\mathbf{c}_1, \ldots, \mathbf{c}_p\}$ of the p centroids from p input observations randomly selected. After training, every centroid $l \in \{1, \ldots p\}$ will represent a set of normalized polar VTEC maps, and the weight vector $\mathbf{c}_l$ will approximate to the *center of mass* of this set.

3. We initialize counter: j that denotes the iteration, i.e. the updated timestamp of the centroids.

4. For iteration 1 to number of epochs:

   (a) For each of the n training vectors of the overall data base, $\mathbf{x}_i$, the following procedures are carried out:

i. We find the node k whose weight $\mathbf{c}_k$ best approaches $\mathbf{x}_i$ (d represents in this case the Euclidean distance in the space $\mathbf{R}^n$, where n is the number of grid values of any polar VTEC map: $d(\mathbf{c}_k, \mathbf{x}_i) \leq d(\mathbf{c}_l, \mathbf{x}_i)$, $\forall l \in \{1, \ldots, p\}$.

ii. We update the weight of the winning node k and its neighbours, $N_k(i)$, approaching the training vector as closely as possible:

$$\mathbf{c}_l(i) = \begin{cases} \mathbf{c}_l(i-1) + \alpha(i)\left[\mathbf{x}_i - \mathbf{c}_l(i-1)\right] & \forall l \in N_k(i) \\ \mathbf{c}_l(i-1) & \forall l \in \{1, \ldots, p\} - N_k(i) \end{cases} \tag{3.1}$$

here $\alpha(i)$ is a suitable, monotonically decreasing sequence of scalar-valued gain coefficients, $0 < \alpha(i) < 1$. The justification of this parameter is related to the Robbins-Monro algorithm (Robbins and Monro, 1951), which guarantees the convergence of an iterative estimation of a mean parameter of a Gaussian distribution. A choice for fast convergence is, for example, a linear decrease of $\alpha(i)$ during the first 1000 epochs in a range between 0.9 and 0.1 (ordering period). Then after this initial phase, $\alpha(i)$ should attain a final value below or equal to 0.01, with a decrease proportional to the inverse of the iteration number, i.e. $\alpha(i) \propto 1/i$.

The distribution of $\{\mathbf{c}_1, \ldots, \mathbf{c}_p\}$ is an approximation of the continuous probability density function of the vectorial input variable $\mathbf{g}(\mathbf{x})$ (actually if follows $[\mathbf{g}(\mathbf{x})]^{\frac{m}{m+2}}$, Kohonen (1990), p. 1466).

3.4.2 Clusters in north and south polar regions

We analyzed with LVQ the time series of polar VTEC maps during over 6600 days from January 1st, 2001 to February 14, 2019, from the inputs consisting of about 640000 UQRG GIMs with a sampling time interval of 15 minutes.

Since the polar ionosphere has pronounced daily variations depending on universal time (David et al., 2016; Hunsucker and Hargreaves, 2007), each UT in the dataset has been examined independently. The geographic coordinate system is selected to show the electron content distribution, because this can help avoid any interpolation, and analyze directly the values provided by the GIMs, and by μ_2, regardless of the level of magnetic field deviation from the standard dipolar model. It is worth noticing that both magnetic poles in north and south hemispheres present a slow drift during the period in question: from 81.3°N 160.06°W and 64.6°S 138.5°E respectively in 2001, to 86.29°N 160.06°W and 64.28°S 136.59°E in 2015 (see for instance *https://en.wikipedia.org/wiki/South_Magnetic_Pole*, Mandea and Purucker, 2018 and Witze, 2019). And this can produce a small smoothing effect, specially

in the north polar region. The NP and SP were split with 45°N and 45°S as the respective latitudinal borders, and the GIM resolution of 5°, 2.5° and 15 minutes in longitude, latitude and time is maintained, which is high enough to detect large-scale patches with hundreds of kilometers to several thousand kilometers in the horizontal dimension, as it has been illustrated in Section 3.3.

To study this long time period, the 1,260,000 polar VTEC maps were normalized by a L2 norm as a preprocessing step before the clustering procedure. The geomagnetic activity has not been taken into account due to the relatively small percentage of significantly active days (see Figure 3.13). For the period considered, i.e. from 2001.0 to 2018.3, 92% of the time is free from geomagnetic storms (Kp$<$ 4). So the clustering results should be considered representative of the predominant quite-time conditions.Therefore we are able: (1) To detect the most frequent features, also with low ionization level, e.g. during nighttime under minimum solar cycle conditions; the time evolution and asymmetry between both poles of corresponding mean VTEC values are shown in Figure 3.14, which are consistent with the VTEC annual asymmetry with higher values in January than in June (Gulyaeva et al., 2014). And (2) to use the inner product among the normalized vectors representing each polar VTEC map to derive their distance (see in Figure 3.15 the mean projection of every polar VTEC map regarding the corresponding cluster in both polar regions, also in agreement with higher asymmetry around south pole). The unsupervised LVQ algorithm, as indicated in Section 3.4.1, was applied independently for each UT and polar region on the time series of normalized polar VTEC maps, providing the corresponding clustering and representative map.

After considering different maximum numbers of centroids in the LVQ clustering procedure of the normalized polar VTEC maps, we selected 4 because it provided more clear differences between clusters, easier to interpret. In fact the typical clustering result of three centroids obtained in the majority of the 96 UT values (from 0000 UT, every 15 minutes) can be interpreted as the existence of just three main groups of GIMs, which are described below. Additionally, we have considered the polar maps of the topside electron content fraction, μ_2, which have been helpful in some cases in Section 3.3 to interpret VTEC features in terms of changes in the vertical electron content distribution.

The clustering representatives of the normalized GIMs defined with latitudes above 45°N are shown in Figure 3.16 and 3.17 for the north polar region and in Figure 3.19 and 3.20 for the south polar one. They are shown from top to bottom every 2 hours, starting from 0145 UT, corresponding every column to each one of the three groups of clusters.

In Figure 3.16 and 3.17 it can be appreciated that the NP structures corresponding to the three groups of normalized VTEC clusters mostly rotate in function of UT, following

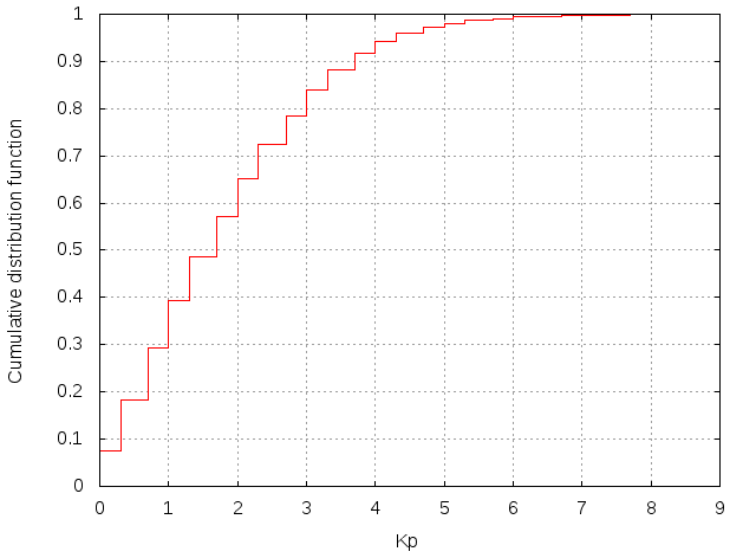

Figure 3.13 Kp cumulative probability distribution function from 2001.0 to 2018.3 (source:NOAA)

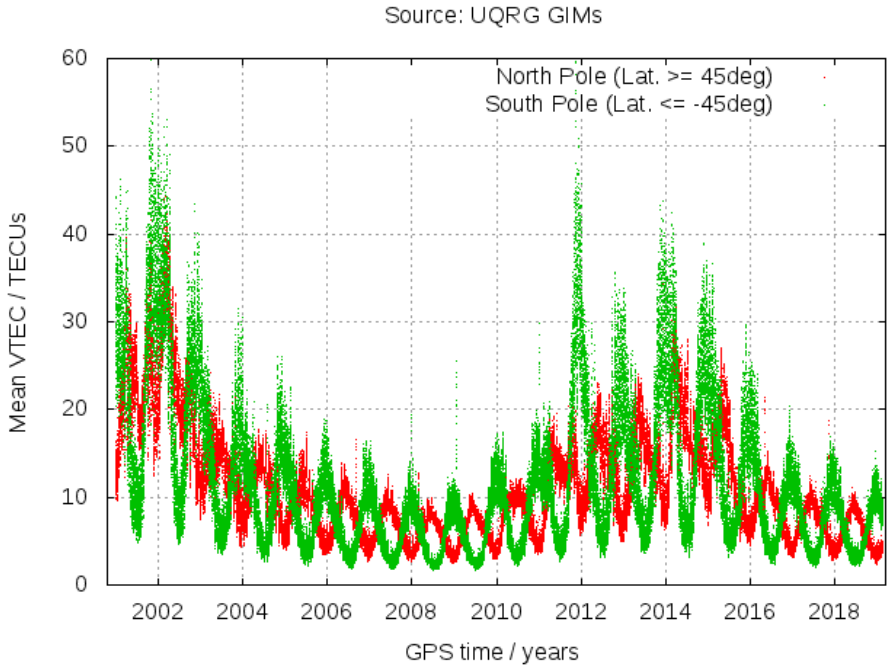

Figure 3.14 Average VTEC evolution for NP and SP (red and green points respectively), extracted from UQRG GIMs from 2001.0 to 2019.5

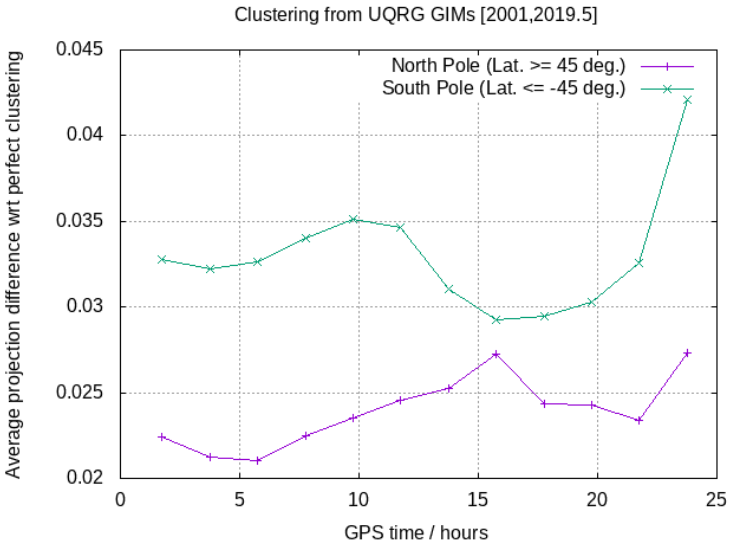

Figure 3.15 Mean of the projection difference of the overall analyzed UQRG GIMs from 2001.0 to 2019.5 regarding the cluster representative for the north and south polar regions, vs. the time corresponding to each independently performed LVQ

a main Local Time (LT) dependence. These clear patterns are different from the SP ones, which distort and change more significantly (Figure 3.19 and 3.20). This is consistent with the north-south asymmetry in the geomagnetic field, as described in (Laundal et al., 2017), where it is shown how the Earth's magnetic field deviates significantly from dipolar model at ionospheric altitudes, especially in terms of magnetic field strength, and the offset between geographic and magnetic poles (higher in the southern hemisphere, see the end of Section 5.2.1 in Hunsucker and Hargreaves, 2007). This asymmetry also explains why the repeatability of μ_2 found in each group of clusters, when it is represented vs. LT for a given latitude, is higher in NP (the third row of Figure 3.18) compared with SP (the third row of Figure 3.21).

In order to detect solar-cycle- and seasonal- related patterns, the histograms of occurrence per year, and per day of year, which are very similar for the overall UTs given a group of clusters, are also represented in the first and second rows of Figure 3.18 and 3.21, for the north and south polar regions, respectively (they follow the same column-wise ordering of the corresponding groups of clusters as the same as in the previous figures).

The ionospheric trough can be clearly appreciated in the second group of normalized NP VTEC map clusters (the second column of Figure 3.16 and 3.17). It is distributed in latitudes around 60°N, from around 0000LT to 0600LT, typically from 0015LT to 0515LT. These characteristics have become visible through the use of the equalization technique (Gonzalez and Woods, 2002). The equalization technique is commonly used in image processing, and

its purpose is to increase the contrast of the images, i.e. the distance between the lightest and darkest value. This means that ionization patterns, which may be hidden by the small difference in intensity (i.e. VTEC level), can be appreciated more clearly. The trough happens mostly during Solar Maximum conditions, and from September to November and from February to March (see the first and second row in second column of Figure 3.18). The higher value of the topside electron content fraction μ_2 at night happens in this second group of clusters, which reaches up to 0.9 coinciding with the trough occurrence at latitude 60°N (see the plot in second column and third raw of Figure 3.18), confirming as well in climatological terms the simultaneous electron content uplift found in the trough case study summarized in Subsection 3.3.2.

It can be seen in the third group of NP clusters (the third column in Figure 3.16 and 3.17) a systematic ring of relatively high electron content in the night sector, from about 55°N to 90°N and from around 2100LT to 0300LT. This happens specially from 2345 UT to 1545 UT, and under Solar Minimum conditions and from November to February, i.e. in winter and part of local fall (see occurrence histograms in the first and second row of the third column in Figure 3.18). A less clear ring is also found in the second group of clusters of NP (the second column of Figure 3.16 and 3.17). It appears during Solar Maximum conditions in a similar LT interval but mostly during the period from September to November and from February to March (see plots in the first and second row of the second column in Figure 3.18).

Mean relative structures of electron content resembling TOIs or partial rings, or either dual rings (see Subsection 3.3.5), can be also found during the time from 1745 UT to 2145 UT in clusters, represented in columns 3 and 2 of Figure 3.16 and 3.17, mostly happening during local summer, spring and fall seasons at any solar cycle time (Figure 3.18).

Finally, the predominant group of clusters of relative polar NP VTEC, represented in the first column of Figure 3.16 and 3.17, presents a flatter shape with maximum being situated around the Sun direction, and concentrated at any solar cycle time in local spring and summer, which seems associated to the predominant daylight conditions (the first column and the first and second rows in Figure 3.18).

As it has been mentioned above, and similar to the NP, the three main clusters obtained after the unsupervised clustering of the normalized south polar GIMs, defined with latitudes south of 45°S, can be seen every 2 hours from 0145 UT in the corresponding columns of Figure 3.19 and 3.20. The third group of SP clusters (the third column of plots) shows a typical relative bimodal electron content depletion at night zone, especially from 2145 UT to 0545 UT, more frequent under Solar Minimum conditions, and from April to August i.e. within local fall and winter seasons (see the third column of Figure 3.19 and 3.20 and the first and second rows in Figure 3.21). A predominant single depletion is also found

more frequently during Solar Maximum conditions in a similar UT time interval but during March-April and July-October (see the second column of plots in Figure 3.19 and 3.20, and in Figure 3.21 - the first and second row-). Other structures appear in SP during the rest of UTs, 0745 UT to 1945 UT, for the same seasons and predominant Solar Cycle phases in the third and second group of clusters (see above mentioned figures): relative theta-aurora-like patterns in 1145-1575 UT (see corresponding example in Subsection 3.3.4) and curly electron content shapes (both in the third column in Figure 3.19 and 3.20 and from April to August), and TOIs (the second column) with similar solar-cycle and seasonal occurrence as in 0745-1945 UT interval, i.e. Solar Maximum conditions during March-April and July-October. The first group of SP clusters shows a flatter distribution, but with a clear mean TOI behaviour during 1345-1945 UT, from November to February, i.e. around local spring and summer seasons, in agreement with the results reported from Swarm measurements in Chartier et al. (2018).

3.5 Summary

In this chapter, the electron content distribution of the north and south polar ionosphere from 2001 to the beginning of 2019 is analyzed by using GIM VTEC, computed every 15 minutes by UPC-IonSAT with a tomographic-kriging combined technique. We firstly show that the accuracy of UQRG GIM is slightly better than that of the GIMs of other analysis centers on the whole and also over both poles. Secondly, we show examples of polar VTEC features in UQRG GIM, previously reported by different authors and with higher-resolution techniques. UQRG GIMs provide an unprecedently valuable dataset regarding the spatial and temporal coverage for the climatology study of interesting ionospheric features in the polar regions, opening a new opportunity for detection and thus probably provide new evidence and arouse new insights for plausible theoretical assumptions. Thirdly, by means of an unsupervised clustering algorithm, learning vector quantization, we characterize the main features of the ionospheric electron content climatology, separately for the north and south polar regions. It is worth mentioning that the unsupervised clustering results demonstrate that TOI and polar cap patches exhibit an annual dependence, i.e. occurring in the North Hemisphere winter and the South Hemisphere summer, which is consistent with the conclusion in Chartier et al. (2018).

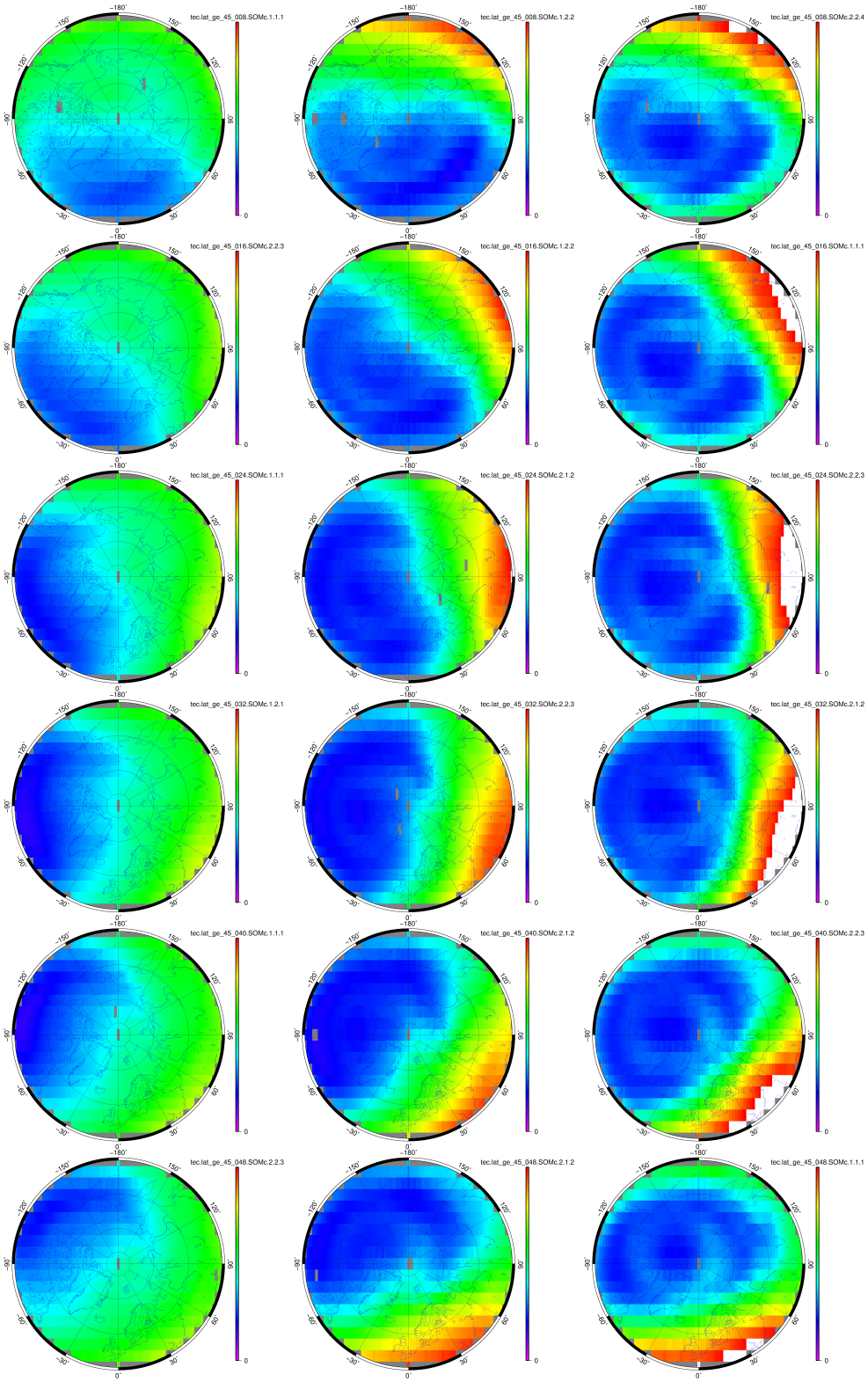

Figure 3.16 Centroids of normalized NP VTEC maps (north of 50°N) in the LVQ computed with 2x2 neurons from UQRG VTEC GIMs from 2001 to the beginning of 2019 for 01.75UT (the first row), 03.75UT (the second row), 05.75UT (the third row), 07.75UT (the fourth row), 09.75UT (the fifth row) and 11.75UT (the sixth row).

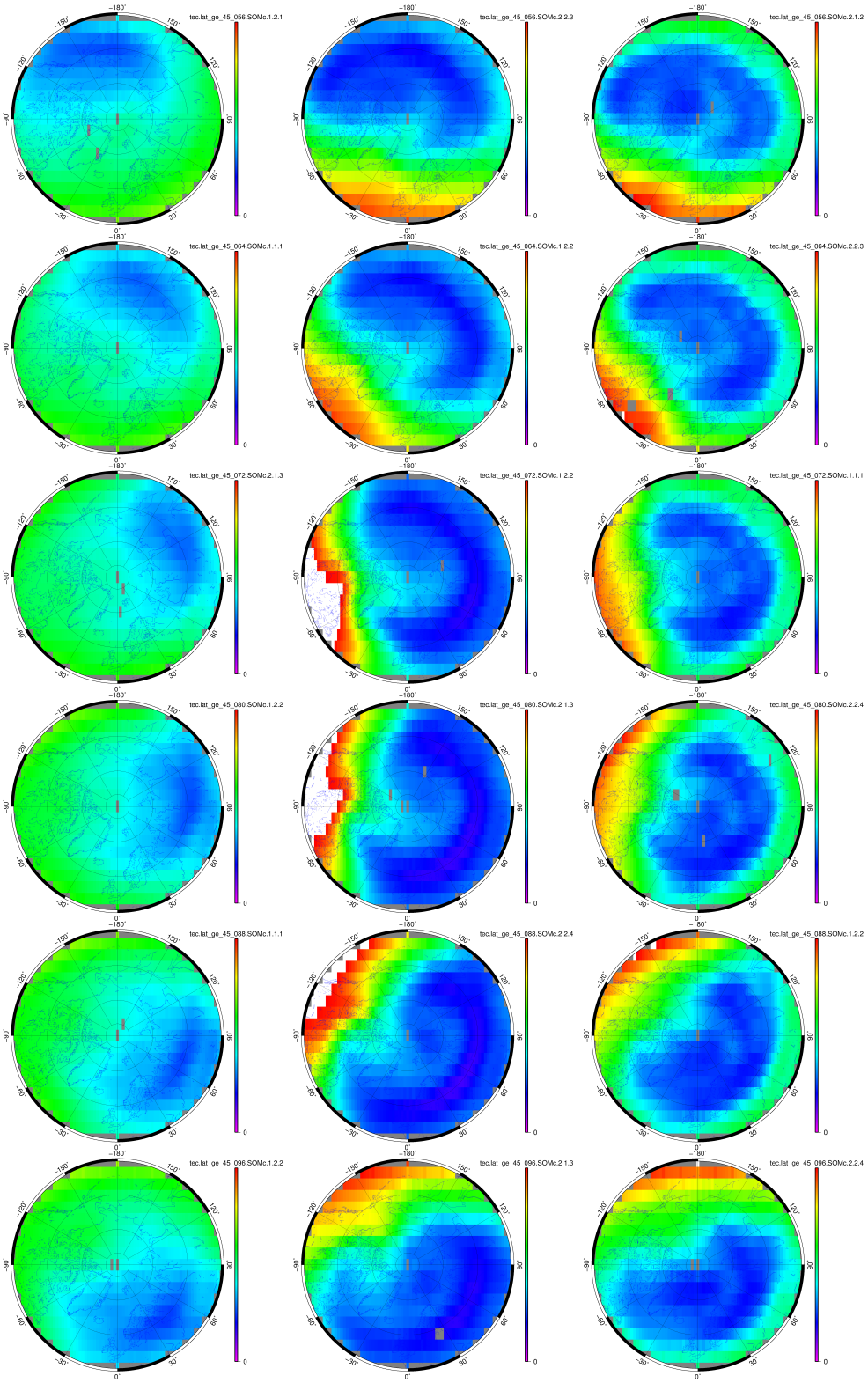

Figure 3.17 Centroids of normalized NP VTEC maps (north of 50°N) in the LVQ computed with 2x2 neurons from UQRG VTEC GIMs from 2001 to the beginning of 2019 for 13.75UT (the first row), 15.75UT (the second row), 17.75UT (the third row), 19.75UT (the fourth row), 21.75UT (the fifth row) and 23.75UT (the sixth row).

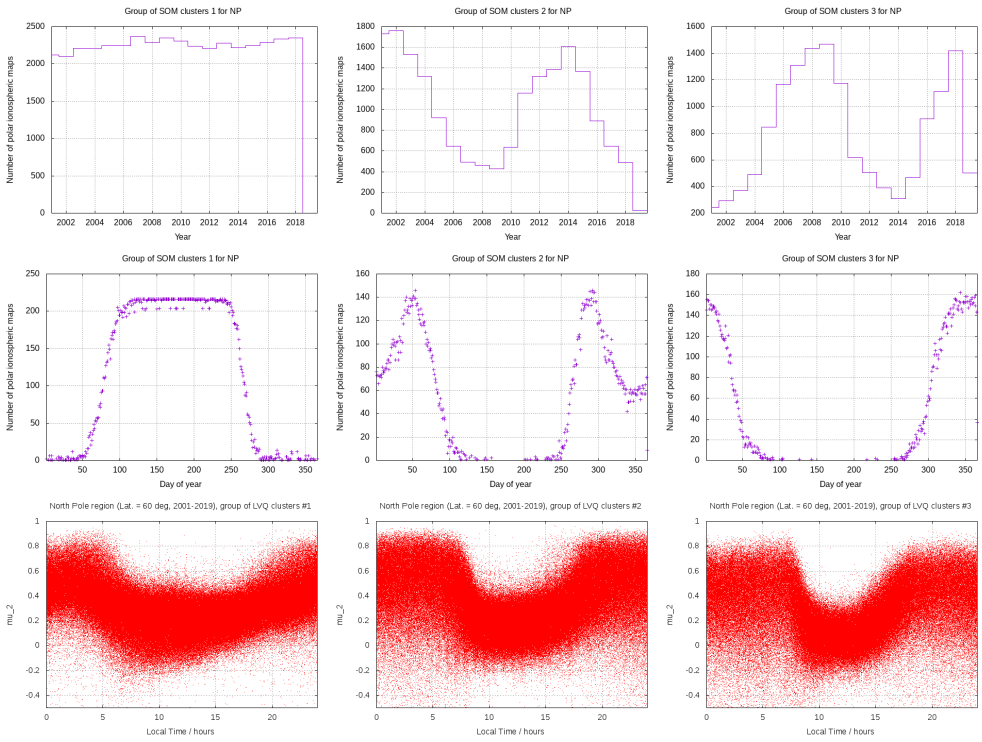

Figure 3.18 Occurrence per year (the first row), occurrence per day of year (the second row) and μ_2 values at latitude 60°N vs. Local Time of the north polar region GIMs associated to the first, second and third group of clusters (the first, second and third column respectively) for all the times.

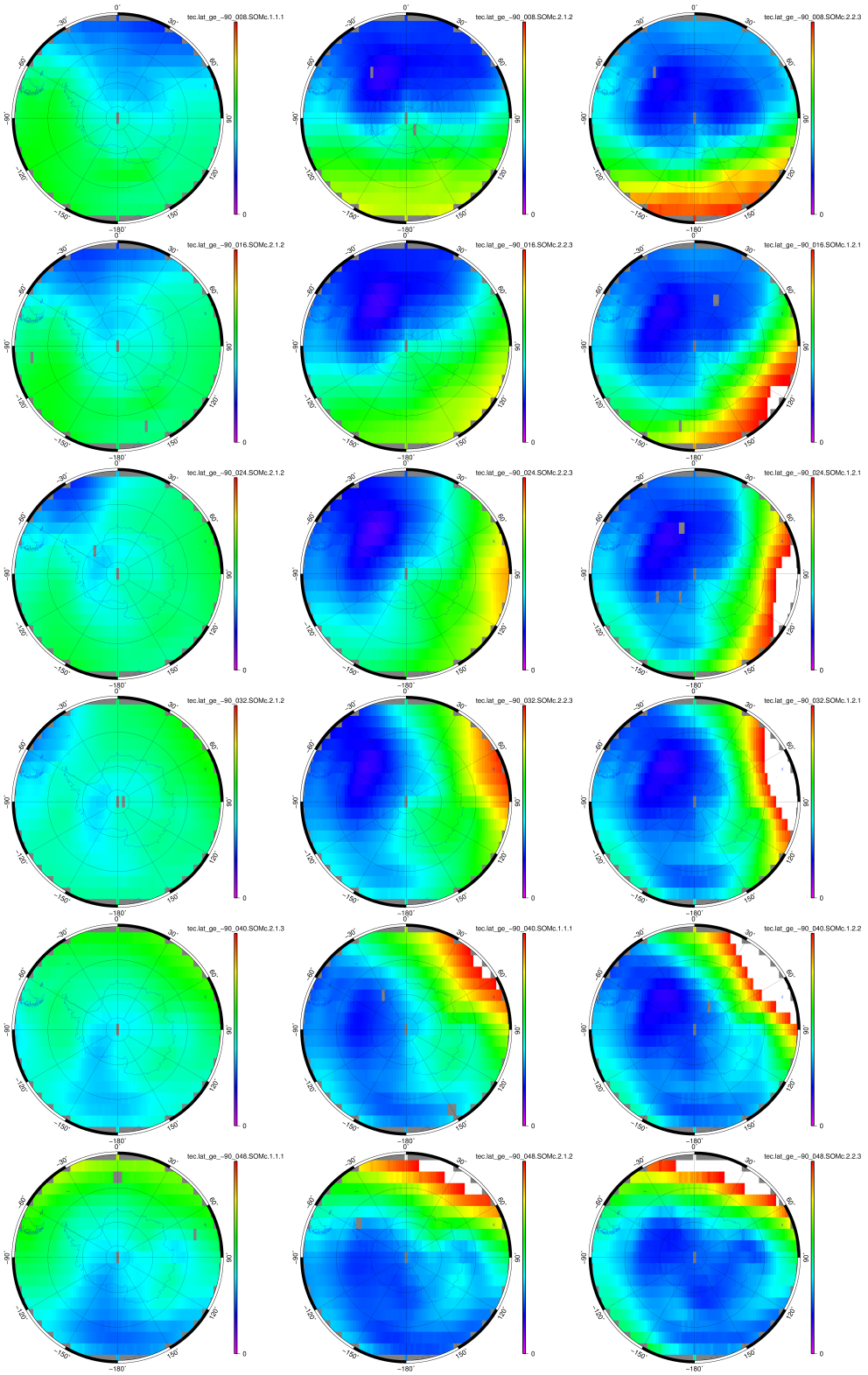

Figure 3.19 Centroids of normalized SP VTEC maps (south of 50°S) in the LVQ computed with 2x2 neurons from UQRG VTEC GIMs from 2001 to the beginning of 2019 for 01.75UT (the first row), 03.75UT (the second row), 05.75UT (the third row), 07.75UT (the fourth row), 09.75UT (the fifth row) and 11.75UT (the sixth row).

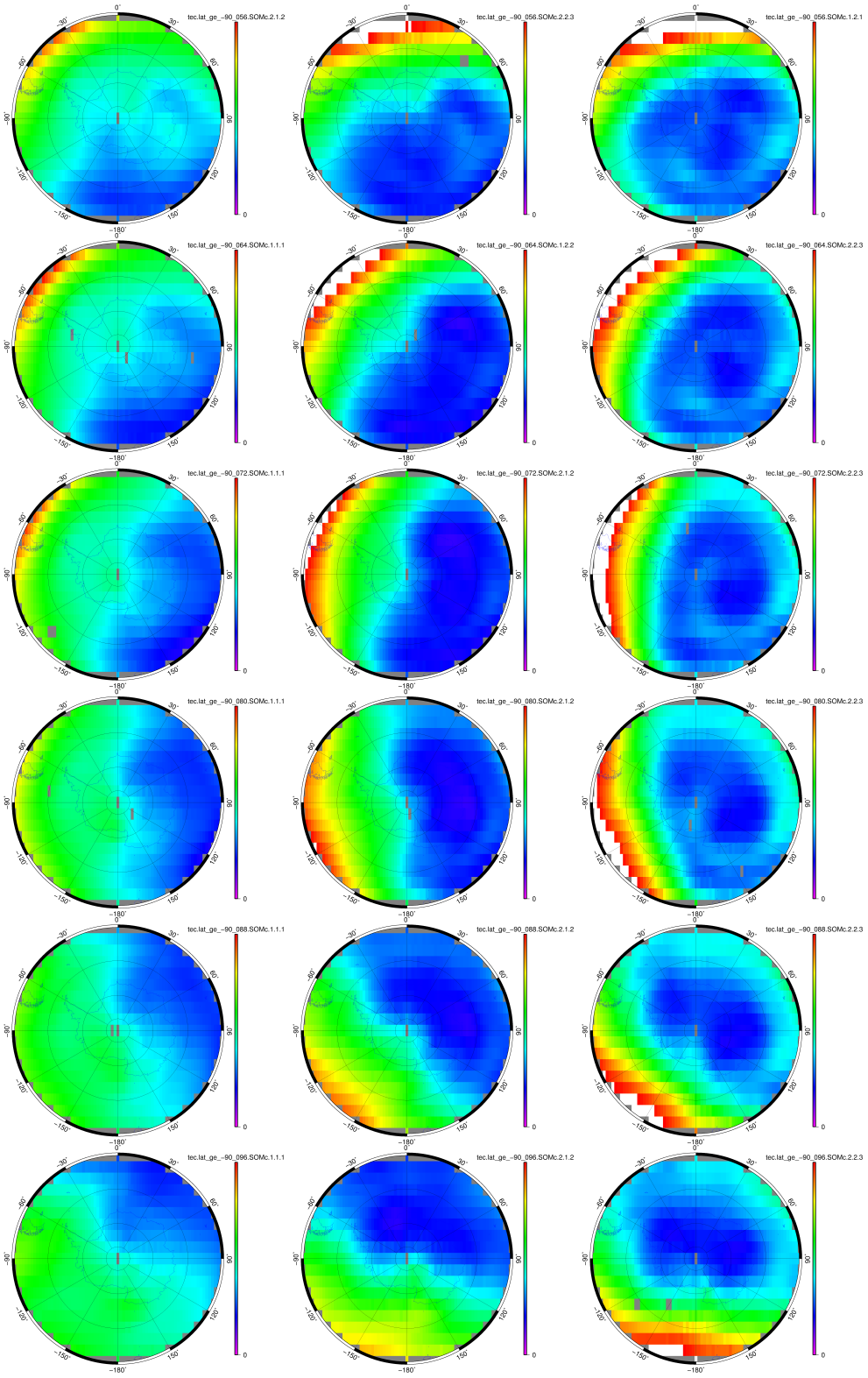

Figure 3.20 Centroids of normalized SP VTEC maps (south of 50°S) in the LVQ computed with 2x2 neurons from UQRG VTEC GIMs from 2001 to the beginning of 2019 for 13.75UT (the first row), 15.75UT (the second row), 17.75UT (the third row), 19.75UT (the fourth row), 21.75UT (the fifth row) and 23.75UT (the sixth row).

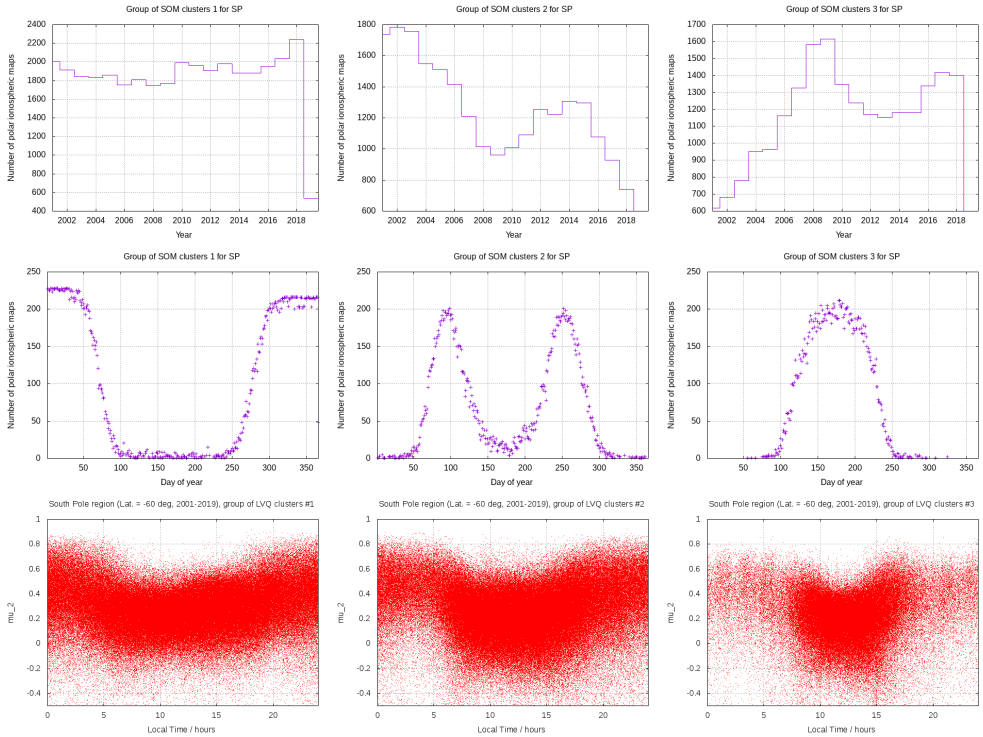

Figure 3.21 Occurrence per year (the first row), occurrence per day of year (the second row) and μ_2 values at latitude 60°S vs. Local Time of the south polar region GIMs associated to the first, second and third group of clusters (the first, second and third column respectively) for all the times.

Chapter 4

Improvement of the Abel inversion of top-truncated RO ionospheric data: AVHIRO

4.1 Introduction

GNSS ionospheric radio occultation (IRO) data provide globally rich information to study the vertical electron density structure of the ionosphere. In the near future, at least 20000 occultations per day, with better coverage in low and high latitudes, will be reached under the recommendation and promotion of International Radio Occultation Working Group (IROWG), in cooperation with worldwide space agencies and commercial entities. This will boost the research in the field of numerical weather prediction, climate and space weather, and help further speed up the application of new results at an operational level. Among different low earth orbit (LEO) satellite missions, European Organization for the Exploitation of Meteorological Satellites (EUMETSAT) Polar System - Second Generation (EPS-SG) will play an important role in providing global observation. The new RO instrument on board EPS-SG satellites, flying at a height of 820 km, focuses on neutral atmospheric profiling. It will provide truncated ionospheric RO data, only below impact heights of 500 km, in order to guarantee a full data gathering of the neutral part. The key problem in electron density profile inversion from truncated IRO data in EPS-SG, is rank deficiency of the normal matrix in the least square estimation by means of Abel inversion. Therefore, realistic external constraints need to be added to the observation equations to solve the unknowns.

The Chapman function is the classical representation of electron density profile in the ionosphere (Chapman, 1931). Rishbeth and Garriott (1969) suggested the use of a modified a-

Chapman function, which takes account of the height variation of the scale height. (Reinisch et al., 2007) proposed a vary-Chap function, i.e. an α-Chapman function with a continuously varying scale height, where a hyperbolic tangent function is adopted to represent the scale height variation with height above the F_2-layer peak, and the data from IMAGE/RPI and ISIS were used to estimate the parameters in the vary-Chap function.

In this thesis to avoid confusion, the Vary-Chap model, where the scale height varies linearly with height above F_2-layer peak, is different from the vary-Chap function in Reinisch et al. (2007). This linear Vary-Chap model can well describe the topside ionosphere (Olivares-Pulido et al., 2016), based on retrieved electron density profiles from FORMOSAT-3/COSMIC GPS occultation data by the Improved Abel transform inversion technique, which takes into account the horizontal electron content gradients (Hernández-Pajares et al., 2000a). This linear relationship agrees with the expected linear temperature dependence. A new Vary-Chap-based Extrapolation Technique of electron density (VCET) for impact parameters of 500 km up to the EPS-SG orbit altitude was developed (Hernández-Pajares et al., 2017a), showing better performance than other classical Chapman models. This good performance is conditioned on accurate estimation of electron densities below certain ceiling height, e.g. 500 km in the experiment, which is a challenge in the retrieval from truncated RO data, with more than 40% of measurement missing in the case of new LEO mission EPS-SG.

Two methods were proposed to solve the problem: the Abel-VaryChap Hybrid, and the Simple Estimation of Electron density profiles, both modeling from topside Incomplete RO data (AVHIRO and SEEIRO, respectively). The two approaches do not depend on external models or data beyond the radio-occultation measurements. AVHIRO priorizes the accuracy and SEEIRO priorizes the estimation computating time in order to allow near real-time usage. The assessment of both techniques is presented with measurements of COSMIC/FORMOSAT-3 truncated up to 500 km, during 4 representative periods (Figure 4.2), by comparing the electron density profiles with the corresponding ones obtained from the full radio-occultation measurements. The chapter will introduce AVHIRO method in detail, and the description of SEEIRO method can be found in Lyu et al. (2019a).

4.2 Methodology

A set of radio-occultation measurements gathered from the LEO, in this case the COSMIC/FORMOSAT-3 at height about $r_L = 800$ km is selected for the experiment. And the data are truncated to a maximum impact parameter height equal to the expected value of $r_0 = 500$ km for EPS-SG. The dual-frequency ionospheric phase combinations, $L_I = L_1 - L_2$, are corrected by substracting STEC above the LEO orbit. These STEC values are computed from POD

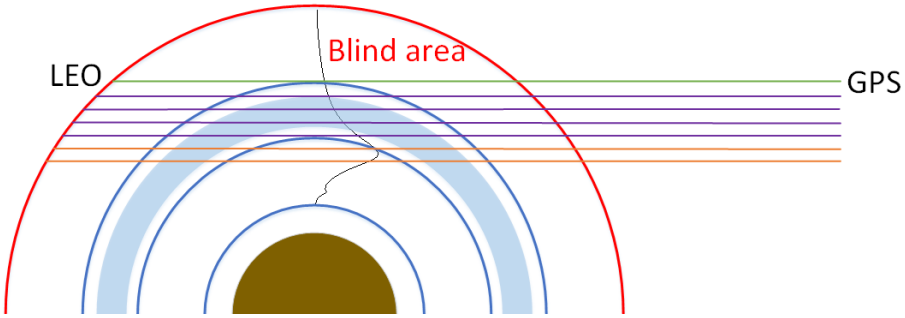

Figure 4.1 Layout of the incomplete RO measurements scenario studied in this work, showing up, as conceptual example, some transmitter-receiver rays illuminating three layers, in green, magenta and orange colors. The height interval used to fit the Vary-Chap model is also represented (light blue color)

antenna measurements, i.e. with positive elevations, by means of a dual-layer tomographic voxel model which simultaneously estimates the electron density of the topside voxels and the carrier phase ambiguities, as described in Hernández-Pajares et al. (2017a).

AVHIRO, which consists of Abel inversion and Vary-Chap model. It synergistically solves the full electron density, ambiguity term and four parameters of Vary-Chap model at the same time, taking into account the nonlinear interactions between the unknown parameters. As it has been indicated above, the Vary-Chap model summarizes the expected distribution of the topside electron density. And it is applied as constraint to improve the accuracy of the overall electron density estimation. Specifically, and following Figure 4.1, we can relate the ionospheric combination in length units, $L_I = L_1 - L_2$, where L_1 and L_2 are the carrier phases measured in frequencies f_1 and f_2, with the known crossing lengths $l_{j,k}$ of the corresponding j-th line-of-sight with each given k-th layer, and with the unknown electron density values N and carrier phase ambiguity in length units B_I. Following Hernández-Pajares et al. (2011), B_I contains the integer terms in cycles, $\lambda_m N_m$, and instrumental phase delays for receiver and satellite, respectively δb_m, $\delta b'_m$, and for frequencies $m = 1, 2$:

$$B_I = B_1 - B_2 = \lambda_1 N_1 - \lambda_2 N_2 + \delta b_1 - \delta b_2 + \delta b'_1 - \delta b'_2$$

In this context we can express the ionospheric combination of carrier phases, from top to bottom, as:

$$\begin{aligned}
(L_I)_1 &= \alpha\,(2l_{1,1}N_1 + 2l_{1,2}N_2 + \ldots + 2l_{1,x}N_x) + B_I \\
(L_I)_2 &= \alpha\,(2l_{2,1}N_1 + 2l_{2,2}N_2 + \ldots + 2l_{2,x}N_x + 2l_{2,x+1}N_{x+1}) + B_I \\
(L_I)_3 &= \alpha\,(2l_{3,1}N_1 + 2l_{3,2}N_2 + \ldots + 2l_{3,x}N_x + 2l_{3,x+1}N_{x+1}) + B_I \\
&\ldots \\
(L_I)_6 &= \alpha\left(2l_{6,1}N_1 + 2l_{6,2}N_2 + \ldots + 2l_{6,x}N_x + 2l_{6,x+1}N_{x+1} + 2l_{6,x+2}N_{x+2}\right) + B_I \\
&\ldots
\end{aligned} \tag{4.1}$$

The observation set of equations 4.1 can be summarized in matrix notation as $Ax = b$, where $x = (N_1, \ldots, N_x, \ldots, B_I)^T$ and $A_{j,k} = 2\alpha \cdot l_{j,k}$ for $k < M$ and $A_{j,M} = 1$ for the ambiguity coefficient, being $\alpha = 1.05 \times 10^{-17}$ m^3 the scaling factor converting electron content into delay (see Hernández-Pajares et al. (2011)) and being M the number of unknowns.

From these equations we cannot apply directly the Abel inversion algorithm (see for instance Hernández-Pajares et al. (2000a)), because the design matrix A is rank deficient due to the lack of observations above 500 km. In order to solve such rank-defect equations, the Vary-Chap model is added as constraint above 500 km, as indicated above, with parameters mainly estimated within the height range of 380 km to 430 km. The Vary-Chap model allows an extrapolation compatible with the observational data.

The Vary-Chap model is based on a non-linear interaction between the parameters to be estimated. So in order to use it as prior, it is important to be aware of the difficulties related to the parameter estimation. The structure of the Vary-Chap model consists of two exponential terms of a variable z , as can be seen in Eq.(4.2). This variable z consists of terms that have to be estimated such as h_m and H. The estimation of these parameters by means of the conventional methods based on gradient search is difficult (Luenberger et al., 1984). This difficulty is due to the fact that small variations in the parameters give rise to very large changes in the value of the derivative, caused by the dependencies inside the exponential functions. These large changes are explained by the different scale of the values of the parametes and also by the nonlinear terms of the expression, which can be summarized as a multiplicative interaction between the parameters (i.e. N_m), the exponencial of the inverse of a variable (i.e. $e^{\frac{1}{H}}$) and a double exponential of z.

A family of estimation methods that is robust to the problems of differentiability of the target function are the algorithms for minimization without derivatives. This family of algorithm searches for the optimum by comparing perturbations of a given candidate to the solution. The fact that instead of computing a derivative, they rely on comparisons, removing the problems related to the extreme variability of the derivatives, and the different

scale of the unknowns. There are different algorithms in this family such as the Powell's method, the Nelder Mead algorithm and the pattern search(see for instance Press et al. (1989)). Due to the differences of scale of the parameters to be estimated, we selected the algorithm that in principle is more rubust to this phenomenon, which is the Powell search method (Powell, 1964). This algorihm was used to estimate the electron densities below 380 km, the ambiguity term and four Vary-Chap parameters, which are peak height h_m, peak eletron density N_m, scale height at peak H_0 and the derivative of scale height $\partial H/\partial h$, simultaneously. Afterwards, the electron densities above 380 km are updated from the Vary-Chap model using the estimated parameters. The expression that relates the electron density N, with the height h, is the following,

$$N = N_m e^{\frac{1}{2}(1-z-e^{-z})}, \quad where\ z = \frac{h-h_m}{H} \tag{4.2}$$

$$H = \frac{\partial H}{\partial h}(h-h_m) + H_0 \tag{4.3}$$

where N and H represent the electron density and scale height at height h above peak respectively.

The cost function of powell search is mainly composed of two terms: one is $\|Ax-b\|^2$ and the other is the difference with respect to a reference estimate x_0, weighted by λ which is a regularization parameter, $\lambda\|x-x_0\|^2$. The regularization parameter λ controls the smoothness of the estimation. Besides, additional penalization terms on h_m, N_m, H_0 and $\partial H/\partial h$ are added to the cost function to constrain Vary-Chap parameters in a realistic range.

The unknown vector x in equation $Ax = b$ is composed to three parts x^1(electron densities from 380 km and 1000 km), x^2 (electron densities below 380 km) and x^{ambi}. The iterative algorithm for the estimation is described as follows:

1. Initial electron density profile below 500 km and ambiguity term are derived from Abel inversion and then the full profile is extrapolated to 1000 km. These values define the vector x_0. Next we iterate updating this vector $x_0 = [x_0^1, x_0^2, x_0^{ambi}]$ each time, following next point.

2. The terms x_0^2 (the current estimate of the electron densities below 380 km) and x_0^{ambi}, are extracted from current unknowns x_0, together with x_0^1, which is calculated with the Vary-Chap model's parameters $[h_m, N_m, H_0, \partial H/\partial h]_0$. These parameters are initialized at the beginning with typical values: h_m and N_m are derived from the very first Abel inversion neglecting the electron content above 500 km, $H_0 = 30$ km and $\partial H/\partial h = 0.05$ from Olivares-Pulido et al. (2016). They form the x_{powell}.

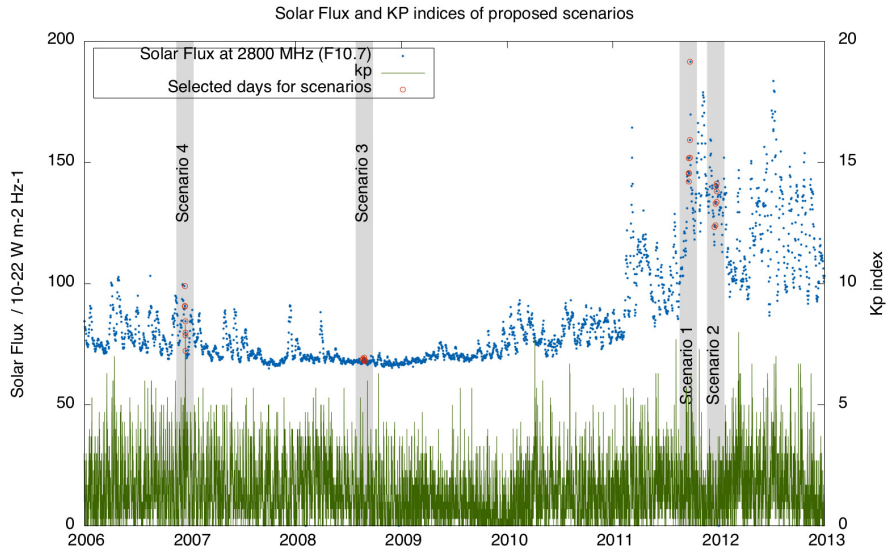

Figure 4.2 Solar Flux, Kp index during the four selected periods, extracted from Hernández-Pajares et al. (2017a).

3. The cost function of the Powell search is the sum of $\|Ax_{powell} - b\|^2$ and $\lambda \|x_{powell} - x_0\|^2$, where λ is obtained from the ratio of both estimated standard deviations in the previous iteration: the one from post-fit residuals versus the one for peak electron density. And the Powell algorithm is applied in order to estimate un update of the values $[x^2, x^{ambi}, h_m, N_m, H_0, \partial H/\partial h]$.

4. The solution at the ith iteration x_{powell_i} can be computed by the searched vector $[x^2, x^{ambi}, h_m, N_m, H_0, \partial H/\partial h]_i$. Then we update x_0 by assigning x_{powell_i} to x_0 and go to step 2. Empirically 10 iterations are performed to ensure the convergence of the algorithm.

4.3 Estimation Assessment

In order to assess the performance of AVHIRO in the height range corresponding to the observations impact parameter heights (below 500 km), we have considered the selected set of over 3700 radio-occultations corresponding to four weeks studied in Hernández-Pajares et al. (2017a). They are representative of the previous solar cycle (see Figure 4.2).

One first illustrative example is shown in Figure 4.3. The performance of one typical occultation retrieval is compared between not applying (initial solution) and applying these new techniques (last iteration). It can be seen that, in this case, the error goes down from

Table 4.1 Pros and Cons of AVHIRO vs SEEIRO: Summary

	AVHIRO	SEEIRO
Ne Relative Accuracy	8%	13%
Predominant Ne Rel. Acc.	3%	10%
Ne Absolute Accuracy	$(1.8 \pm 3.9) \times 10^{10}\mathrm{m}^{-3}$	$(3.0 \pm 4.7) \times 10^{10}\mathrm{m}^{-3}$
Predominant Ne Abs. Acc.	$< 10^{10}\mathrm{m}^{-3}$	$10^{10}\mathrm{m}^{-3}$
CPU time per preprocessed RO	20 minutes	15 seconds
Suitable for NRT service?	Not now	Yes
Required ancillary information?	No	No
Required inputs	2-freq. GPS carrier phase meas., predicted GPS and LEO orbits (both)	
Convenient inputs	2-freq. GPS POD carrier phase meas. (both)	

45-46%, to 1.3% with AVHIRO and 10.0% with SEEIRO. We will see below that these final relative errors are not far from the most frequent ones.

For the four representative periods, the comparison of the absolute and relative error RMS for AVHIRO are respectively shown in Figures 4.4 and 4.5. The error reduces from $1.1 \times 10^{11} \pm 1.4 \times 10^{11}\mathrm{m}^{-3}$ (53.0% of RMS) in the initial iteration to $1.8 \times 10^{10} \pm 3.9 \times 10^{10}\mathrm{m}^{-3}$ (15.8% of RMS) in the final one.

4.4 Extrapolation Assessment

Although the area below 500 km, tackled in the previous section, is the main target of this work, the extrapolation precision for the topside part (above 500 km in this work) should be examined, since the electron densities in the blind area have a non-negligible impact on the retrieval. In AVHIRO method, the full electron densities are estimated simultaneously, with a full linear Vary-Chap model for the topside part of the electron density profile, instead of by two steps to separate the observed and blind area. Hence the topside assessment can to some extent reflect the performance of Vary-Chap model, which is shown in this section for completeness.

From absolute errors histogram (Figure 4.6), the performance in the blind area is a little worse than but comparable to that in the area below 500 km, with bias 2.3×10^{10} m^{-3} and standard deviation 5.1×10^{10} m^{-3}, which are in the same magnitude as those in the lower part. While the relative errors (see Figure 4.7) are quite large with 57.5% of RMS compared to 15.8% in the observed area. This can be easily explained by taking into account that the electron densities above 500 km are quite small and the sample number is limited for statistics, so the small absolute errors of electron density could produce big relative errors.

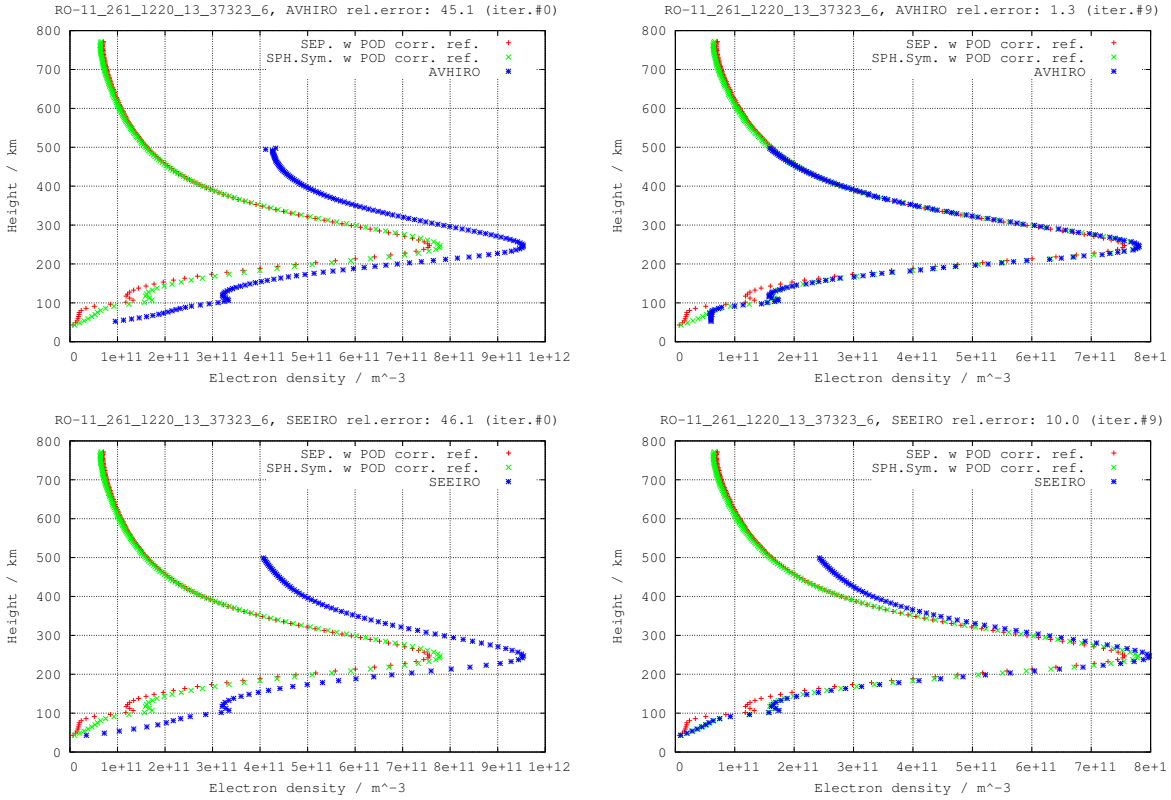

Figure 4.3 Example of the electron density (blue points) obtained from the measurements below 500 km of impact parameter height, with the AVHIRO (top row) and SEEIRO (bottom row) approaches, comparing the first and last iteration included in left- and right-hand columns respectively. It corresponds to a single radio-occultation, of satellite PRN13 with measurements from COSMIC/FORMOSAT-3 receiver L261 starting on second 37323 of day 261 of year 2011. They are compared with two different solutions obtained from the complete set of measurements. The first one has been obtained by applying Abel inversion under the assumption of spherical Symmetry (green points) and the second one modeling the horizontal variability with the Separability concept mentioned above; the profile corresponding to hmF2 tangent point is represented with red points. In both reference cases POD-data based LEO topside corrections have been applied.

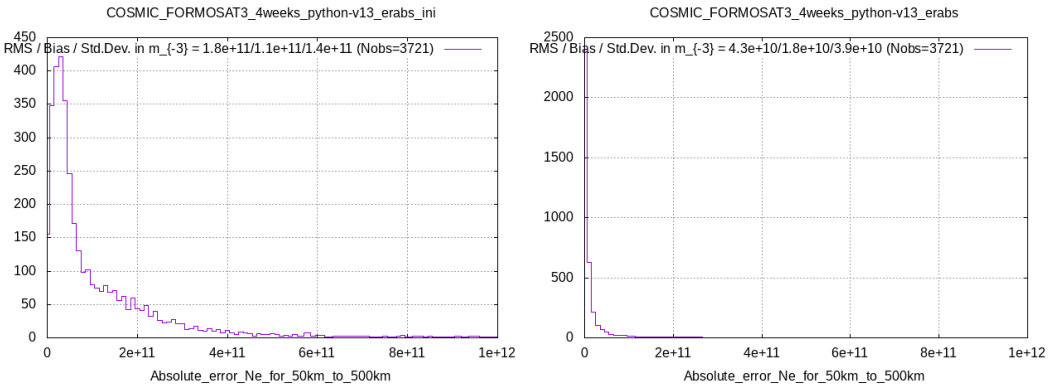

Figure 4.4 Histogram of the electron density error RMS values, one per occultation and expressed in m^{-3}. They correspond to the initial (left) and final (right) iteration of AVHIRO, for the selected COSMIC/FORMOSAT-3 radio-occultations

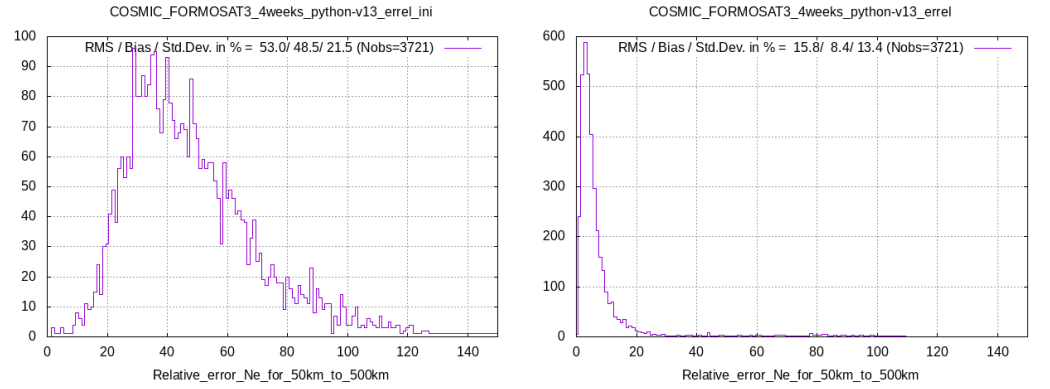

Figure 4.5 Histogram of the relative electron density error RMS values, one per occultation and expressed in %. They correspond to the initial (left) and final (right) iteration of AVHIRO, for the selected COSMIC/FORMOSAT-3 radio-occultations

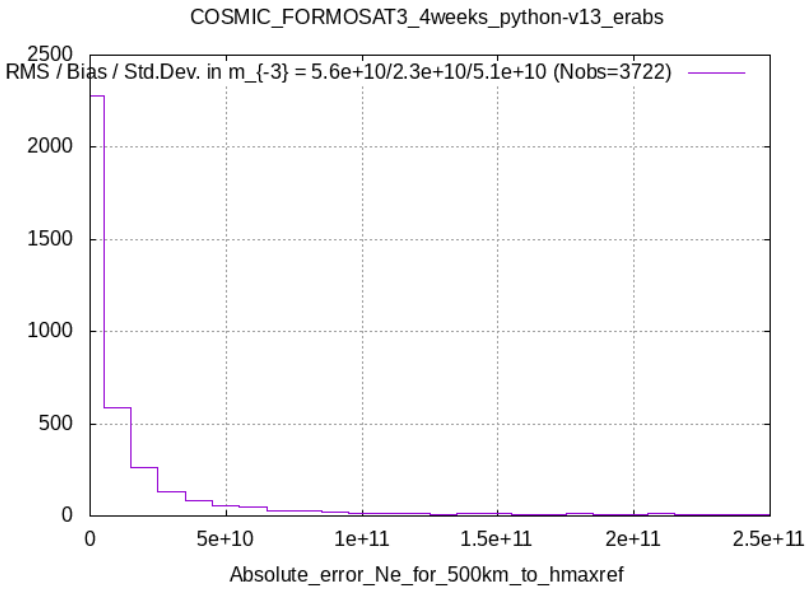

Figure 4.6 Histogram of the absolute topside electron density error RMS values, one per occultation and expressed in m^{-3}. They correspond to the final iteration of AVHIRO, for the selected COSMIC/FORMOSAT-3 radio-occultations

For example, the four cases in Figure 4.8 show that, even with high relative error (93.1%), the extrapolation results by Vary-Chap model are very close to reference values, with 8.9×10^9 m^{-3} of absolute error inside error bars. Therefore, this proves good performance of Vary-Chap model in simultaneously extrapolating the topside electron density as well. Figure 4.9 shows the variation of electron density bias and standard deviation with height, and it can be seen that both bias and standard deviation have been decreased significantly after applying AVHIRO.

4.5 Summary

In this work we have presented a new Abel-VaryChap Hybrid modeling from topside Incomplete RO data (AVHIRO). This can complete the set of algorithms for ionospheric electron density retrieval from GPS RO data in EPS-SG with lack of measurements for impact parameter heights above 500 km, as a new post-processing technique.

AVHIRO reduces, without the need of external data, the electron density error of the RO inversion with measurements up to 500 km by taking the full inversion with observations up to 800 km as reference: from 53.0% before, to 15.8% percentage of electron density RMS after applying AVHIRO. Moreover, AVHIRO provides simultaneously the linear Vary-Chapman extrapolated electron density profile with accuracy just slightly lower than that

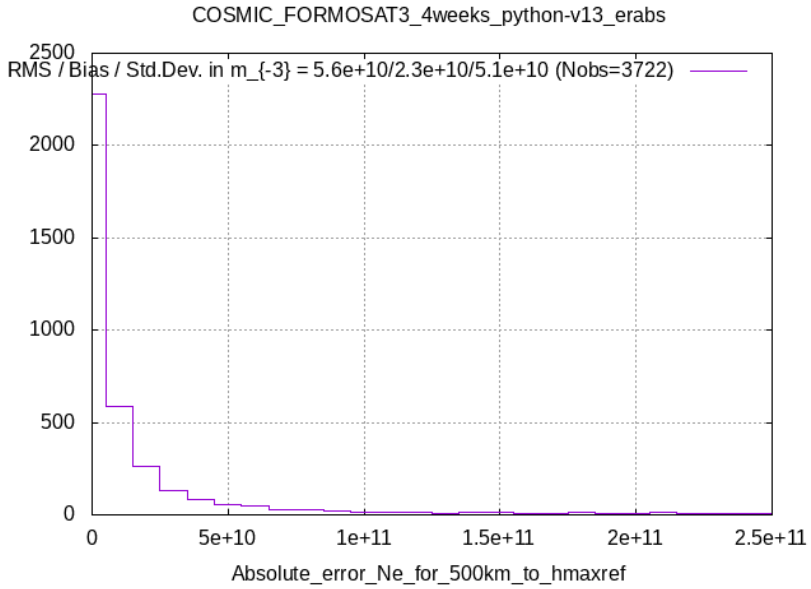

Figure 4.7 Histogram of the relative topside electron density error RMS values, one per occultation and expressed in %. They correspond to the final iteration of AVHIRO, for the selected COSMIC/FORMOSAT-3 radio-occultations

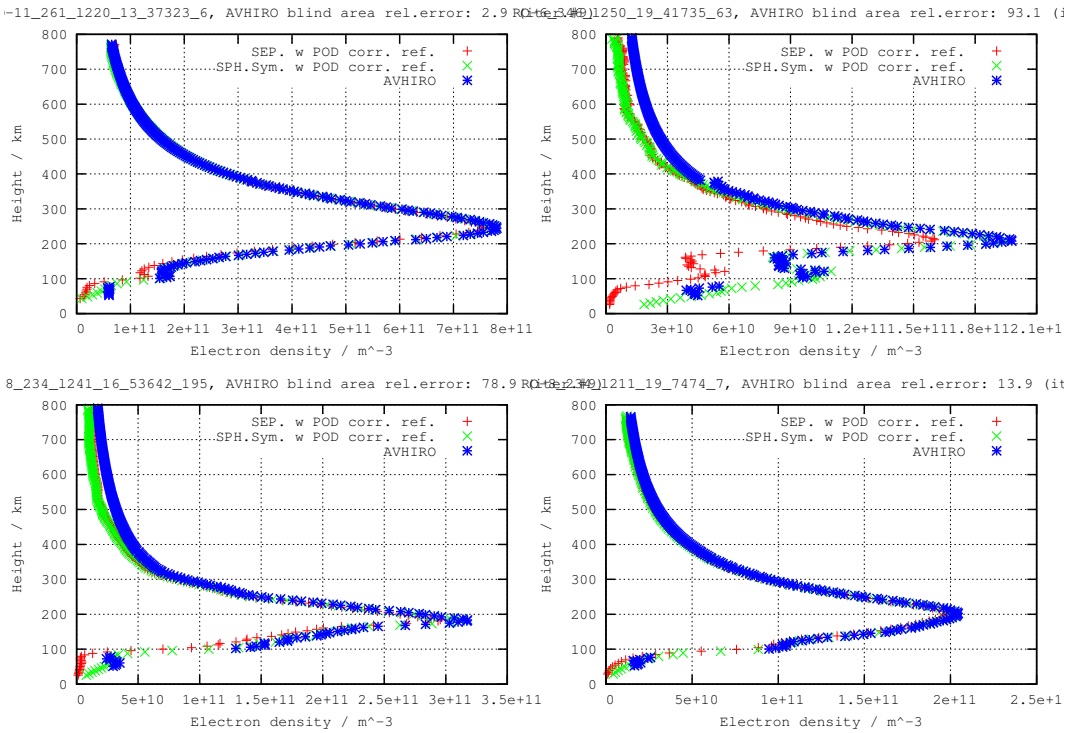

Figure 4.8 Four representative cases showing the electron density profile obtained with AVHIRO applied to the FORMOSAT-3/COSMIC measurements below 500 km, compared with the electron density profile obtained from the full RO dataset

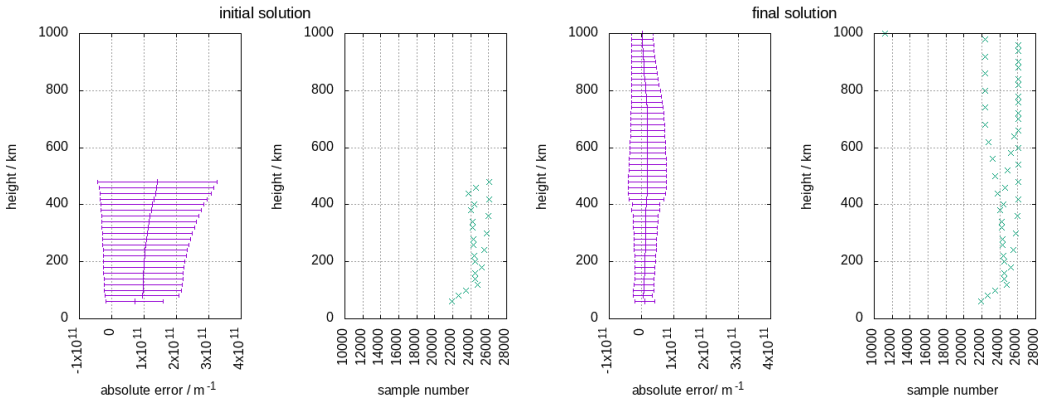

Figure 4.9 Variation of electron density bias and standard deviation with height in the first and final iteration with AHIRO for the four-week representative RO data

obtained at heights below 500 km with observations: $(2.3 \pm 5.1) \times 10^{10}$ m^{-3} above vs. $(1.8 \pm 3.9) \times 10^{10}$ m^{-3} below 500 km.

These results suggest that AVHIRO technique is appropriate, respectively, for postprocessing determination of electron density profiles from topside truncated radio-occultation data. A comparison of the main characteristics of AVHIRO and SEEIRO techniques is summarized in Table 4.1.

Chapter 5

A new way of improving Global Ionospheric Maps by ionospheric tomography based on multi-Space Geodetic dual-frequency measurements

5.1 Introduction

The characteristics of GNSS technique application in monitoring the Earth's ionosphere are its continuous and global coverage at low-cost and high precision, which are advantages over other techniques. Since IGS Ionosphere Working Group started in 1998, GIM VTEC products derived from GPS/GNSS measurements by different IGS analysis centers, have been generated with increased accuracy (Roma-Dollase et al., 2018), and increasingly used in scientific research and industry fields. Currently, more available ionospheric measurements, than those in the beginning period when IGS Iono WG was founded, are provided by multi-GNSS systems, namely GPS, GLONASS, Galileo and BeiDou. In the recent decade, in addition to GNSS, different combinations of space-geodetic measurements have been investigated as well: Todorova et al. (2008) studied the contribution of satellite radar altimetry combined with GNSS data to VTEC modeling. Alizadeh et al. (2011) exploited data from GNSS, satellite altimetry, and Formosat-3/COSMIC to improve the modeling precision in areas with few available GNSS observations. Dettmering et al. (2011) built a regional model, consisting of the climatological IRI model and the correction part expanded in terms of B-spline function by utilizing measurements of four space-geodetic techniques (terrestrial GPS, space-based GPS, altimetry, and Very-long-baseline interferometry). Doppler Orbitography

and Radio-positioning Integrated by Satellite (DORIS) measurements have been capitalized in his following work (Dettmering et al., 2014). In addition, global ionospheric modeling based on multi-GNSS, satellite altimetry, Formosat-3/COSMIC data and DORIS data has been studied (Chen et al., 2017; Yao et al., 2018).

Indeed, multi-GNSS can contribute to a considerably denser distribution of Ionospheric Pierce Points (IPPs) and, to certain extent, improve the precision of VTEC products. However, the limited data coverage in the ocean has remained the crucial problem in the VTEC estimation, thus causing low estimation precision in the seas, since most of GNSS stations are located in land. GNSS data collected in moving ships or vessels could palliate this lack of coverage. If the possible technical issues brought by adding this data can be addressed, the problem of sparsity of IPPs' distribution in the ocean will be significantly improved and the performance of GIM products will be further enhanced. Moreover, measurements from LEO satellites, including DORIS and LEO POD data sensitive to the ionospheric delay below and above their respective orbits, can also be made use of to increase the coverage and the accuracy in the generation of GIM VTEC products. The reason why the role of DORIS and POD data has been underrated is that systematic errors would be introduced when single layer ionospheric model is adopted, since the LOS path of them does not cover the whole part of ionosphere. But if tomographic models with multiple layers are taken into account, like the one used in UPC TOMION software (see for instance Hernández-Pajares et al. (1997)), the impact caused by systematic errors mentioned above would not be an issue anymore. On the other hand, it will provide more data illuminated in the voxels with diverse geometry and can help to reconstruct the vertical structure of ionosphere in more details. Another benefit is that it might lead to more accurate electron density fraction estimation and then improve the Barcelona Ionospheric Mapping Function (BIMF) (Lyu et al., 2018b).

This paper presents the impact by adding different combinations of dual-frequency measurements from different Space Geodetic techniques and with different transmitter-receiver line-of-sight geometries, on the GIM VTEC estimation based on a carrier phase data-based tomographic model. Sect. 5.2 describes different types and frequencies of carrier phase measurements used in this work. The validation methods are given in Sect. 5.3. Following that, separate impact by adding each measurement is analyzed in Sect. 5.4 and the performance of all the GIMs which have been considered, compared to external JASON3 VTEC, is assessed in Sect. 5.5. And Sect. 5.6 makes a summary.

5.2 Different types of input dual-frequency carrier phase measurements

The four additional types of measurements respectively from Galileo, LEO POD, DORIS and moving vessel, together with the GPS data, are used to generate the GIM VTEC products in this experiment. In this section, the main features of each type of measurement can be compared in Table 5.1, which will be briefly described in the next subsections.

5.2.1 Galileo

Galileo Navigation Satellite System is compatible and interoperable with GPS. The inclination of the orbit planes is 56 deg. Terrestrial reference frames and reference time systems of Galileo and GPS are aligned, simplifying the combination of measurements from both systems.

5.2.2 LEO POD

On the date with full availability of the different datasets on DOY 155, 2017, four LEO satellites are included, namely Sentinel-3, SWARM-A, -B and -C, the spatial distribution of which can be seen in Figure 5.4. The orbit heights of these four LEOs are around 800 km, 460 km, 530 km and 460 km, respectively. The electron content above the fixed effective height, e.g. 450 km adopted in IGS, is non-negligible, in particular during local night. Thus the GNSS POD data is able to provide valuable information for tomographic model in this work.

5.2.3 DORIS

DORIS dual-frequency measurements, at 2036.25 MHz (S1) and 401.25 MHz (U2), from the 51 ground transmitters to the 5 available LEO-on-board receivers, LEOs Cryosat-2 (CS2), JASON-3 (JA3), HY-2A (H2A), Sentinel-3 (S3A) and Saral (SRL) flying at different orbital heights, has been also considered in this study during the second half of day 4 to the end of day 5 June 2017.

5.2.4 Moving vessel

The University of Hamburg (Germany) operates the F.S. (Forschungsschiffe, research vessel) Maria D. Merian (see Figure 5.1) in various campaigns around the globe. In particular, as

Figure 5.1 F.S. Maria D. Merian, research vessel operated by the University of Hamburg

part of its standard equipment, the vessel features a Trimble SPS461 GPS receiver that is able to deliver raw GNSS measurements (code, phase, Doppler and C/N0) at L1 and L2 frequencies, with 1-Hz data rate. It was working during this study from the second half of day 4 to the end of day 5 June 2017 in the North Atlantic (see the top-right map in Figure 5.10), in order to assess the impact of trying to counterbalance the lack of GNSS receivers in such a region for the GIM generation.

5.3 Validation means

JASON-3 VTEC comparison and dSTEC test assessing the performance on differences between STEC measurements, have been used to externally assess GIMs from different IGS ionospheric analysis centers directly in the ionospheric delay domain (Roma-Dollase et al., 2018). And both are adopted to examine the impact of different combinations on GIM VTEC.

The comparison with direct VTEC measurements from JASON-3 is one direct VTEC external validation method for GIMs, over the oceans, i.e. in worse cases typically far away from the ground GNSS data used to compute the GIM.

Another complementary method is taking the very precise dSTEC data as reference, which is defined as the difference in the given STEC and the STEC at the highest elevation, for each given pair of transmitter and receiver, and for a phase-continuous arc, directly provided by the GNSS receiver measurements with the accuracy of less than 0.1 TECU. In

Table 5.1 Main characteristics of the different type of measurements combined under multi-TOMION, including LEO GPS receivers Sentinel-3 (Sent3), SWARM-A (SWA), -B (SWB) and -C (SWC), and LEO DORIS receivers Cryosat-2 (CS2), HY-2A (H2A), JASON-3 (JA3), Sentinel-3 (S3A) and Saral (SRL). The types of data are S1 (2036.25 MHz) and U2 (401.25 MHz) for DORIS, E1 (1575.42 MHz) and E5a (1176.45 MHz) for Galileo, and L1 (1575.42 MHz) and L2 (1227.60) for GPS, with a typical measurement precision better than 0.1 TECUs. The corresponding number of processed observations, in thousands, are also indicated in the last column.

System		Type		Height		# obs.
	carriers	receiver	transmitter	receiver	transmitter	/1000
GPS	L1,L2	vessel	MEOs	sea-level	20200 km	946
GPS	L1,L2	LEO-Sent3	MEOs	800km	20200 km	305
GPS	L1,L2	LEO-SWA	MEOs	460km	20200 km	317
GPS	L1,L2	LEO-SWB	MEOs	530km	20200 km	320
GPS	L1,L2	LEO-SWC	MEOs	460km	20200 km	317
DORIS	S1,U2	LEO-CS2	stations	725 km	ground	31
DORIS	S1,U2	LEO-H2A	stations	975 km	ground	35
DORIS	S1,U2	LEO-JA3	stations	1345 km	ground	51
DORIS	S1,U2	LEO-S3A	stations	800 km	ground	34
DORIS	S1,U2	LEO-SRL	stations	790 km	ground	33
Galileo	E1,E5a	stations	MEOs	ground	23230 km	2825
GPS	L1,L2	stations	MEOs	ground	20200 km	12368

this case the assessment involves slant observations and over indepedent GNSS stations, i.e. typically not far away from the input GNSS stations used in the GIM estimation.

It has been shown in Hernández-Pajares et al. (2017c) that both assessment techniques are well correlated over receivers placed in islands, when the RMS of the dSTEC discrepancy and the Standard Deviation of the altimeter VTEC difference (quite unaffected by the electron content above the altimeter and below the MEO transmitter) are considered. Due to such characteristics the dSTEC test has been applied in this work over 8 available external GPS receivers, closest to the vessel trajectory, to better detect the impact of its data usage thanks to the higher sensibility of dSTEC test, compared to the altimeter VTEC comparison.

5.4 Separate impact analysis of each measurement

All the GIMs with different combinations of measurements (see last column of Table 5.1) are computed based on the combined tomographic modeling and kriging interpolation, implemented in the TOMIONv1 software (see for instance section 2.4 and references in Roma-Dollase et al. (2018)). In brief, the tomographic part is solved based only on carrier phase data, much more precise than the pseudorange one. And the corresponding phase bias, assumed constant per each phase-continuous transmitter-receiver arc, is estimated as random variable (i.e. parameter) in the Kalman filter. This is done simultaneously to the estimation of the electron density for each illuminated voxel, distributed in two or more shells ("layers"). These unknowns are treated as random walk process, in a Sun-fixed reference frame, in the same Kalman filter. This approach, based on two-layers and ground GPS data only, has been used by UPC since 1998. And the corresponding GIMs have shown in general a slightly better performance than the GIMs of other IGS analysis centers (Roma-Dollase et al., 2018). And, among that, the tomographic-kriging approach of TOMIONv1 allows a straightforward ingestion of ionospheric combinations of dual-frequency carrier phase measurements regardless of any frequencies, GNSS constellations and space geodetic systems. And this is done accurately without the need of estimating any of the many different associated Differential Code Biases (DCB) associated to the pseudorange data, not used in our approach.

5th June 2017 (DOY 156), and the second half of previous day for ensuring Kalman filter initialization, were chosen for this study since the data from polar vessel on that day is available. In this section, the results under different combinations of multi-geometry, multi-GNSS, and multi-Space Geodetic techniques are described in detail.

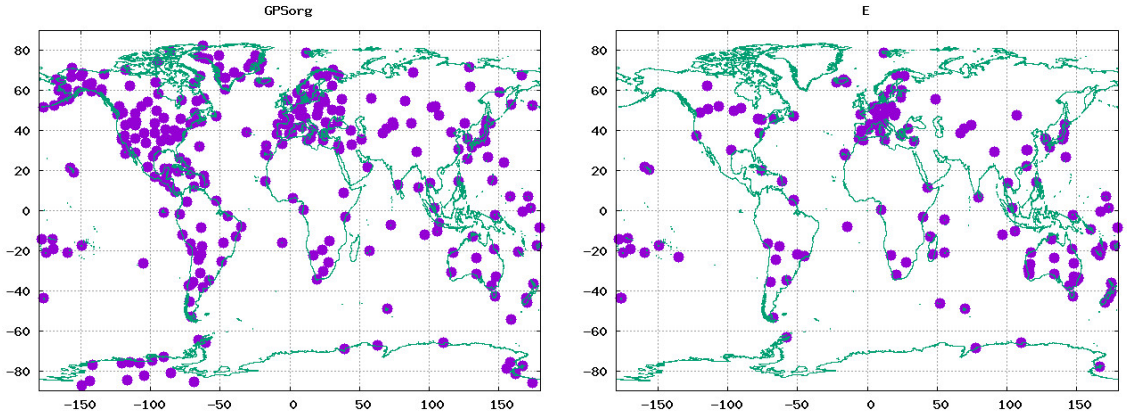

Figure 5.2 Distribution of the original set of GPS receivers (left map), which measurements have processed with the ones of the Galileo receivers distributed in the right map, during 2017 June 4th, 12:00 to June 5th, 24:00.

5.4.1 Impact of adding Galileo data

L1 and L2 dual-frequency measurements of 290 GPS receivers, which are used to compute the GPS-only UQRG GIM, and dual-frequency (E1, E5a) measurements of 164 Galileo receivers, with around 60 of them being collocated, are ingested into TOMION software to compute the combined GPS-Galileo UGEG GIM. The distribution of receivers in each system is shown in Figure 5.2. The improvement attained by adding Galileo measurements is very limited, about 2% in terms of the Standard Deviation (STD) of the GIM versus the independent and direct JASON-3 VTEC measurements over seas: from 2.20 TECU for UQRG to 2.16 TECU for UGEG (see more details in Table 5.2). As for the upper layer electron density estimation, normalized by the VTEC (μ_2 hereafter), the slight benefit of Galileo data, not significantly improving the GPS coverage over the ocean during June 2017 (see Figure 5.2), can be seen in Figure 5.3. These plots correspond to the convergence phase of the filter used to solve the tomographic problem, starting from 12:00, 4th June. The μ_2 values, containing the fractional part of the topside electron content, are slightly more realistic after adding Galileo data with fewer negative values in the local nighttime.

5.4.2 Impact of LEO POD-GPS data

This section examines the impact on ionospheric tomography by using dual-frequency GPS measurements from receivers on-board LEO satellites. Four layers in the tomographic modeling are considered, with boundaries at 110 km, 450 km, 790 km, 1130 km and 1470 km, after splitting by two the original dual layer model to better accommodate the different LEO heights. Three runs have been performed with these four layers:

Table 5.2 Statistics of the difference of JASON3-VTEC minus GIM-VTEC measurements, with GPS+Galileo GIM (UGEG, left-hand part) and GPS-only GIM (UQRG, right-hand part), during June 5th, 2017. Units are in TECU

	VTEC_ALTIMETERobs. – VTEC_GIM								JASON3	
	UGEG				UQRG				VTEC	
	Bias	Sigma	RMS	%ERR	Bias	Sigma	RMS	%ERR		
	-2.30	2.16	3.16	45.6	-2.29	2.20	3.18	45.8	6.93	
UT(hours)	Bias	Sigma	RMS	%ERR	Bias	Sigma	RMS	%ERR	VTEC	#OBS
0.00	-1.34	2.04	2.44	75.2	-1.27	1.84	2.24	69.0	3.24	1902
2.00	-2.86	2.79	4.00	46.4	-2.67	2.58	3.71	43.1	8.61	3377
4.00	-2.17	2.32	3.18	36.0	-1.95	2.29	3.00	34.0	8.83	4125
6.00	-2.68	2.12	3.41	48.9	-2.62	2.19	3.42	48.9	6.98	5360
8.00	-2.91	2.29	3.70	49.8	-3.00	2.37	3.82	51.5	7.43	4263
10.00	-2.32	2.13	3.15	38.6	-2.08	2.30	3.10	38.1	8.16	3008
12.00	-2.28	1.93	2.99	50.5	-2.34	2.23	3.23	54.6	5.92	4040
14.00	-1.46	1.57	2.14	49.3	-1.52	1.58	2.19	50.5	4.35	3340
16.00	-2.48	2.07	3.23	59.9	-2.55	2.15	3.34	61.8	5.40	4204
18.00	-2.55	1.96	3.22	50.8	-2.78	2.06	3.46	54.7	6.34	4566
20.00	-2.15	1.80	2.80	38.5	-2.18	1.90	2.89	39.7	7.27	3440
22.00	-1.97	1.74	2.63	27.1	-1.96	1.77	2.64	27.3	9.69	3886
24.00	-1.85	2.54	3.14	52.0	-1.85	2.33	2.97	49.3	6.03	2943
Lat(deg)	Bias	Sigma	RMS	%ERR	Bias	Sigma	RMS	%ERR	VTEC	#OBS
-60.00	-1.00	1.90	2.14	53.8	-0.92	1.90	2.11	52.8	3.99	10624
-40.00	-1.59	1.98	2.54	51.3	-1.40	1.92	2.38	48.1	4.95	9942
-20.00	-2.75	1.91	3.35	47.4	-2.89	1.94	3.48	49.3	7.05	7407
0.00	-3.60	2.14	4.19	44.5	-3.75	2.12	4.31	45.8	9.42	6553
20.00	-3.18	2.09	3.80	34.2	-3.22	2.03	3.81	34.2	11.13	5890
40.00	-3.04	1.69	3.48	40.5	-3.07	1.73	3.52	41.0	8.59	4983
60.00	-2.37	1.77	2.95	41.2	-2.36	1.80	2.97	41.4	7.16	3055

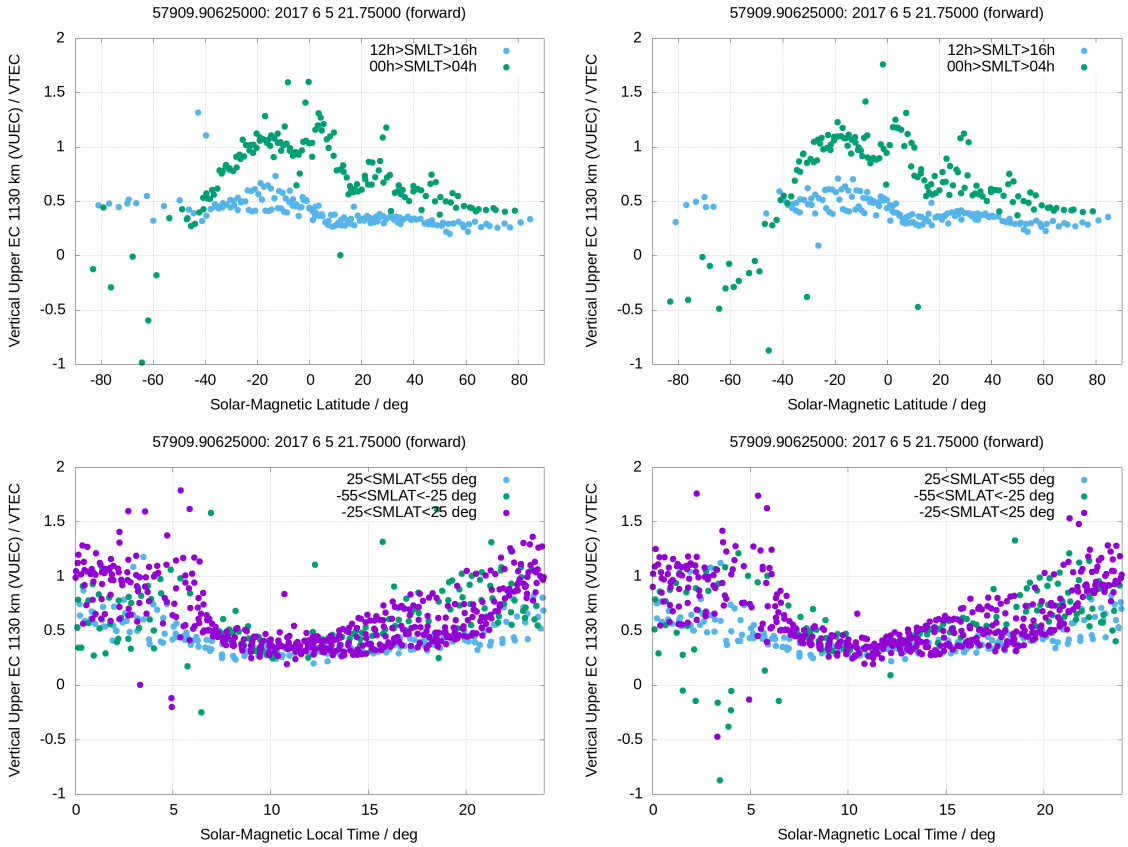

Figure 5.3 Distribution of the upper layer electron density estimation, normalized by the VTEC (the so called shape function assessed at the top layer): from GPS + Galileo measurements (the first column), from GPS measurements (the second column), vs. geomagnetic latitude (the first row) and vs. solar-magnetic local time (the second row). The results correspond to the early phase of the Kalman filter convergence of the global ionospheric tomographic model, at 2017 June 4th, 13:45, within the run from 2017 June 4th, 12:00 to June 5th, 24:00.

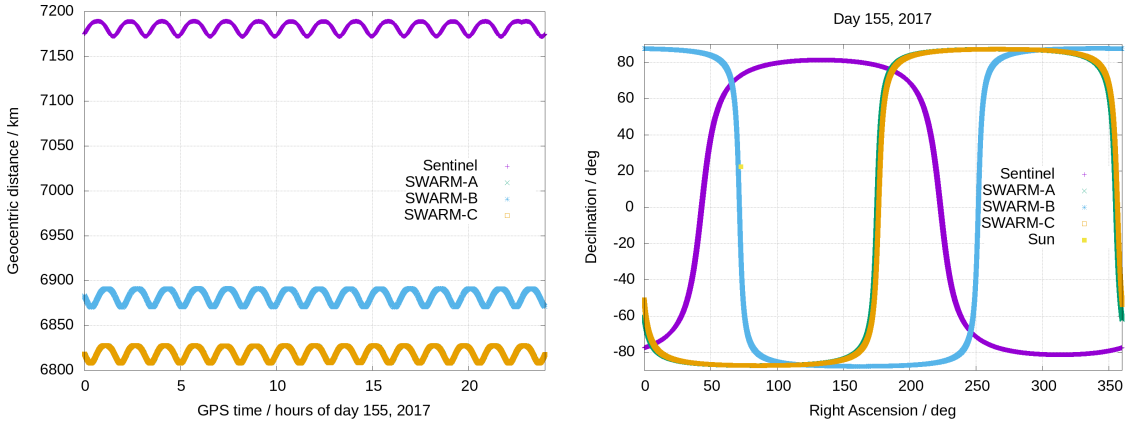

Figure 5.4 Left: Distribution of the heights of LEOs SWARM –A, and –C (magenta and green) and SWARM-B (blue) and Sentinel (yellow) during day 155, 2017. Right: Ground-track of the Sentinel and SWARM LEOs.

- Scenario "G": only ground GPS data.
- Scenario "GL": Ground and LEO GPS data.
- Scenario "L": LEO GPS data only, illuminating only the three top layers (see distribution of LEO heights in Figure 5.4).

The results for the three scenarios are summarized in Figure 5.5 and Figure 5.6: The vertical electron content for the two upper layers, from 790 to 1470 km, is represented vs. latitude for daytime and nighttime, vs. local-time for high-, mid-, and low-latitudes for scenarios G, L and GL. It can be seen the high influence of the topside LEO GPS measurements, decreasing the values given by the ground-only based tomography when the four-layer model is used. This proves that more measurements with different geometries can help improve the estimation accuracy in the tomographic modeling

5.4.3 Impact of adding DORIS data

A first assessment of the impact of adding DORIS dual-frequency measurements, at 2036.25 MHz (S1) and 401.25 MHz (U2), to GPS ground data, on the global two-layer ionospheric tomography, with boundaries at 110, 790 and 1470 km, is summarized in this section. Figure 5.7 shows the distribution of ionopsheric pierce points from 51 ground transmitters to the 5 available LEO-on-board receivers.

From one example of electron content of both layers versus local time (Figure 5.8) and versus latitude (Figure 5.9), it can be seen that both increase in electron content of the second layers and decrease in the first layers are significant, especially at low latitudes and during

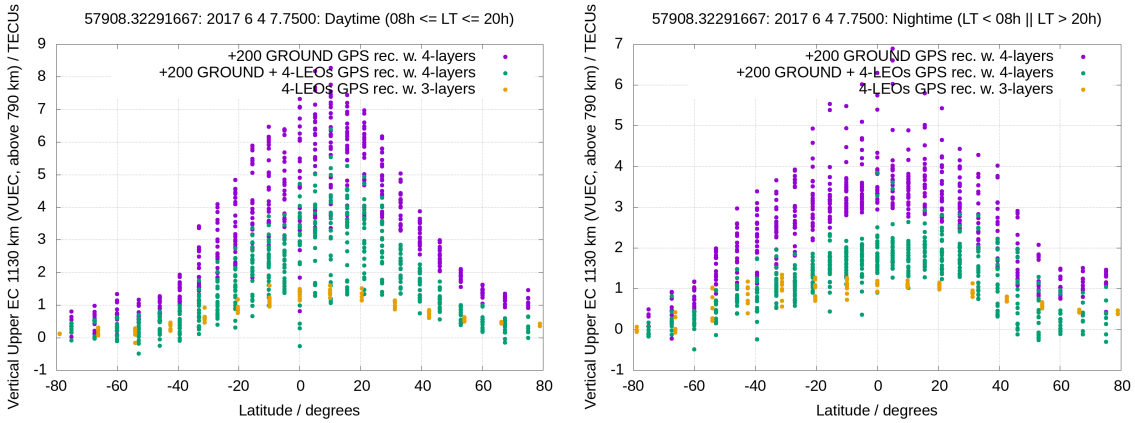

Figure 5.5 Electron content of the two upper layers [790-1470] km vs. latitude for daytime (left) and nighttime (right) for scenarios G (magenta), GL (green) and L (yellow), 07:45 day 155, 2017

the local night (up to 3 TECUs). This change produces a reduction in the certain extent of negative values in the first layers that can be seen again especially during the night at low latitudes. Morever, this effect brought about by merging DORIS to ground-based GPS measurements is consistent with the similar effect observed when LEO POD-GPS data were considered in Sect. 5.4.1 (see Figure 5.6).

Table 5.3 summarizes the assessment of the overall kriging-interpolated VTEC GIMs vs. external JASON-3 VTEC. The bias has changed from -2.29 TECU to -1.78 TECU when DORIS data is incorporated, with a reduction of 0.51 TECU, which is consistent with the results mentioned above. In spite of STD of the difference between JASON-3 VTEC and GIM VTEC being almost equivalent, the relative error RMS is significantly reduced from 45.8% to 41.1% during this day of solar minimum.

5.4.4 Impact of adding vessel data

The combination of dual-frequency GPS measurements taken from a vessel (receiver MAME), with permanent ground receivers has been utilized in order to assess the potential improvement in GIM VTEC over seas. The station distribution map, its zoom map, and the detailed trajectory in the analyzed time are shown in Figure 5.10.

It can be seen in Table 5.4 that the overall VTEC STD remains unchanged, with a certain improvement during the second part of the day, when the filter involving MAME data has converged, and at the ship latitudes, but with certain worsening otherwise.

To better understand the effect of the data combination of the vessel GPS receiver with the global ground-based GPS network, we have applied a second complementary independent

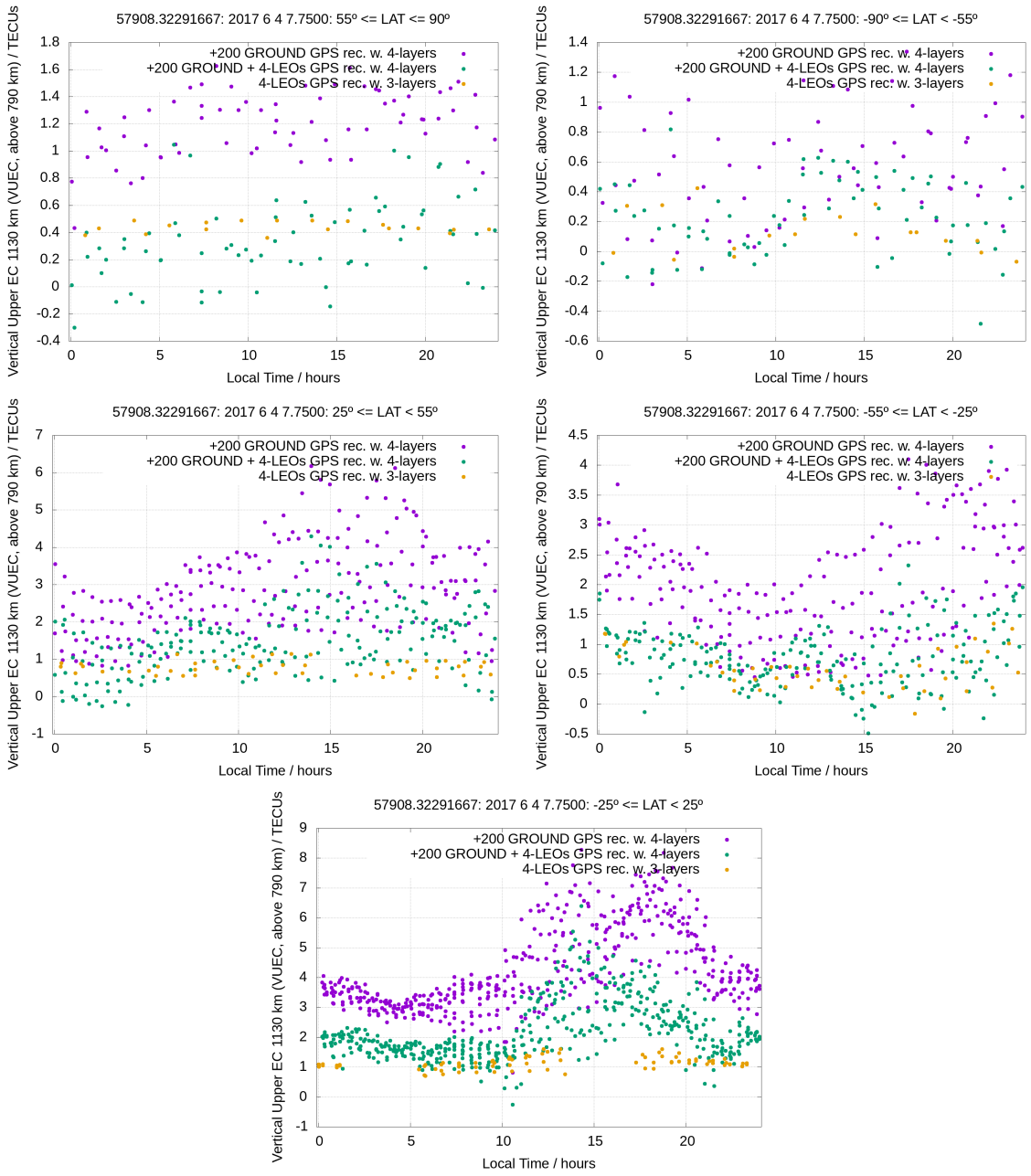

Figure 5.6 Plots similar to the previous ones, but the upper electron content is represented vs. local time, the top for high-latitudes, north and south hemispheres (left- and right-hand plots, respectively); the middle for mid-latitudes, north(left) and south(right) hemispheres; the bottom for low latitudes.

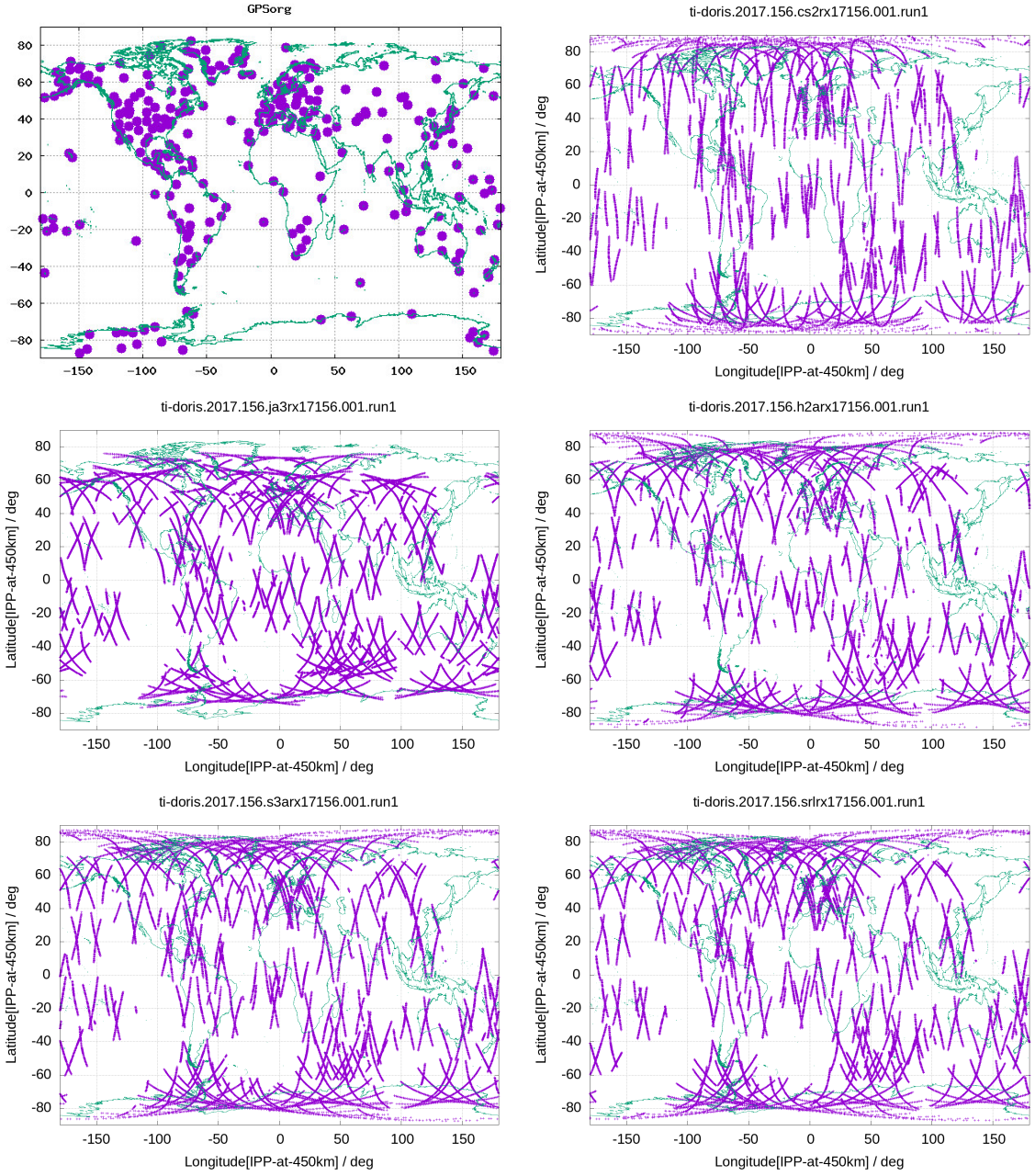

Figure 5.7 The distribution of the set of ground GPS receivers can be seen at top left plot. The distribution of ionospheric pierce points, at 450 km height, for the DORIS LOS observations can be seen in the consecutive plots corresponding, from left to right and from top to bottom, to the LEOs Cryosat-2 (CS2), JASON-3 (JA3), HY-2A (H2A), Sentinel-3 (S3A) and Saral (SRL), everything during June 5, day 156, 2017.

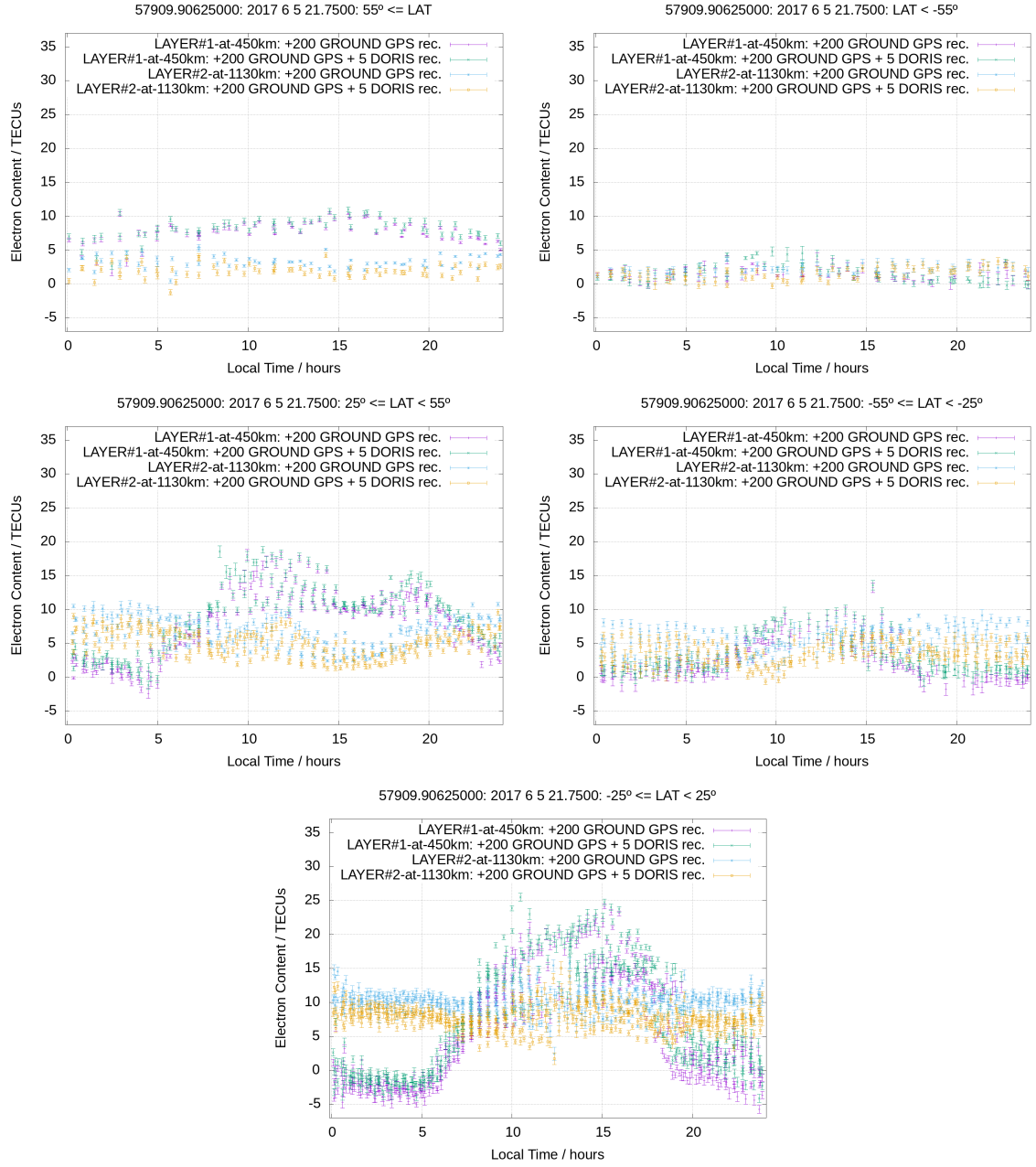

Figure 5.8 Each plot represents versus local time the vertical electron content of the first layer [110-790] km by using ground GPS data only (magenta) and ground GPS and DORIS data (green), and the vertical electron content of the second layer [790-1470] km with GPS data only (blue) and ground GPS and DORIS (yellow). Each plot corresponds to GPS time of 21.75h during June 5th, day 156 of 2017. From top to bottom and from left to right, the plots are for north high-latitudes, south high-latitudes, north mid-latitude, south mid-latitudes and low latitudes, respectively.

Table 5.3 Statistics of the difference of JASON3-VTEC minus GIM-VTEC measurements, with ground-based GPS and DORIS data (UGDG, left-hand part) and GPS ground only (UQRG, right-hand part), during June 5th, day 156 of year 2017

	VTEC_ALTIMETERobs. – VTEC_GIM								JASON3	
	UGDG				UQRG				VTEC	
	Bias	Sigma	RMS	%ERR	Bias	Sigma	RMS	%ERR		
	-1.78	2.22	2.85	41.1	-2.29	2.20	3.18	45.8	6.93	
UT(hours)	Bias	Sigma	RMS	%ERR	Bias	Sigma	RMS	%ERR	VTEC	#OBS
0.00	-0.81	2.22	2.37	73.1	-1.27	1.84	2.24	69.0	3.24	1902
2.00	-2.57	3.04	3.98	46.2	-2.67	2.58	3.71	43.1	8.61	3377
4.00	-1.61	2.21	2.73	30.9	-1.95	2.29	3.00	34.0	8.83	4125
6.00	-2.08	2.05	2.92	41.8	-2.62	2.19	3.42	48.9	6.98	5360
8.00	-2.54	2.40	3.49	47.0	-3.00	2.37	3.82	51.5	7.43	4263
10.00	-1.83	2.10	2.79	34.2	-2.08	2.30	3.10	38.1	8.16	3008
12.00	-1.73	2.00	2.65	44.8	-2.34	2.23	3.23	54.6	5.92	4040
14.00	-0.80	1.67	1.85	42.5	-1.52	1.58	2.19	50.5	4.35	3340
16.00	-1.70	2.20	2.78	51.5	-2.55	2.15	3.34	61.8	5.40	4204
18.00	-2.10	2.07	2.95	46.6	-2.78	2.06	3.46	54.7	6.34	4566
20.00	-1.67	1.70	2.38	32.8	-2.18	1.90	2.89	39.7	7.27	3440
22.00	-1.54	1.78	2.35	24.3	-1.96	1.77	2.64	27.3	9.69	3886
24.00	-1.29	2.57	2.87	47.6	-1.85	2.33	2.97	49.3	6.03	2943
Lat(deg)	Bias	Sigma	RMS	%ERR	Bias	Sigma	RMS	%ERR	VTEC	#OBS
-60.00	-0.51	1.92	1.98	49.7	-0.92	1.90	2.11	52.8	3.99	10624
-40.00	-0.94	2.08	2.28	46.1	-1.40	1.92	2.38	48.1	4.95	9942
-20.00	-2.29	2.00	3.04	43.1	-2.89	1.94	3.48	49.3	7.05	7407
0.00	-3.31	2.21	3.98	42.2	-3.75	2.12	4.31	45.8	9.42	6553
20.00	-2.65	2.08	3.37	30.2	-3.22	2.03	3.81	34.2	11.13	5890
40.00	-2.31	1.70	2.87	33.4	-3.07	1.73	3.52	41.0	8.59	4983
60.00	-1.86	1.76	2.56	35.7	-2.36	1.80	2.97	41.4	7.16	3055

Table 5.4 Statistics of the difference of JASON3-VTEC minus GIM-VTEC measurements, with ground+vessel receivers (UGS1, left-hand part) and GPS ground only (UQRG, right-hand part), during June 5th, day 156 of year 2017

	VTEC_ALTIMETERobs. – VTEC_GIM								JASON3	
	USG1				UQRG				VTEC	
	Bias	Sigma	RMS	%ERR	Bias	Sigma	RMS	%ERR		
	-2.44	2.20	3.28	47.4	-2.29	2.20	3.18	45.8	6.93	
UT(hours)	Bias	Sigma	RMS	%ERR	Bias	Sigma	RMS	%ERR	VTEC	#OBS
0.00	-1.67	2.03	2.63	81.3	-1.27	1.84	2.24	69.0	3.24	1902
2.00	-3.02	2.82	4.13	48.0	-2.67	2.58	3.71	43.1	8.61	3377
4.00	-2.16	2.33	3.17	35.9	-1.95	2.29	3.00	34.0	8.83	4125
6.00	-2.84	2.25	3.62	51.8	-2.62	2.19	3.42	48.9	6.98	5360
8.00	-2.98	2.49	3.89	52.3	-3.00	2.37	3.82	51.5	7.43	4263
10.00	-2.57	2.33	3.47	42.5	-2.08	2.30	3.10	38.1	8.16	3008
12.00	-2.24	1.94	2.97	50.1	-2.34	2.23	3.23	54.6	5.92	4040
14.00	-1.69	1.57	2.31	53.1	-1.52	1.58	2.19	50.5	4.35	3340
16.00	-2.61	2.03	3.31	61.3	-2.55	2.15	3.34	61.8	5.40	4204
18.00	-2.83	1.98	3.46	54.6	-2.78	2.06	3.46	54.7	6.34	4566
20.00	-2.40	1.86	3.04	41.8	-2.18	1.90	2.89	39.7	7.27	3440
22.00	-2.08	1.74	2.71	28.0	-1.96	1.77	2.64	27.3	9.69	3886
24.00	-1.79	2.32	2.93	48.6	-1.85	2.33	2.97	49.3	6.03	2943
Lat(deg)	Bias	Sigma	RMS	%ERR	Bias	Sigma	RMS	%ERR	VTEC	#OBS
-60.00	-1.01	1.90	2.15	53.8	-0.92	1.90	2.11	52.8	3.99	10624
-40.00	-1.69	1.95	2.59	52.3	-1.40	1.92	2.38	48.1	4.95	9942
-20.00	-2.92	1.78	3.42	48.5	-2.89	1.94	3.48	49.3	7.05	7407
0.00	-3.92	2.17	4.48	47.6	-3.75	2.12	4.31	45.8	9.42	6553
20.00	-3.49	2.18	4.12	37.0	-3.22	2.03	3.81	34.2	11.13	5890
40.00	-3.08	1.72	3.53	41.1	-3.07	1.73	3.52	41.0	8.59	4983
60.00	-2.39	1.76	2.97	41.5	-2.36	1.80	2.97	41.4	7.16	3055

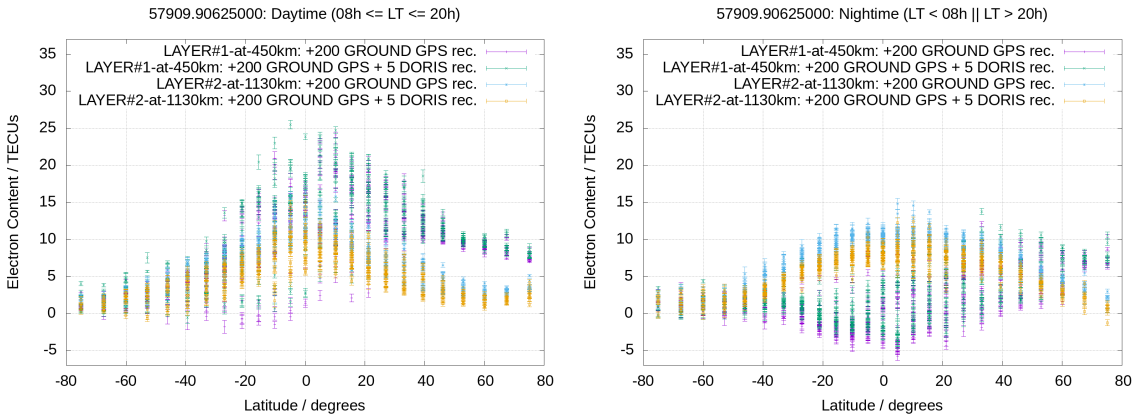

Figure 5.9 Plots similar to previous figure but for approximately local daytime between 08h and 20h (left) and local nighttime before 08h and after 20h (right) at 21.75h on June 5th, day 156 of 2017.

assessment, the dSTEC based on STEC measurements from GPS receivers not used in the VTEC GIM computation (see Hernández-Pajares et al. (2017c)). The eight closest available independent receivers shown in the zoom map of Figure 5.10 have been considered. They are divided into two groups: group A includes two GPS receivers in Ireland - ENIS and FOYL, and NEWL in England, without any permanent receiver between them and the vessel receiver's trajectory; and group B contains GPS receivers ACOR, GAIA, LEON, SALA and VIGO at Iberian Peninsula, surrounded by ground receivers used in the GIM computation. It can be seen in Figure 5.11 and in Table 5.6 that the dSTEC performance improves around 6-10% in the most isolated locations (receivers in group A), but it decreases 10-15% in the locations in group B, whic are close to receivers contributing to the VTEC GIMs. This result is consistent with the processing rate of the vessel receiver measurements (1 second) compared with the downdated global ground-based measurements (reduced to 900 seconds), which can produce a less influence on the GIM in the area of the permanent ground receivers in group B.

5.5 Performance of different GIMs vs. JASON3 VTEC

In order to provide an overall summary of the performance vs. external JASON3 VTEC of different VTEC GIMs obtained by the above mentioned combinations of ground GPS, LEO-POD GPS, DORIS and ground Galileo, including Galileo-only, we have firstly tuned the smoothing of the JASON3 VTEC measurements.

In order to increase the "contrast" of the assessment vs. altimeter VTEC in the present minimum of the Solar Cycle, an updated sliding window of 25 altimeter samples (instead

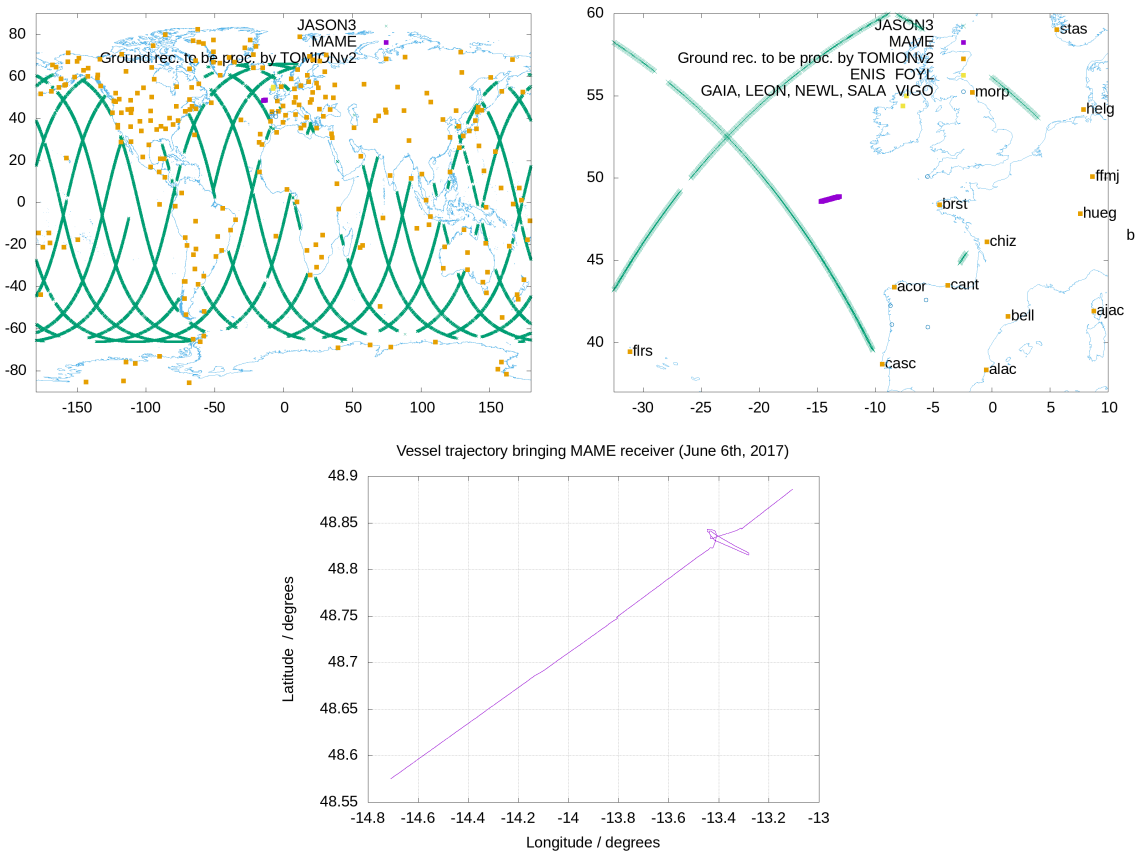

Figure 5.10 Map and zoom of global network of permanent GPS receivers on land (top), used to compute the VTEC GIM UQRG (yellow), vessel-on-board receiver MAME (magenta), track of JASON-3 altimeter (green) and additional external receivers, i.e. not involved in the GIM computation, to assess it (brown circles and light-blue squares). The vessel trajectory, computed by TOMION with PPP each 30 seconds and linearly interpolated at 1Hz, is shown at the bottom (June 5th, day 156, 2017).

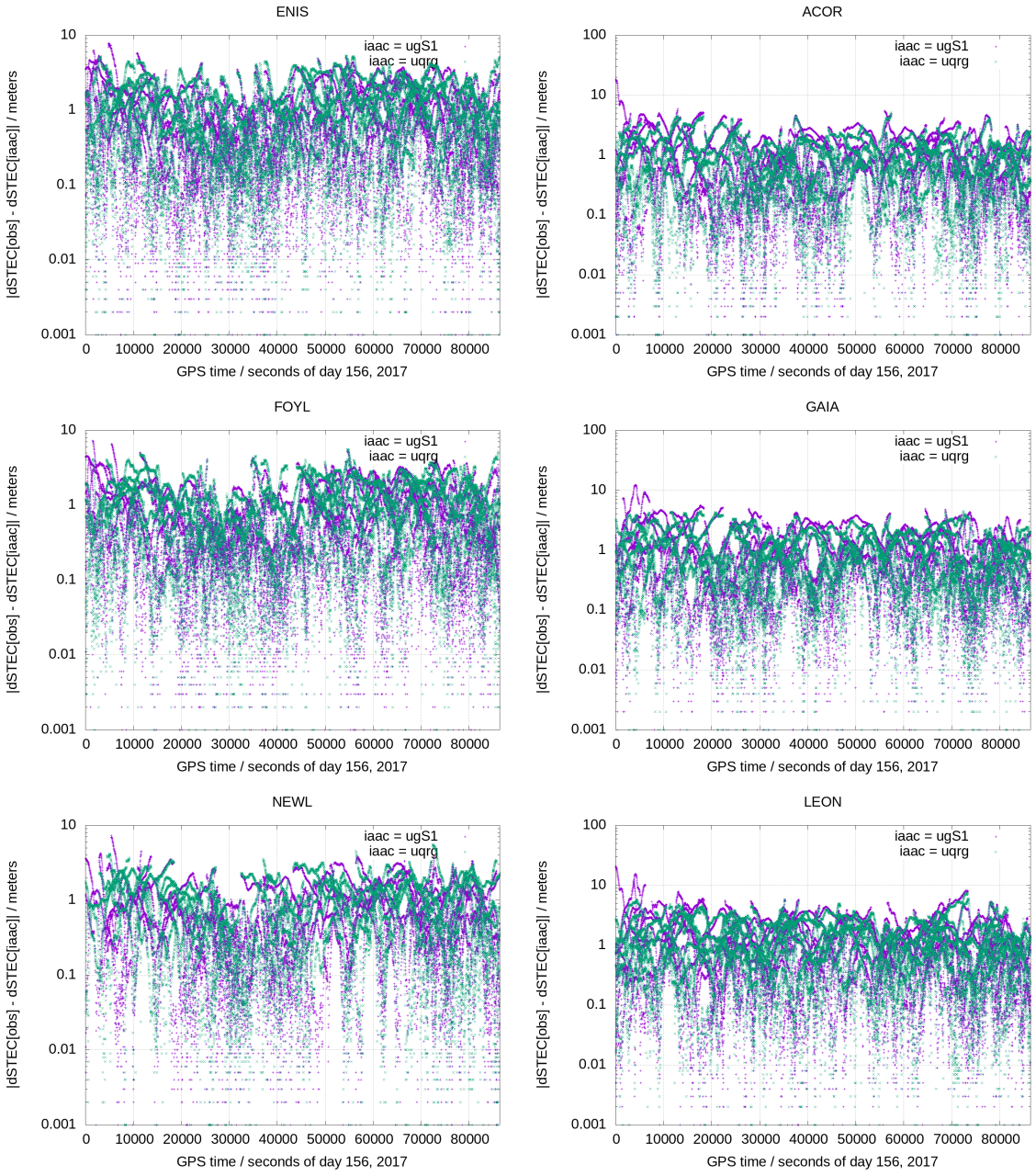

Figure 5.11 Semilog plots representing the absolute value of the dSTEC error using the +200 GPS receivers and the vessel-onboard MAME receiver (UGS1, magenta points) and only the permanent GPS receivers (UQRG, green points), for external GPS receivers in Ireland and England (first column), and three receivers in Spain and Portugal (second column), during June 5th, day 156 of year 2017.

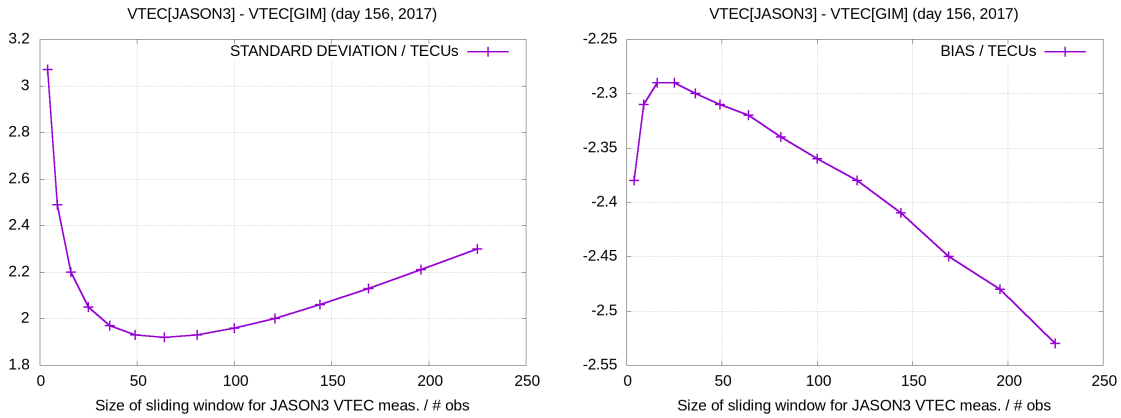

Figure 5.12 Standard deviation (left) and bias (right) of VTEC_JASON3 – VTEC_UQRG, in TECU, vs. the number of samples of the smoothing sliding window for JASON3 measurements.

of the initial value of 16), to smooth the reference measurements, has been selected for this overall comparison.

It can be seen in Figure 5.12 that this window length significantly reduces the STD of the best behaving UPC GIM (UQRG) regarding JASON-3 VTEC, minimizing the bias.

In Table 5.5 it can be seen that the GIM combining ground-GPS + LEO-POD GPS + DORIS (ugDP) significantly increase the accuracy regarding to the ground-GPS GIM (uqrg): reduction of 3% in Standard Deviation coinciding with a reduction to less than the half of bias, a reduction of more than 1 TECU. Another remarkable result is for the GIM combining ground Galileo + GPS, which increases the GIM performance about 1.5% in Standard Deviation.

In short, one of the main results of the overall study as detailed in the tomographic results, the reduction in the top layer estimation consistently obtained from independent usage of DORIS and LEO-POD GPS measurements, is confirmed as well with the VTEC assessment vs. JASON-3.

5.6 Summary

In this work we introduce a new way of improving the sligthly best performing GIM within IGS, the UQRG produced by UPC-IonSAT with the TOMION dual-layer voxel model solved with ground-based dual-frequency carrier phase GPS data combined with kriging interpolation. This is done by increasing its vertical resolution consistently with the heights of the now involved GNSS and DORIS LEO receivers. This has allowed the synergestic combination of vessel-, LEO- and ground-based measurements, providing an increase of the

Table 5.5 Statistics of VTEC_JASON3-VTEC_GIM during June 5th, day 156, 2017 for different GIMs computed and compared in this study: ground-Galileo only (UE__), ground-GPS 5min-updated-filter (ug5m), ground-GPS and Doppler (ugD_), ground-GPS, Doppler and LEO-POD GPS (ugDP), ground-GPS and ground-Galileo (ugEG), ground-GPS and GPS-on-board-vessel at NA 1Hz (ugS1), ground-GPS (uqrg), among the IGS final combined (igsg) and IGS final individual GIMs (casg, codg, emrg, esag, jplg, upcg). The 47664 JASON-3 VTEC measurements present a daily average of 6.92 TECU.

IONEX ID	Bias	St.Dev. TECU	RMS	Rel.Err. %
casg	-1.04	2.41	2.62	37.9
codg	-1.20	2.37	2.65	38.3
emrg	-1.59	2.37	2.86	41.2
esag	-1.82	2.58	3.16	45.6
igsg	-2.28	2.43	3.33	48.0
jplg	-3.75	2.65	4.59	66.4
uE__	-1.76	2.10	2.74	39.6
ug5m	-1.88	2.12	2.84	41.0
ugDg	-1.78	2.09	2.74	39.6
ugDP	-1.09	1.99	2.27	32.7
ugEG	-2.30	2.02	3.06	44.2
ugS1	-2.44	2.05	3.19	46.0
upcg	-2.34	2.14	3.17	45.8
uqrg	-2.29	2.05	3.08	44.5

VTEC accuracy at global scale in large regions with sparse GPS ground-based data. The performance of the new resulting multiTOMION model is illustrated with a first application to one of the infrequent datasets, including the whole day of June 5th 2017, with all the involved input data collocated, in particular the vessel-based GNSS ones. The results show in particular: (1) an overall GIM improvement of 3% in standard deviation vs. independent JASON-3 VTEC measurements when LEO- and ground- based GPS data are combined with DORIS measurements. And (2) a local improvement of 6-9% in performance vs. observed differences of STEC (dSTEC) from independent GPS receivers placed at several hundreds of km far from the vessel.

Table 5.6 Statistics of the difference of dSTEC directly measured by independent GPS receivers (first column) minus the value provided by the corresponding VTEC GIMs, with ground+vessel receivers (UGS1, left part) and ground only (UQRG, right-hand part), after the tomographic convergence time, from 03:00 to 24:00, DOY 156, 2017.

receiver ID	dSTEC_GPSobs - dSTEC_GIM								#Obs
	UGS1				UQRG				
	Bias	Std.Dev.	RMS	Rel.Err.	Bias	Std.Dev.	RMS	Rel.Err.	
	TECU			%	TECU			%	
ENIS	-0.1	1.2	1.2	15.3	0.1	1.3	1.4	16.5	24534
FOYL	-0.0	1.1	1.1	14.4	0.1	1.2	1.2	15.9	22752
NEWL	-0.2	1.0	1.0	15.3	-0.1	1.1	1.1	16.3	18625
ACOR	-0.4	1.2	1.3	15.8	-0.3	1.1	1.1	13.5	20207
GAIA	-0.5	1.3	1.4	16.3	-0.4	1.1	1.2	14.0	21539
LEON	-0.3	1.7	1.7	15.8	-0.2	1.5	1.5	14.2	24782
SALA	-0.5	1.5	1.6	13.3	-0.3	1.3	1.3	11.1	25039
VIGO	-0.5	1.4	1.5	14.1	-0.4	1.2	1.3	11.9	24091

Chapter 6

Quality Indexes

This chapter is aimed at providing evidence of the quality of the research developed in the context of the Ph.D. study. The work supporting this thesis has been presented to a number of international conferences and peer-reviewed journals, where experts have provided valuable comments that have improved the quality and clarity of the research. The list of papers and presentations can be found in the following sections.

6.1 Peer-reviewed Journals

- Lyu, H., Hernández-Pajares, M., Nohutcu, M., García-Rigo, A., Zhang, H., and Liu, J. (2018b). The barcelona ionospheric mapping function (bimf) and its application to northern mid-latitudes. *GPS solutions*, 22(3):67(8 citations following google scholar)

- Lyu, H., Hernández-Pajares, M., Monte-Moreno, E., and Cardellach, E. (2019a). Electron density retrieval from truncated radio occultation gnss data. *Journal of Geophysical Research: Space Physics*, 124(6):4842–4851(1 citation following google scholar)

- Hernández-Pajares, M., Lyu, H., Aragón-Àngel, À., Monte-Moreno, E., Liu, J., An, J., and Jiang, H. (2020a). Polar electron content from gps data-based global ionospheric maps: Assessment, case studies, and climatology. *Journal of Geophysical Research: Space Physics*, 125(6):e2019JA027677

- Hernández-Pajares, M., Lyu, H., Garcia-Fernandez, M., and Orus-Perez, R. (2020b). A new way of improving global ionospheric maps by ionospheric tomography: consistent combination of multi-gnss and multi-space geodetic dual-frequency measurements gathered from vessel-, leo- and ground-based receivers. *Journal of Geodesy*, 94(8):1–16

The importance of each journal where the research has been published is proven in Table 6.1, by means of presenting the latest Impact Factor (IF) and quartile available at the time of writing this dissertation, according to Thomson Reuters. As we can see, all the previous listed journals are in the first quartile.

Journal	ISSN	Quartile	Impact Factor	5 year Impact Factor
GPS Solut	1080-5370	Q1	3.049	3.924
JGR: Space Physics	2169-9402	Q1	2.733	2.49
Journal of Geodesy	0949-7714	Q1	4.806	5.280

Table 6.1 Journal information and ranking in its category based on the IF.

6.2 Presentations at International Conferences

- Lyu, H., Hernández-Pajares, M., Aragón-Àngel, A., Monte Moreno, E., Liu, J., An, J., and Jiang, H. (2020). Polar electron content features shown in UQRG GIMs and climatology study by Learning Vector Quantization. In *GNSS Research and Application for Polar Environment (GRAPE)/RESOURCE Online Workshop*, pages 1–23, Online

- Lyu, H., Hernández-Pajares, M., Monte-Moreno, E., and Cardellach, E. (2019b). Two methods of electron density retrieval from truncated ionospheric radio occultation data. In *EUMETSAT ROM SAF - IROWG2019*, pages 1–45, Copenhagen

- Lyu, H., Hernández-Pajares, M., Monte-Moreno, E., B., N., and Cardellach, E. (2018a). A hybrid of Abel inversion and Vary-Chap model to reconstruct RO electron density profile. In *International GNSS Service Workshop*, pages 1–1, Wuhan

- Lyu, H., Hernández-Pajares, M., Nohutcu, M., and Garcia-Rigo, A. (2017b). The new Barcelona Ionospheric Mapping Function (BIMF). In *International Colloquium on Scientific and Fundamental Aspects of GNSS / Galileo*, pages 1–26, Valencia

- Lyu, H., Hernández-Pajares, M., and Monte-Moreno, E. (2017a). Derivation and applicability of 3D electron content and decorrelation lengths obtained from ground- and LEO-based GNSS models. In *URSI General Assembly and Scientific Symposium*, pages 1–46, Montreal

- Lyu, H., Hernández-Pajares, M., Nohutcu, M., and Garcia-Rigo, A. (2017c). The New Barcelona Ionospheric Mapping Function for North Mid Latitude GNSS applications. In *International GNSS Service Workshop*, pages 1–1, Paris

- García-Rigo, A., Roma-Dollase, D., Hernández-Pajares, M., Lyu, H., Li, Z., Wang, N., Terkildsen, M., Olivares, G., Ghoddousi-Fard, R., Dettmering, D., Erdogan, E., Haralambous, H., Beniguel, Y., Berdermann, J., Kriegel, M., Krypiak-Gregorczyk, A., Gulyaeva, T., Fuller-Rowell, T., Altadill, D., Blanch Llosa, E., Bergeot, N., Chevalier, J., Krankowski, A., Agrotis, L., Galkin, I., Orús, R., and Prol, F. (2017). Contributions to real time and near real time ionosphere monitoring by IAG's RTIM-WG. In *Joint Scientific Assembly of the International Association of Geodesy and International Association of Seismology and Physics of the Earth's Interior*

- Hernández-Pajares, M., Lyu, H., Nohutcu, M., Garcia-Rigo, A., Zhang, H., and Liu, J. (2017b). New ionospheric mapping function (BIM) and other recent contributions to GNSS ionospheric sounding involving UPC-IonSAT. In *Specialized Summit on Space Geodesy and Ionosphere Research*, pages 1–28, Berlin

- Hernández-Pajares, M., Lyu, H., Monte Moreno, E., Yang, H., dos Santos Prol, F., Roma Dollase, D., and García-Rigo, A. (2018b). Recent results on ionospheric modeling with UPC-IonSAT contributions. In *Specialized Summit on Space Geodesy and Ionosphere Research*, pages 1–33, Berlin

- Hernández-Pajares, M., Lyu, H., An, J., Jiang, H., and Aragón-Àngel, A. (2018a). Time evolution of vertical electron content distribution in polar ionosphere from UPC-GIM TOMION runs. In *International GNSS Service Workshop*, pages 1–1, Wuhan

- Hernández-Pajares, M., Lyu, H., Yang, H., Monte Moreno, E., Aragón-Àngel, A., and Cardellach, E. (2019b). Recent contributions to GNSS Ionospheric modelling: Truncated Radio-Occultations, multi-TID tsunami signatures and GIMs information on Polar Ionosphere. In *Specialized Summit on Space Geodesy and Ionosphere Research*, pages 1–58, Berlin

- Hernández-Pajares, M., Roma-Dollase, D., García-Rigo, A., Monte-Moreno, E., Yang, H., Lyu, H., dos Santos Prol, F., Themens, D., Garcia-Fernandez, M., Orus-Perez, R., Li, Z., Wang, N., Yuan, Y., Laurichesse, D., and Blot, A. (2019d). Recent UPC-IonSAT results on global RT and other ionospheric modelling problems. In *The 10th China Satellite Navigation Conference (CSNC 2019)*, pages 1–29, Beijing

- Hernández-Pajares, M., Lyu, H., Aragón-Àngel, A., Monte Moreno, E., Liu, J., An, J., and Jiang, H. (2019a). The Polar Ionosphere seen through Global Ionospheric Maps. In *The 20th International Beacon Satellite Symposium*, pages 1–20, Olsztyn

- Hernández-Pajares, M., Olivares-Pulido, G., Aragón-Àngel, A., dos Santos Prol, F., Lyu, H., Monte Moreno, E., E., C., Garcia-Fernàndez, M., A., R., R., N., von Engelni, A., R. Themens, D., García-Rigo, A., de Oliveira Camargoi, P., and Tadeu de Assis Honorato Muella, M. (2019c). Recent progress in Linear Vary-Chapman (LVC) modelling of the electron density. In *The International Workshop on GNSS Ionosphere*, pages 1–37, Neustrelitz

Chapter 7

Conclusions

The present chapter brings together the conclusions achieved in this dissertation. In addition, future research work in progress are explained.

7.1 Conclusions

The first contribution shown in Chapter 2 is to propose a new ionospheric mapping function concept - Barcelona Ionospheric Mapping Function (BIMF) and its first implementation in the northern mid-latitudes (BIMF-nml), aiming to improve the accuracy of conversion from VTEC to STEC for GNSS users. As one of the IGS Ionosphere Associate Analysis Centers, UPC has performed the daily run of dual-layer tomographic calculation since 1998. The byproduct is the vertical electron content fraction of the second layer - μ_2, which is the key parameter of BIMF. BIMF-nml, for the latitude range from 30°N to 60°N, is climatologically defined, based on the μ_2 database during one solar cycle from 1998.4 to 2009.4. After analyzing the variation characteristics of μ_2, we modeled its variation for northern mid-latitudes as a function depending on the days during one solar cycle and local time. For GNSS users, BIMF is simple to apply for STEC computation by saving the coefficients of this climatic μ_2 model as constants. In terms of model assessment, the GIMs from different IGS IAACs are used to obtain the VTEC values, and precise dSTEC measurements are chosen as evaluation criteria. Only the IGS stations not used for the generation of GIMs are selected to test the performance of BIMF-nml. The statistical results of dSTEC daily RMS error in 2014 show that BIMF performs better than the standard mapping function in most cases for all mid geomagnetic latitudes, with VTEC GIMs computed with different models by different analysis centers, not only for UPC but also for CODE and JPL, with even better improvements compared to UPC GIMs.

The second contribution shown in Chapter 3 is to demonstrate that the UQRG GIMs, computed by UPC-IonSAT since 1998, are able to provide the main VTEC climatology in both polar ionospheres in a realistic way. This statement is supported by two following points: firstly, UQRG is the slightly most accurate GIM among IGS centers, globally as well as in polar regions, by comparing it and different final IGS GIMs with direct VTEC measurements of altimeters available from 2002 to 2018; secondly, UQRG GIMs are able to show the VTEC footprint of different polar ionosphere phenomena, through six case studies, i.e. Tongue of Ionization, trough and dawn-side drifting structure, flux transfer event, *Theta-aurora*, ionospheric convection patterns and storm enhanced density during infrequent major geomagnetic storms. All of them are in agreement with the results reported by other authors, with different techniques and sources of measurement. The interpretation for some of these phenomena is supported as well by the topside electron content fraction μ_2. The unsupervised clustering results of normalized VTEC distribution from 2001 to the beginning of 2019 show that TOI and polar cap patches exhibit an annual dependence, i.e. occurring in the North Hemisphere winter and the South Hemisphere summer.

The third contribution summarized in Chapter 4 is to propose a new Abel-VaryChap Hybrid method, called AVHIRO, to retrieve the electron density profiles from topside truncated radio-occultation data, e.g. data in future EPS-SG satellites. AVHIRO method solves the full electron densities, ambiguity term, and four parameters of the Linear Vary-Chap model simultaneously, taking into account the nonlinear interactions between the unknown parameters, with the help of Powell searching, instead of using the conventional methods based on gradient search. One advantage of AVHIRO method is not depending on any external model or data beyond RO measurements. After applying AVHIRO, both bias and standard deviation of estimated electron densities have been decreased significantly compared to the values before applying AVHIRO. It can considered as a good postprocessing technique for electron density estimation from truncated RO data.

The fourth and last contribution shown in Chapter 5 has been focused on the impact of combining different sources of dual-frequency space geodetic measurements in the estimation of global ionospheric electron content maps thanks to the opportunity of collocated availability of such diverse sources of data. DORIS, ground-based Galileo, ground-based, LEO-POD and vessel-based GPS, have been combined in a Kalman-filtered global dual-layer voxel model, which outputs Kriging-filtered VTEC, during the target day 156 (June 5th), 2017. The resulting GIMs are assessed versus external JASON-3 VTEC and GPS dSTEC observations. From the above analysis, GIM VTEC estimation is improved by combining multi-system carrier phase measurements gathered under different geometries in a multi-layer tomographic model. The most obvious change is the reduction in the top layer estimation,

which is consistent with the result obtained from independent usage of DORIS and LEO-POD GPS measurements. This is also confirmed with the VTEC assessment versus JASON-3, with reduction up to 3% in standard deviation and with reduction of up to less than half of bias (+1 TECU). Moreover, local improvements of 6-9% in dSTEC performance can be obtained by incorporating dual-frequency GNSS measurements from vessels, which are important because they offer an invaluable data source in areas with lack of GNSS data under normal conditions. In this regard, it might be convenient that data generators and curators (like CDDIS and EUREF) could centralize the data into a common future repository so that analysis centers would then have the opportunity to use this data in order to reprocess their products. Additionally, further improvement in the user retrieval of slant delay from GIMs can be achieved by extending the recently introduced Barcelona Ionospheric Mapping Function concept to a global scale from the given tomography.

7.2 Future work

BIMF-nml has proved the potential application prospect of BIMF for northern mid-latitudes, and the new mapping function will be optimized and generalized for different latitudinal ranges in the future. We also plan to generalize BIMF on a global scale and extend the type of validation to the positioning domain.

Parallel processing to speed up the AVHIRO estimation will be implemented to meet the requirement of near real time application.

The analyzed data will be extended from the end of 1996 to 2019 for the climatology study of polar ionosphere phenomena. Based on the unsupervised clustering results, a new climatic model of both polar ionospheres will be investigated.

The mutliTOMION model used in Chapter 5 will be further developed to ingest Beidou and GLONASS data. In the future, when all the data can be accessed, including GPS and multi-GNSS data gathered from globally distributed vessels, ground stations, and LEO satellites, as well as DORIS data, more studies will be triggered on the extensive application of this multiTOMION model.

Chapter 8

Publications

The present chapters includes a copy of the articles published in peer-reviewed journals realized in the context of the Ph.D. study.

ATTENTION¡¡

Pages 104 to 166 of the thesis, which contain the following 4 articles, are available on the website of the respective publisher

1 Lyu. X. [et al.]. The Barcelona ionospheric mapping function (BIMF) and its application to northern mid-latitudes. "Gps solutions", 26 April 2018.

https://link.springer.com/article/10.1007%2Fs10291-018-0731-0

2 Lyu, H. [et al.]. Electron density retrieval from truncated Radio Occultation GNSS data. "Journal of geophysical research: space physics", 1 Juny 2019, vol. 124, núm. 6, p. 4842-4851.

https://agupubs.onlinelibrary.wiley.com/doi/abs/10.1029/2019JA026744

3 Hernández-Pajares, M. [et al.]. Polar Electron Content From GPS Data-Based Global Ionospheric Maps: Assessment, Case Studies, and Climatology. "Journal of geophysical research: space physics", 1 June 2020, vol. 125, num. 6, e2019JA027677

https://agupubs.onlinelibrary.wiley.com/doi/abs/10.1029/2019JA027677

4 Hernández-Pajares, M. [et al.]. A new way of improving global ionospheric maps by ionospheric tomography: consistent combination of multi-GNSS andmulti-space geodetic dual-frequency measurements gathered from vessel-, LEO- and ground-based receivers

https://link.springer.com/article/10.1007/s00190-020-01397-1

Bibliography

Aa, E., Huang, W., Yu, S., Liu, S., Shi, L., Gong, J., Chen, Y., and Shen, H. (2015). A regional ionospheric tec mapping technique over china and adjacent areas on the basis of data assimilation. *Journal of Geophysical Research: Space Physics*, 120(6):5049–5061.

Afraimovich, E., Astafyeva, E., Oinats, A., Yasukevich, Y. V., and Zhivetiev, I. (2008). Global electron content: A new conception to track solar activity. In *Annales geophysicae: atmospheres, hydrospheres and space sciences*, volume 26, pages 335–344.

Afraimovich, E., Palamartchouk, K., and Perevalova, N. (1998). Gps radio interferometry of travelling ionospheric disturbances. *Journal of Atmospheric and Solar-Terrestrial Physics*, 60(12):1205–1223.

Alizadeh, M., Schuh, H., Todorova, S., and Schmidt, M. (2011). Global ionosphere maps of vtec from gnss, satellite altimetry, and formosat-3/cosmic data. *Journal of Geodesy*, 85(12):975–987.

Angrisano, A., Gaglione, S., Gioia, C., Massaro, M., and Robustelli, U. (2013). Assessment of nequick ionospheric model for galileo single-frequency users. *Acta Geophysica*, 61(6):1457–1476.

Balmforth, H., Moffett, R., and Rodger, A. (1999). Localized structure in the cusp and high-latitude ionosphere: a modelling study. In *Annales Geophysicae*, volume 17, pages 455–462. Springer.

Basu, S., Basu, S., MacKenzie, E., Coley, W., Sharber, J., and Hoegy, W. (1990). Plasma structuring by the gradient drift instability at high latitudes and comparison with velocity shear driven processes. *Journal of Geophysical Research: Space Physics*, 95(A6):7799–7818.

Basu, S., Basu, S., MacKenzie, E., and Whitney, H. (1985). Morphology of phase and intensity scintillations in the auroral oval and polar cap. *Radio Science*, 20(3):347–356.

Bilitza, D. (2001). International reference ionosphere 2000. *Radio Science*, 36(2):261–275.

Birch, M., Hargreaves, J., and Bailey, G. (2002). On the use of an effective ionospheric height in electron content measurement by gps reception. *Radio Science*, 37(1):1–19.

Buchau, J., Reinisch, B., Weber, E., and Moore, J. (1983). Structure and dynamics of the winter polar cap f region. *Radio Science*, 18(6):995–1010.

Buchau, J., Weber, E., Anderson, D., Carlson Jr, H., Moore, J., Reinisch, B., and Livingston, R. (1985). Ionospheric structures in the polar cap: Their origin and relation to 250-mhz scintillation. *Radio Science*, 20(3):325–338.

Bust, G. and Crowley, G. (2007). Tracking of polar cap ionospheric patches using data assimilation. *Journal of Geophysical Research: Space Physics*, 112(A5).

Cai, H. T., Yin, F., Ma, S. Y., and McCrea, I. W. (2011). Observations of agw/tid propagation across the polar cap: a case study. In *Annales Geophysicae*, volume 29. Springer.

Carlson, H. C. (2012). Sharpening our thinking about polar cap ionospheric patch morphology, research, and mitigation techniques. *Radio Science*, 47(04):1–16.

Chapman, S. (1931). The absorption and dissociative or ionizing effect of monochromatic radiation in an atmosphere on a rotating earth. *Proceedings of the Physical Society*, 43(1):26.

Chartier, A. T., Mitchell, C. N., and Miller, E. S. (2018). Annual occurrence rates of ionospheric polar cap patches observed using swarm. *Journal of Geophysical Research: Space Physics*, 123(3):2327–2335.

Chen, P., Yao, Y., and Yao, W. (2017). Global ionosphere maps based on gnss, satellite altimetry, radio occultation and doris. *GPS solutions*, 21(2):639–650.

Coley, W. R. and Heelis, R. A. (1995). Adaptive identification and characterization of polar ionization patches. *Journal of Geophysical Research: Space Physics*, 100(A12):23819–23827.

Coley, W. R. and Heelis, R. A. (1998). Structure and occurrence of polar ionization patches. *Journal of Geophysical Research: Space Physics*, 103(2):2201–2208.

Dandekar, B. (2002). Solar cycle dependence of polar cap patch activity. *Radio Science*, 37(1):1–13.

David, M., Sojka, J., Schunk, R., and Coster, A. (2016). Polar cap patches and the tongue of ionization: A survey of gps tec maps from 2009 to 2015. *Geophysical Research Letters*, 43(6):2422–2428.

Dettmering, D., Limberger, M., and Schmidt, M. (2014). Using doris measurements for modeling the vertical total electron content of the earth's ionosphere. *Journal of Geodesy*, 88(12):1131–1143.

Dettmering, D., Schmidt, M., Heinkelmann, R., and Seitz, M. (2011). Combination of different space-geodetic observations for regional ionosphere modeling. *Journal of Geodesy*, 85(12):989–998.

Fear, R. C., Milan, S. E., Maggiolo, R., Fazakerley, A. N., Dandouras, I., and Mende, S. B. (2014). Direct observation of closed magnetic flux trapped in the high-latitude magnetosphere. *Science*, 346(6216):1506–1510.

Feltens, J., Angling, M., Jackson-Booth, N., Jakowski, N., Hoque, M., Hernández-Pajares, M., Aragón-Àngel, A., Orús, R., and Zandbergen, R. (2011). Comparative testing of four ionospheric models driven with GPS measurements. *Radio Science*, 46(6).

Foster, J. C. (1993). Storm time plasma transport at middle and high latitudes. *Journal of Geophysical Research: Space Physics*, 98(A2):1675–1689.

Foster, J. C., Coster, A. J., Erickson, P. J., Holt, J. M., Lind, F. D., Rideout, W., ..., and Rich, F. J. (2005). Multiradar observations of the polar tongue of ionization. *Journal of Geophysical Research: Space Physics*, 110(A9).

Foster, J. C. and Doupnik, J. R. (1984). Plasma convection in the vicinity of the dayside cleft. *Journal of Geophysical Research: Space Physics*, 89(A10):9107–9113.

García-Rigo, A., Roma-Dollase, D., Hernández-Pajares, M., Lyu, H., Li, Z., Wang, N., Terkildsen, M., Olivares, G., Ghoddousi-Fard, R., Dettmering, D., Erdogan, E., Haralambous, H., Beniguel, Y., Berdermann, J., Kriegel, M., Krypiak-Gregorczyk, A., Gulyaeva, T., Fuller-Rowell, T., Altadill, D., Blanch Llosa, E., Bergeot, N., Chevalier, J., Krankowski, A., Agrotis, L., Galkin, I., Orús, R., and Prol, F. (2017). Contributions to real time and near real time ionosphere monitoring by IAG's RTIM-WG. In *Joint Scientific Assembly of the International Association of Geodesy and International Association of Seismology and Physics of the Earth's Interior*.

Gonzalez, R. C. and Woods, R. E. (2002). Digital image processing.

Gulyaeva, T. L., Arikan, F., Hernandez-Pajares, M., and Veselovsky, I. (2014). North-south components of the annual asymmetry in the ionosphere. *Radio Science*, 49(7):485–496.

Hajj, G. A. and Romans, L. J. (1998). Ionospheric electron density profiles obtained with the global positioning system: Results from the gps/met experiment. *Radio Science*, 33(1):175–190.

Hardy, D. A., Gussenhoven, M. S., Raistrick, R., and McNeil, W. J. (1987). Statistical and functional representations of the pattern of auroral energy flux, number flux, and conductivity. *Journal of Geophysical Research: Space Physics*, 92(A11):12275–12294.

Hernández-Pajares, M. (1993). Can a local bulge be differentiated? *Monthly Notices of the Royal Astronomical Society*, 264(1):1–4.

Hernandez-Pajares, M. and Floris, J. (1994). Classification of the hipparcos input catalogue using the kohonen network. *Monthly Notices of the Royal Astronomical Society*, 268(2):444–450.

Hernández-Pajares, M., Garcia-Fernàndez, M., Rius, A., Notarpietro, R., von Engeln, A., Olivares-Pulido, G., Aragón-Àngel, À., and García-Rigo, A. (2017a). Electron density extrapolation above f2 peak by the linear vary-chap model supporting new global navigation satellite systems-leo occultation missions. *Journal of Geophysical Research: Space Physics*, 122(8):9003–9014.

Hernández-Pajares, M., García-Rigo, A., Juan, J. M., Sanz, J., Monte, E., and Aragón-Àngel, A. (2012). Gnss measurement of euv photons flux rate during strong and mid solar flares. *Space Weather*, 10(12):1–16.

Hernández-Pajares, M., Juan, J., and Sanz, J. (1997). Neural network modeling of the ionospheric electron content at global scale using GPS data. *Radio Science*, 32(3):1081–1089.

Hernández-Pajares, M., Juan, J., and Sanz, J. (1999). New approaches in global ionospheric determination using ground gps data. *Journal of Atmospheric and Solar-Terrestrial Physics*, 61(16):1237–1247.

Hernández-Pajares, M., Juan, J., and Sanz, J. (2000a). Improving the Abel inversion by adding ground GPS data to LEO radio occultations in ionospheric sounding. *Geophysical Research Letters*, 27(16):2473–2476.

Hernández-Pajares, M., Juan, J., Sanz, J., and Colombo, O. (2002). Improving the real-time ionospheric determination from gps sites at very long distances over the equator. *Journal of Geophysical Research: Space Physics*, 107(A10):SIA–10.

Hernández-Pajares, M., Juan, J., Sanz, J., and Colombo, O. L. (2000b). Application of ionospheric tomography to real-time gps carrier-phase ambiguities resolution, at scales of 400–1000 km and with high geomagnetic activity. *Geophysical Research Letters*, 27(13):2009–2012.

Hernández-Pajares, M., Juan, J., Sanz, J., Orus, R., Garcia-Rigo, A., Feltens, J., Komjathy, A., Schaer, S., and Krankowski, A. (2009). The igs vtec maps: a reliable source of ionospheric information since 1998. *Journal of Geodesy*, 83(3-4):263–275.

Hernández-Pajares, M., Juan, J., Sanz, J., and Sole, J. (1998). Global observation of the ionospheric electronic response to solar events using ground and LEO GPS data. *Journal of Geophysical Research: Space Physics*, 103(A9):20789–20796.

Hernández-Pajares, M., Juan, J. M., Sanz, J., Aragón-Àngel, À., García-Rigo, A., Salazar, D., and Escudero, M. (2011). The ionosphere: effects, gps modeling and the benefits for space geodetic techniques. *Journal of Geodesy*, 85(12):887–907.

Hernández-Pajares, M., Lyu, H., An, J., Jiang, H., and Aragón-Àngel, A. (2018a). Time evolution of vertical electron content distribution in polar ionosphere from UPC-GIM TOMION runs. In *International GNSS Service Workshop*, pages 1–1, Wuhan.

Hernández-Pajares, M., Lyu, H., Aragón-Àngel, A., Monte Moreno, E., Liu, J., An, J., and Jiang, H. (2019a). The Polar Ionosphere seen through Global Ionospheric Maps. In *The 20th International Beacon Satellite Symposium*, pages 1–20, Olsztyn.

Hernández-Pajares, M., Lyu, H., Aragón-Àngel, À., Monte-Moreno, E., Liu, J., An, J., and Jiang, H. (2020a). Polar electron content from gps data-based global ionospheric maps: Assessment, case studies, and climatology. *Journal of Geophysical Research: Space Physics*, 125(6):e2019JA027677.

Hernández-Pajares, M., Lyu, H., Garcia-Fernandez, M., and Orus-Perez, R. (2020b). A new way of improving global ionospheric maps by ionospheric tomography: consistent combination of multi-gnss and multi-space geodetic dual-frequency measurements gathered from vessel-, leo- and ground-based receivers. *Journal of Geodesy*, 94(8):1–16.

Hernández-Pajares, M., Lyu, H., Monte Moreno, E., Yang, H., dos Santos Prol, F., Roma Dollase, D., and García-Rigo, A. (2018b). Recent results on ionospheric modeling with UPC-IonSAT contributions. In *Specialized Summit on Space Geodesy and Ionosphere Research*, pages 1–33, Berlin.

Hernández-Pajares, M., Lyu, H., Nohutcu, M., Garcia-Rigo, A., Zhang, H., and Liu, J. (2017b). New ionospheric mapping function (BIM) and other recent contributions to GNSS ionospheric sounding involving UPC-IonSAT. In *Specialized Summit on Space Geodesy and Ionosphere Research*, pages 1–28, Berlin.

Hernández-Pajares, M., Lyu, H., Yang, H., Monte Moreno, E., Aragón-Àngel, A., and Cardellach, E. (2019b). Recent contributions to GNSS Ionospheric modelling: Truncated Radio-Occultations, multi-TID tsunami signatures and GIMs information on Polar Ionosphere. In *Specialized Summit on Space Geodesy and Ionosphere Research*, pages 1–58, Berlin.

Hernández-Pajares, M. and Moreno-Borràs, D. (2020). Real-time detection, location and measurement of geoeffective stellar flares from global navigation satellite system data: new technique and case studies. *Space Weather*, 18(https://doi.org/10.1029/2020SW002441):1–10.

Hernández-Pajares, M., Olivares-Pulido, G., Aragón-Àngel, A., dos Santos Prol, F., Lyu, H., Monte Moreno, E., E., C., Garcia-Fernàndez, M., A., R., R., N., von Engelni, A., R. Themens, D., García-Rigo, A., de Oliveira Camargoi, P., and Tadeu de Assis Honorato Muella, M. (2019c). Recent progress in Linear Vary-Chapman (LVC) modelling of the electron density. In *The International Workshop on GNSS Ionosphere*, pages 1–37, Neustrelitz.

Hernández-Pajares, M., Roma-Dollase, D., García-Rigo, A., Monte-Moreno, E., Yang, H., Lyu, H., dos Santos Prol, F., Themens, D., Garcia-Fernandez, M., Orus-Perez, R., Li, Z., Wang, N., Yuan, Y., Laurichesse, D., and Blot, A. (2019d). Recent UPC-IonSAT results on global RT and other ionospheric modelling problems. In *The 10th China Satellite Navigation Conference (CSNC 2019)*, pages 1–29, Beijing.

Hernández-Pajares, M., Roma-Dollase, D., Krankowski, A., García-Rigo, A., and Orús-Pérez, R. (2017c). Methodology and consistency of slant and vertical assessments for ionospheric electron content models. *Journal of Geodesy*, 91(12):1405–1414.

Hernández-Pajares, M., Zornoza, J. M. J., Subirana, J. S., Farnworth, R., and Soley, S. (2005). Egnos test bed ionospheric corrections under the october and november 2003 storms. *IEEE transactions on Geoscience and Remote Sensing*, 43(10):2283–2293.

Hoque, M. M. and Jakowski, N. (2013). Mitigation of ionospheric mapping function error.

Hunsucker, R. D. and Hargreaves, J. K. (2007). *The high-latitude ionosphere and its effects on radio propagation*. Cambridge University Press.

Jakowski, N., Heise, S., Wehrenpfennig, A., Schlüter, S., and Reimer, R. (2002). Gps/glonass-based tec measurements as a contributor for space weather forecast. *Journal of Atmospheric and Solar-Terrestrial Physics*, 64(5-6):729–735.

Jakowski, N., Hoque, M., and Mayer, C. (2011). A new global tec model for estimating transionospheric radio wave propagation errors. *Journal of Geodesy*, 85(12):965–974.

Jin, S., Occhipinti, G., and Jin, R. (2015). Gnss ionospheric seismology: Recent observation evidences and characteristics. *Earth-Science Reviews*, 147:54–64.

Juan, J. M., Rius, A., Hernández-Pajares, M., and Sanz, J. (1997). A two-layer model of the ionosphere using global positioning system data. *Geophysical Research Letters*, 24(4):393–396.

Kelley, M. C., Vickrey, J. F., Carlson, C., and Torbert, R. (1982). On the origin and spatial extent of high-latitude f region irregularities. *Journal of Geophysical Research: Space Physics*, 87(A6):4469–4475.

Kelly, J. D. and Vickrey, J. F. (1984). F-region ionospheric structure associated with antisunward flow near the dayside polar cusp. *Geophysical research letters*, 11(9):907–910.

Klobuchar, J. A. (1987). Ionospheric time-delay algorithm for single-frequency gps users. *IEEE Transactions on aerospace and electronic systems*, (3):325–331.

Kohonen, T. (1990). The self-organizing map. *Proceedings of the IEEE*, 78(9):1464–1480.

Kohonen, T. (2012). *Self-organization and associative memory*, volume 8. Springer Science & Business Media.

Komjathy, A. and Langley, R. (1996). The effect of shell height on high precision ionospheric modelling using gps. In *Proceedings of the 1996 IGS workshop international GPS service for geodynamics (IGS)*, volume 203.

Laundal, K. M., Cnossen, I., Milan, S. E., Haaland, S., Coxon, J., Pedatella, N., Förster, M., and Reistad, J. P. (2017). North–south asymmetries in earth's magnetic field. *Space Science Reviews*, 206(1-4):225–257.

Leitinger, R., Ladreiter, H.-P., and Kirchengast, G. (1997). Ionosphere tomography with data from satellite reception of global navigation satellite system signals and ground reception of navy navigation satellite system signals. *Radio Science*, 32(4):1657–1669.

Linde, Y., Buzo, A., and Gray, R. (1980). An algorithm for vector quantizer design. *IEEE Transactions on communications*, 28(1):84–95.

Liu, J., Chen, R., Wang, Z., and Zhang, H. (2011). Spherical cap harmonic model for mapping and predicting regional tec. *GPS solutions*, 15(2):109–119.

Liu, J., Wang, W., Burns, A., Liu, L., and McInerney, J. (2017). A tiegcm numerical study of the source and evolution of ionospheric f-region tongues of ionization: Universal time and interplanetary magnetic field dependence. *Journal of Atmospheric and Solar-Terrestrial Physics*, 156:87–96.

Lockwood, M. and Carlson Jr, H. (1992). Production of polar cap electron density patches by transient magnetopause reconnection. *Geophysical research letters*, 19(17):1731–1734.

Luenberger, D. G., Ye, Y., et al. (1984). *Linear and nonlinear programming*, volume 2. Springer.

Lyu, H., Hernández-Pajares, M., Aragón-Àngel, A., Monte Moreno, E., Liu, J., An, J., and Jiang, H. (2020). Polar electron content features shown in UQRG GIMs and climatology study by Learning Vector Quantization. In *GNSS Research and Application for Polar Environment (GRAPE)/RESOURCE Online Workshop*, pages 1–23, Online.

Lyu, H., Hernández-Pajares, M., and Monte-Moreno, E. (2017a). Derivation and applicability of 3D electron content and decorrelation lengths obtained from ground- and LEO-based GNSS models. In *URSI General Assembly and Scientific Symposium*, pages 1–46, Montreal.

Lyu, H., Hernández-Pajares, M., Monte-Moreno, E., B., N., and Cardellach, E. (2018a). A hybrid of Abel inversion and Vary-Chap model to reconstruct RO electron density profile. In *International GNSS Service Workshop*, pages 1–1, Wuhan.

Lyu, H., Hernández-Pajares, M., Monte-Moreno, E., and Cardellach, E. (2019a). Electron density retrieval from truncated radio occultation gnss data. *Journal of Geophysical Research: Space Physics*, 124(6):4842–4851.

Lyu, H., Hernández-Pajares, M., Monte-Moreno, E., and Cardellach, E. (2019b). Two methods of electron density retrieval from truncated ionospheric radio occultation data. In *EUMETSAT ROM SAF - IROWG2019*, pages 1–45, Copenhagen.

Lyu, H., Hernández-Pajares, M., Nohutcu, M., and Garcia-Rigo, A. (2017b). The new Barcelona Ionospheric Mapping Function (BIMF). In *International Colloquium on Scientific and Fundamental Aspects of GNSS / Galileo*, pages 1–26, Valencia.

Lyu, H., Hernández-Pajares, M., Nohutcu, M., and Garcia-Rigo, A. (2017c). The New Barcelona Ionospheric Mapping Function for North Mid Latitude GNSS applications. In *International GNSS Service Workshop*, pages 1–1, Paris.

Lyu, H., Hernández-Pajares, M., Nohutcu, M., García-Rigo, A., Zhang, H., and Liu, J. (2018b). The barcelona ionospheric mapping function (bimf) and its application to northern mid-latitudes. *GPS solutions*, 22(3):67.

Mandea, M. and Purucker, M. (2018). The varying core magnetic field from a space weather perspective. *Space Science Reviews*, 214(1):11.

Murtagh, F. and Hernández-Pajares, M. (1995). The kohonen self-organizing map method: an assessment. *Journal of Classification*, 12(2):165–190.

Nava, B., Coisson, P., and Radicella, S. (2008). A new version of the nequick ionosphere electron density model. *Journal of Atmospheric and Solar-Terrestrial Physics*, 70(15):1856–1862.

Niranjan, K., Srivani, B., Gopikrishna, S., and Rama Rao, P. (2007). Spatial distribution of ionization in the equatorial and low-latitude ionosphere of the indian sector and its effect on the pierce point altitude for gps applications during low solar activity periods. *Journal of Geophysical Research: Space Physics*, 112(A5).

Noja, M., Stolle, C., Park, J., and Lühr, H. (2013). Long-term analysis of ionospheric polar patches based on champ tec data. *Radio Science*, 48(3):289–301.

Olivares-Pulido, G., Hernández-Pajares, M., Aragón-Àngel, A., and Garcia-Rigo, A. (2016). A linear scale height chapman model supported by gnss occultation measurements. *Journal of Geophysical Research: Space Physics*, 121(8):7932–7940.

Orús, R., Hernández-Pajares, M., Juan, J., and Sanz, J. (2005). Improvement of global ionospheric VTEC maps by using kriging interpolation technique. *Journal of Atmospheric and Solar-Terrestrial Physics*, 67(16):1598–1609.

Powell, M. J. (1964). An efficient method for finding the minimum of a function of several variables without calculating derivatives. *The computer journal*, 7(2):155–162.

Press, W. H., Flannery, B. P., Teukolsky, S. A., Vetterling, W. T., et al. (1989). Numerical recipes.

Raghunath, S. and Ratnam, D. V. (2015). Detection of low-latitude ionospheric irregularities from gnss observations. *IEEE Journal of Selected Topics in Applied Earth Observations and Remote Sensing*, 8(11):5171–5176.

Reinisch, B., Nsumei, P., Huang, X., and Bilitza, D. (2007). Modeling the f2 topside and plasmasphere for iri using image/rpi and isis data. *Advances in Space Research*, 39(5):731–738.

Rishbeth, H. and Garriott, O. K. (1969). *Introduction to ionospheric physics*, volume 14. Academic Press New York.

Robbins, H. and Monro, S. (1951). A stochastic approximation method. *The annals of mathematical statistics*, pages 400–407.

Rodger, A., Pinnock, M., Dudeney, J., Baker, K., and Greenwald, R. (1994). A new mechanism for polar patch formation. *Journal of Geophysical Research: Space Physics*, 99(A4):6425–6436.

Roma-Dollase, D., Hernández-Pajares, M., Krankowski, A., Kotulak, K., Ghoddousi-Fard, R., Yuan, Y., Li, Z., Zhang, H., Shi, C., Wang, C., et al. (2018). Consistency of seven different gnss global ionospheric mapping techniques during one solar cycle. *Journal of Geodesy*, 92(6):691–706.

Sakai, T., Yoshihara, T., Saito, S., Matsunaga, K., Hoshinoo, K., and Walter, T. (2001). Modeling vertical structure of ionosphere for sbas. In *Proceedings of the 22nd International Technical Meeting of The Satellite Division of the Institute of Navigation (ION GNSS 2009)*, pages 1257–1267.

Sojka, J. J., Bowline, M., and Schunk, R. W. (1994). Patches in the polar ionosphere: Ut and seasonal dependence. *Journal of Geophysical Research: Space Physics*, 99(A8):14959–14970.

Sojka, J. J., Bowline, M. D., Schunk, R. W., Decker, D. T., Valladares, C. E., Sheehan, R., ..., and Heelis, R. A. (1993). Modeling polar cap f-region patches using time varying convection. *Geophysical Research Letters*, 20(17):1783–1786.

Spicher, A., Clausen, L. B. N., Miloch, W. J., Lofstad, V., Jin, Y., and Moen, J. I. (2017). Interhemispheric study of polar cap patch occurrence based on swarm in situ data. *Journal of Geophysical Research: Space Physics*, 122(3):3837–3851.

Todorova, S., Hobiger, T., and Schuh, H. (2008). Using the global navigation satellite system and satellite altimetry for combined global ionosphere maps. *Advances in Space Research*, 42(4):727–736.

Weber, E., Buchau, J., Moore, J., Sharber, J., Livingston, R., Winningham, J. D., and Reinisch, B. (1984). F layer ionization patches in the polar cap. *Journal of Geophysical Research: Space Physics*, 89(A3):1683–1694.

Weber, E., Klobuchar, J., Buchau, J., Carlson Jr, H., Livingston, R., de La Beaujardiere, O., McCready, M., Moore, J., and Bishop, G. (1986). Polar cap f layer patches: Structure and dynamics. *Journal of Geophysical Research: Space Physics*, 91(A11):12121–12129.

Wild, J. A., Cowley, S. W. H., Davies, J. A., Khan, H., Lester, M., Milan, S. E., Provan, G., Yeoman, T. K., Balogh, A., Dunlop, M. W., Fornacon, K. H., and Georgescu, E. (2001). First simultaneous observations of flux transfer events at the high-latitude magnetopause by the cluster spacecraft and pulsed radar signatures in the conjugate ionosphere by the cutlass and eiscat radars. In *Annales Geophysicae*, volume 19, pages 1491–1508. Springer.

Wild, J. A., Milan, S. E., Cowley, S. W. H., Dunlop, M. W., Owen, C. J., Bosqued, J. M., . . . , and Yukimatu, A. S. (2003). Coordinated interhemispheric superdarn radar observations of the ionospheric response to flux transfer events observed by the cluster spacecraft at the high-latitude magnetopause. In *Annales Geophysicae*, volume 21, pages 1807–1826. Springer.

Witze, A. (2019). Earth's magnetic field is acting up and geologists don't know why. *Nature*, 565(7738):143–145.

Yao, Y., Liu, L., Kong, J., and Zhai, C. (2018). Global ionospheric modeling based on multi-gnss, satellite altimetry, and formosat-3/cosmic data. *GPS Solutions*, 22(4):104.

Zhang, Q.-H., Lockwood, M., Foster, J., Zhang, S.-R., Zhang, B.-C., McCrea, I., Moen, J., Lester, M., and Ruohoniemi, J. M. (2015). Direct observations of the full dungey convection cycle in the polar ionosphere for southward interplanetary magnetic field conditions. *Journal of Geophysical Research: Space Physics*, 120(6):4519–4530.

Zhang, Q.-H., Zhang, B.-C., Moen, J., Lockwood, M., McCrea, I., Yang, H.-G., Hu, H.-Q., Liu, R.-Y., Zhang, S.-R., and Lester, M. (2013). Polar cap patch segmentation of the tongue of ionization in the morning convection cell. *Geophysical Research Letters*, 40(12):2918–2922.

Zus, F., Deng, Z., Heise, S., and Wickert, J. (2017). Ionospheric mapping functions based on electron density fields. *GPS Solutions*, 21(3):873–885.